A STUDY OF THE VANADIUM OXIDE BRONZE θ-VOB, AND VANADIUM OXIDES V_2O_5 AND VO_2, USING HYPERFINE INTERACTION TECHNIQUES

by Vishnu Visvanathan Naicker

Submitted in part fulfilment of the requirements for the degree of Doctor of Philosophy in the Department of Physics, Faculty of Science, at the University of Durban-Westville.

Promoter: Prof. K. Bharuth-Ram

Joint Promoter: Prof. K. P. Lieb

Date submitted: January 1999

DECLARATION

I, the undersigned, VISHNU VISVANATHAN NAICKER, declare that these studies represent original work by me and have not been submitted in any form to another university. Where use was made of the work of others, it has been duly acknowledged in the text.

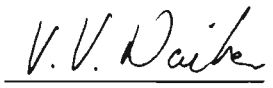

V.V.Naicker

January 1999

ABSTRACT

One of the main interests in the vanadium oxides V_2O_5 and VO_2 is that, when doped with a metal such as Fe, these oxides display semiconductor-to-metal transitions at certain critical temperatures. These transitions are also accompanied with changes in the crystallographic phases of the oxides. This thesis describes the use of hyperfine interactions at dopant sites in the vanadium oxides V_2O_5 and VO_2 to infer information on the phase transitions that take place in these oxides.

The hyperfine interaction techniques of Mössbauer Spectroscopy and Time Differential Perturbed Angular Correlation (TDPAC) are used to study the hyperfine parameters in the Fe - V_2O_5 system and Cd - V_2O_5 system, respectively. X-ray powder diffraction spectroscopy were also conducted on the samples to establish the phases created.

A large part of this project was spent in the design of apparatus. The apparatus constructed were (i) a furnace to perform a solid state reaction in order to introduce Fe into V_2O_5, the maximum operating temperature of the furnace being 1473 K, (ii) a Mössbauer sample chamber and sample holder which enabled the sample to be heated up to a temperature of 873 K, and (iii) a device constructed to determine the electrical conductivities of powder samples at temperatures ranging from 773 K to room temperature.

For the Mössbauer studies, the Fe-V_2O_5 system was studied as a function of the Fe concentration. Six symmetric doublets, with intensities changing as the Fe concentration changed, were observed. Correlating the Mössbauer components of the individual spectra

with the phases identified using powder x-ray diffraction patterns in terms of the reflection intensities, allowed two of the doublets to be assigned to lattice sites in the vanadium oxide bronze system, θ-VOB, a further two doublets to substitutional and interstitial sites in the Fe doped V_2O_5 system, respectively, and the fifth doublet to the super-paramagnetic Fe_2O_3 phase. The sixth doublet observed was attributed to an unresolved crystallographic phase observed in the x-ray diffraction spectra at large Fe concentrations.

The magnitude of the quadrupole splittings of the doublets assigned to the vanadium oxide bronze and the Fe-V_2O_5 systems indicate that the electronic environment of the Fe atoms in the bronze phase displays a greater symmetry than those in the V_2O_5 phase.

In order to gain insight on the semiconducting nature of the Fe doped V_2O_5 and the θ-VOB phases, temperature dependent Mössbauer measurements ranging from 300 K to 573 K, together with electrical conductivity measurements, were performed on a few samples. The temperature dependent Mössbauer spectra displayed the usual second order Doppler shift of the isomer shifts for the various components as a function of temperature, but no significant change in the magnitude of the quadrupole splittings. From this result, on the basis of the Duncan-Golding correlation diagram, the valence state of the Fe ions was inferred to be 3+. No components were observed (with increasing temperature) that could be correlated with the population of Fe^{2+} states. This therefore suggests that the semiconducting properties of the Fe doped V_2O_5 phase and the θ-VOB phase are associated with electron hopping between V^{4+} - V^{5+} valence sites rather than Fe^{3+} - Fe^{2+} valence sites.

^{111}In-TDPAC measurements were made on V_2O_5 and VO_2. For V_2O_5, the measurements yielded one distinct substitutional cation site for the ^{111}Cd ions, with quadrupole coupling constant ν_Q = 88,1(3) MHz, and asymmetry η = 0,619(3)

In VO_2, temperature dependent TDPAC measurements yielded two well defined quadrupole coupling frequencies for the ^{111}Cd probe nuclei, the first , ν_Q = 43,0(7) MHz, observed at room temperature, corresponding to a monoclinic or triclinic phase of VO_2, and the second, ν_Q = 89,1(1) MHz, observed at 423 K and above, corresponding to the rutile phase of VO_2.

I dedicate this thesis to my wife Desnie and daughter Mekara,
who showed me the true meaning of happiness
which cannot be obtained in any Physics laboratory.

ACKNOWLEDGEMENTS

I would like to acknowledge the following people for their guidance, advice and support, without which this thesis would not have been possible

My promoters, Prof. K. Bharuth-Ram (University of Durban-Westville) and Prof. K. P. Lieb (Universität Göttingen, Germany), for their extremely high standard of supervision. Their keen interest, encouragement and guidance were invaluable.

Prof. J. Dunlevy (Department of Geology, University of Durban-Westville) for his invaluable assistance with the acquisition of the X-ray scans.

Mr V. Lester, Mr S. Pillay, Mr I. Ramlakhan, Mr S. Reddy and Mr J. Pillay (Academic Instrument Unit, University of Durban-Westville) for their willing and expert technical support.

My fellow students at the University of Durban-Westville, who all provided support in one way or another, especially Mr D. Naidoo and Mr. D. Gxawu.

The students who were at the Zweites Physikalishes Institüt, Universität Göttingen, especially Dr A. Bartos, Dr T. Wenzel and Dr D. Wiarda, for their invaluable assistance and advice.

All my colleagues in the Department of Physics, University of Durban-Westville, for their assistance and concern.

My family and friends, especially my parents Krish and Grace, my wife's parents Rajen and Salome, and my daughter Mekara, for their unfailing support and encouragement.

Lastly, and not least, my wife Desnie, whose constant support and understanding, enabled me to accomplish this thesis.

CONTENTS

I. INTRODUCTION

The vanadium-oxide system ranges from the element vanadium to V_2O_5. In this system, the well known stable oxides are V_2O_5, VO_2, V_2O_3 and VO. The production of the lower oxides (e.g. V_2O_3, V_6O_{13} and VO_2) can be obtained from V_2O_5 using suitable reduction procedures [BOS84]. Intermediate non-stoichiometric oxides also exist as stable oxides, of which the Magneli phases V_nO_{2n-1}, which exists between V_2O_3 and VO_2, is one such example. Table 1.1 summarises the physical properties of some of these oxides.

Interest in the vanadium oxides stems from several considerations, both practical and theoretical. Of particular interest are the electrical properties of the vanadium oxides. At some critical temperature, the oxide changes from non-metallic to metallic or semiconductor to metallic [MOR59, MOO70, JON65, FEI67, OKI69 and OKI70]. In most cases, crystallographic phase changes also accompany these transitions [ADL67, FEI67, WAR60, KOS67, PEB83 and WIE78]. Further, some of these oxides also display changes in their magnetic properties at the transition temperatures [MOO70, JON65, FAB90, UME65, RUD58, KAW64, KOS67 and KKO67]. The transition temperatures of a few oxides, together with the crystallographic phases and magnetic properties before, and after, the transition (i.e. in the low temperature phase and the high temperature phase) are included in Table 1.1.

V_2O_5 in its pure form has not been reported to display any insulator/semiconductor to metal transition, but when doped with small amounts of foreign metals, this transition also manifests itself, [KHA90, PEK80, BAN87, BAR85].

Another important practical application is the suitability of vanadium and its alloys for industrial use [MOO91]. For example, the vanadium steels are used for general engineering purposes. Steels doped with small concentrations of vanadium, 0.1 - 0.25% V, have excellent welding characteristics. Steels doped with chromium and tungsten and vanadium concentrations of 1- 5% are used for the manufacture of high speed tools which are noted for hardness retention over a moderate temperature range [MOO91]. Vanadium steels are also used in high pressure boilers, locomotive parts, gears and turbines [MOO91].

Vanadium metal, with body centred cubic structure, has potential applications as a high temperature material, for example, in advanced nuclear reactors and power plants, and in applications in superconducting devices [JAN82].

Although in the applications, the vanadium doped materials are not fabricated with the intent of having oxides present in their composition, traces of these oxides are always present arising from the normal production processes used for these materials and from the applications of the materials, i.e. oxidation of the material due to heating over time. Thus, a careful study of the solubility of oxygen in the vanadium alloy/steel systems is essential to the understanding of its effect on the desired properties of these materials.

In the vanadium oxides, interest also stems from their chemical applications. The highest oxide of the vanadium oxide system, V_2O_5, is widely used as catalysts, for example, in the oxidation of sulphur dioxide, carbon monoxide, and hydrocarbons [ROO80, MOR87 and CAV88]. V_2O_5 is also used as a functional inorganic material, having wide applications for such functions as gas sensors, catalysts, and secondary battery electrodes [SHI90].

^{57}Fe and ^{111}Cd were chosen as probe atoms, and hence the investigations were mainly conducted using the hyperfine interaction techniques of Mössbauer Spectroscopy and Time Differential Perturbed Angular Correlations. Complimentary x-ray diffraction studies and electrical conductivity measurements were also made on some samples.

In both these hyperfine interaction methods, probes are introduced into the host lattices and information concerning the immediate environment of these probes are obtained from the interaction between the nuclear moments (magnetic and/or electrical quadrupole) of the probe nuclei and the charge distribution and electric field gradient at the probe site.

By controlling the concentration of the probes, information about the parent material can be inferred, i.e. these probes are introduced into the oxides in small amounts so that the oxides remain virtually unchanged in terms of their crystallographic structure. The hyperfine interaction then yields insight on the bonding of the probes in these oxide environments and on the symmetry of the environment of the probes.

In the studies presented in this thesis, ^{57}Fe and ^{111}Cd are used for the Mössbauer effect and TDPAC studies, respectively. Exact correlations between the two sets of hyperfine interaction measurements are therefore not possible due to the difference in the electronic structure of vanadium with Fe and Cd, respectively.

As stated above, V_2O_5 when doped with small amounts of foreign metals display semiconducting behaviour. This has prompted several studies on the Fe-V_2O_5 system, in particular, using Mössbauer Spectroscopy, to investigate the configurations of the dopant atoms. Several ^{57}Fe Mössbauer Spectroscopy studies have been reported [ABD69, BUR76 and BUR78]. In these studies, Fe was introduced into the V_2O_5 lattice using a solid state reaction in which Fe_2O_3 powder and V_2O_5 powder were mechanically mixed according to required molar ratios and then melted for some pre-set time at a temperature greater than the melting point of V_2O_5. Two components in the Mössbauer spectra were identified as Fe sites in the V_2O_5 lattice and a third component was attributed to the superparamagetic phase of α-Fe_2O_3.

Closely related to these studies on Fe doped V_2O_5, are the Mössbauer studies on the oxides referred to as the vanadium oxide bronzes (θ-VOB) [BAR74, PEK80, BAR85 and KOR82]. Here, Fe is present in the V_2O_5 lattice according to the formula $Fe_xV_2O_5$, where x ranges between 0.33 and 0.38. The θ-VOB phase has a different crystallographic structure (monoclinic) to that of the pure V_2O_5 phase (orthorhombic). In these studies, the samples

were also produced using a solid state reaction as in the case of Fe doped V_2O_5, with the difference that Fe powder instead of Fe_2O_3 powder was used as the second reactant.

The results obtained from each of these investigations differ from each other. Pekala et al. [PEK80] observed a single paramagnetic line above 17 K. Baran et al. [BAR74] observed a strong quadrupole doublet and two additional weak doublets. They attributed the strong doublet to a site in the vanadium oxide bronze, and followed Abdullaev et al. [ABD69] in attributing the weak doublets to sites in Fe doped V_2O_5. Korecki et al. [KOR82] observed two quadrupole doublets. Bara et al. [BAR85] observed two broad lines in the Mössbauer spectra, to which they could fit four quadrupole doublets. They were, however, unable to assign these observed doublets to four non-equivalent types of surrounding in the vanadium oxide bronze.

The vanadium oxide bronze is of considerable interest since it displays a semiconducting nature. An "electron hopping" mechanism [KRU76] has been suggested to explain this semiconducting property. It is proposed that the solution of Fe in the V_2O_5 lattice provides a trap for the electrons. The Fe is most likely to exist in the 3+ oxidation state, with the 2+ oxidation state also a possibility. Therefore, since electrical neutrality must be maintained, this leads to the creation of V^{4+} and V^{5+} centres, which then provide electron hopping sites.

This mechanism could also be extended to explain the semiconducting behaviour [KHA90, JAN73] in the case of Fe doped V_2O_5, where the foreign atoms have a concentration x smaller than 0.33.

Lass et al. [LAS86] have extended the Mössbauer study of the θ-VOB system to temperatures below 300 K and have shown that magnetic order sets in below 18 K.

The present study can be divided into three parts. The first part involved the design and construction of some of the apparatus used for the Mössbauer studies. These were the furnace used for producing the Fe doped samples, the sample holders and sample chamber, and the apparatus used to measure the electrical conductivity of the powders.

The second part involved the Mössbauer effect and related measurements. This encompassed the physical preparation of the Fe doped Mössbauer samples and the subsequent Mössbauer measurements, the x-ray powder diffraction measurements, and the electrical conductivity measurements.

In preparing the Mössbauer samples, natural Fe powder rather than Fe_2O_3 powder was used in the solid state reaction. The molar concentration of the Fe powder with respect to that of the V_2O_5 powder in the melt ranged from 5% to 80%. This concentration range encompassed the Fe doped V_2O_5 phase (which was the phase with the Fe concentration small) and the vanadium oxide bronze phase, θ-VOB. The determination of the hyperfine parameters for the entire concentration range was therefore carried out.

With the aim of obtaining information on the mechanism responsible for the observed semiconducting behaviour of V_2O_5, temperature dependent Mössbauer measurements on a

selection of the samples were also performed. These measurements were complimented with electrical conductivity measurements.

The third part of this study involved the time differential perturbed angular correlation (TDPAC) measurements on V_2O_5 and VO_2. ^{111}Cd was used as the probe in the V_2O_5 lattice and it was introduced into the material by ion implantation of radioactive ^{111}In, which decays by electron capture to ^{111}Cd. In these cases the concentration of the probe was very small. This meant that the material under study was that of a doped V_2O_5 specimen rather than a mixture of the doped V_2O_5 and an equivalent cadmium-vanadium oxide phase corresponding to the θ-VOB. The results therefore reflected the hyperfine interaction of ^{111}Cd doped V_2O_5.

Mössbauer studies as a function of temperature were previously conducted on the VO_2 lattice doped with ^{57}Fe [KOS67]. In these studies, the phase change from the semi-conductor to the metal was observed. In the present study, TDPAC studies of VO_2 as a function of the annealing temperature and the sample temperature were performed. These results are correlated with that of the Mössbauer results of Kosuge et al. [KOS67] in terms of the semiconductor-to-metal transition.

The first two parts of this research was conducted in the Physics Department, at the University of Durban-Westville, South Africa, and the third part was conducted at the Zweites Physikalishes Institüt, Universität Göttingen, Germany.

Table 1.1. Summary of the physical, electrical, magnetic and crystallographic properties of some vanadium oxides

oxide	Physical Appearance	Melting Point (K)	Transitn. Temp. T_c	Electrical Properties		Magnetic Properties		Crystallographic Phases	
				Below T_c	Above T_c	Below T_c	Above T_c	Below T_c	Above T_c
VO	black powder PRA67	2350 CRC72	126 K ADL67	semiconductor MOR59	metallic MOR59			orthorhombic ADL67	rock salt ADL67
V_2O_3	black crystals PRA67	2240 CRC72	150 K FEI67,DER70, ADL67	insulator MOO70, JON65 semiconductor FEI67	metallic FEI67	anti-ferromagnetic MOO70, JON65 FAB90	paramagnetic FAB90	monoclinic FEI67, WAR60,	corundum - rhombohedral FEI67,ADL67
VO_2	deep blue crystals PRA67	1818 CRC72	340 K ADL67	semiconductor MOR59	metallic MOR59	paramagnetic UME65, RUD58, KAW64, KOS67	paramagnetic KOS67	2 monoclinic & 1 triclinic KOS67,PEB83, WIE78 & ADL67	rutile tetragonal ADL67, KOS67
V_2O_5	orange red powder PRA67	943 CRC72							
V_3O_5		2100 CRC72	133 K KKO67, GRO60, OKI72						
V_4O_7			250 K KKO67, GRO60,	semiconductor OKI69, OKI70	metallic OKI69, OKI70	paramagnetic KKO67	paramagnetic KKO67		
V_5O_9			135 K KKO67, GRO60,	semiconductor OKI69, OKI70	metallic OKI69, OKI70	paramagnetic KKO67	paramagnetic KKO67		
V_6O_{11}			170 K KKO67, GRO60,	semiconductor OKI69, OKI70	metallic OKI69, OKI70				
V_8O_{15}			70 K KKO67, GRO60,	semiconductor OKI69, OKI70	metallic OKI69, OKI70				

II : THEORY

2.1 HYPERFINE INTERACTIONS

The study of the interaction of the electrical quadrupole moment or magnetic dipole moment of an atomic nucleus with its surrounding electric field gradient or magnetic field, respectively, often leads to insight on the nature of these fields surrounding the nucleus. A brief overview of both these interactions is presented below. More detailed discussion on the theory can be obtained in Frauenfelder and Steffen [FRA65] and Schatz and Weidinger [SCH96].

2.1.1 The Electric Hyperfine Interaction

Consider an atomic nucleus in an electric potential Φ. The electric potential can arise from the asymmetry of the electronic orbitals, or the asymmetry of the host lattice. The energy, E_{elec}, of the interaction can be written as the sum of three terms

$$E_{elec} = E^{(0)} + E^{(1)} + E^{(2)} \qquad 2.1$$

where higher order terms which vanish or are negligibly small are neglected, and where

$$E^{(0)} = \Phi_0 \int \rho(\vec{r}) \partial^3 r \qquad 2.1a$$

$$E^{(1)} = \sum \left(\frac{\partial \Phi}{\partial x_\alpha} \right)\Bigg|_0 \int \rho(\vec{r}) x_\alpha \partial^3 r \qquad 2.1b$$

$$E^{(2)} = \tfrac{1}{2} \sum \left(\frac{\partial^2 \Phi}{\partial x_\beta \partial x_\beta} \right)\Bigg|_0 \int \rho(\vec{r}) x_\alpha x_\beta \partial^3 r \,. \qquad 2.1c$$

In these equations, $\rho(\vec{r})$ is the nuclear charge density, with the integration performed over the finite nuclear volume.

The first term $E^{(o)}$ represents the Coulomb energy for a point charge of atomic number Z and electric charge e in a potential Φ_o. For the hyperfine methods employed in the present work, namely, the Mössbauer Effect (ME) and the time differential perturbed angular correlation (TDPAC), the interacting probe nuclei for each method are the isotopes ^{57}Fe and ^{111}In, respectively. Since the value of Z remains constant in each method, this first term can be ignored since its effect cancels when comparing the excited state with the ground state of the nuclei.

The second term $E^{(1)}$ is the interaction at the origin between the electric dipole moment of the nucleus and the electric field. Due to the definite parity of the nuclear states, the expectation value of the electric dipole moment is zero. Therefore, this second term $E^{(1)}$ in the energy of the interaction disappears.

All that remains is the third term $E^{(2)}$ which can be written in terms of two components in the following way:

$$E^{(2)} = E_C + E_Q \qquad 2.2$$

where

$$E_C = \frac{Ze^2}{6\varepsilon_0}\left|\Psi(0)\right|^2\left\langle r^2\right\rangle \qquad 2.2a$$

and

$$E_Q = \frac{e}{c}\sum V_{\alpha\alpha}Q_{\alpha\alpha}\,. \qquad 2.2b$$

In Eqn. (2.2(a)), $|\Psi(0)|^2$ is the probability of finding the s-electrons at the nucleus, $\langle r^2 \rangle$ is the mean square radius of the nucleus, $Q_{\alpha\alpha}$ is the electric quadrupole moment defined by $Q_{\alpha\alpha} = \frac{1}{e}\int \rho(\vec{r})(3x_\alpha^2 - r^2)\partial^3 r$, and $V_{\alpha\alpha}$ are the three components of the electric field gradient. $V_{\alpha\alpha}$ is related to $\Phi_{\alpha\beta}$ by the equations

$$\Phi_{\alpha\alpha} = V_{\alpha\alpha} + \tfrac{1}{3}(\Delta\Phi)\delta_{\alpha\alpha}$$

and

$$\sum V_{\alpha\alpha} = 0.$$

The electric field gradient is normally written in terms of V_{ZZ} and η, where V_{ZZ} is the electric field gradient along the z axis, and η is the asymmetry parameter defined by

$$\eta = \frac{V_{xx} - V_{yy}}{V_{zz}}.$$

In the case of an axially symmetric electric field gradient, where $V_{xx} = V_{yy}$, the energy of the interaction involving E_Q is given by

$$E_Q = \frac{3M^2 - I(I+1)}{4I(2I-1)} eQV_{zz} \qquad 2.3$$

where I and M are the quantum numbers of the total angular momentum and the z component, respectively, of the nucleus.

From this equation the quadrupole coupling frequency ω_Q and quadrupole constant ν_Q are defined as

$$\omega_Q = \frac{eQV_{zz}}{4I(2I-1)\hbar} \qquad 2.4a$$

$$\nu_Q = \frac{eQV_{zz}}{\hbar}. \qquad 2.4b$$

2.1.2 The Magnetic Hyperfine Interaction

Consider a nucleus with a magnetic dipole $\vec{\mu}$ in a magnetic field $\vec{B}$. The interaction between $\vec{\mu}$ and $\vec{B}$ can have two effects: (i) it can lift the degeneracy of the nuclear level into its *(2I + 1)* sub states or (ii) it can cause a precession of the nuclear spin.

The lifting of the degeneracy of the nuclear level will be discussed first. The energy of the interaction is written as

$$\begin{aligned} E_{magn} &= \langle I, M | -\mu_Z B_Z | I, M \rangle \\ &= -\gamma B_Z \hbar M \end{aligned} \qquad 2.5$$

and it is observed that the nucleus in the presence of this $\vec{B}$ field gets split into *(2I + 1)* states. The level splittings are equidistant and the difference in energy between two neighbouring *m* states are

$$\Delta E = -\gamma \hbar B_z.$$

For the nuclear precession, the nuclear spin will precess about the magnetic field with a frequency $\omega_L = -\gamma B_z$ where γ is the gyromagnetic ratio.

This can be written in terms of the wave function of the nuclear state $\Psi(0)$, and the time evolution operator $\Lambda(t)$ as

$$\Psi(t) = \Lambda(t)\Psi(0)$$

where $\Lambda(t)$ is defined as

$$\Lambda(t) = \exp\left(-\frac{iHt}{\hbar}\right).$$

H, the Hamiltonian operator, is defined by

$$H = -\gamma I_z B_z .$$

2.2 THE MÖSSBAUER EFFECT

2.2.1 Principle of the Mössbauer Effect

Suppose that a γ-photon were to interact with an atomic nucleus. If the energy of the γ-photon, E_0 was equal to the energy needed to excite the nucleus from the ground state, of energy E_g, to a higher level, of energy E_e, i.e. $E_0 = E_e - E_g$, then the γ-photon will be absorbed. One can then imagine that if a nucleus decays from the excited state to the ground state, with the emission of a γ-photon of energy E_0, another identical nucleus will absorb the γ-photon and make the transition from the ground state to the excited state, i.e. there will be resonance fluorescence. This process is illustrated in Fig. 2.1.

However, this is not the case in general. When a nucleus undergoes a transition $|i\rangle \rightarrow |f\rangle$ by photon emission, conservation of linear momentum requires that the nucleus recoils with momentum $\vec{p}_N$ and energy $E_R = \frac{E_0^2}{2Mc^2}$. The energy carried away by the emitted γ-photon is therefore not the transition energy E_0, but a reduced energy $E_\gamma = E_0 - E_R$, with its linear momentum $p_\gamma = \frac{E_\gamma}{\hbar}$. This means that the energy of the emitted γ will be decreased by the amount E_R. A similar effect occurs when the absorbing nucleus absorbs the γ-photon, since the absorbing nucleus will also recoil with an energy $E_R' = \frac{E_0^2}{2Mc^2}$ due to the conservation of linear momentum, and the energy of the γ required to cause the transition will be $E_\gamma' = E_0 + E_R'$.

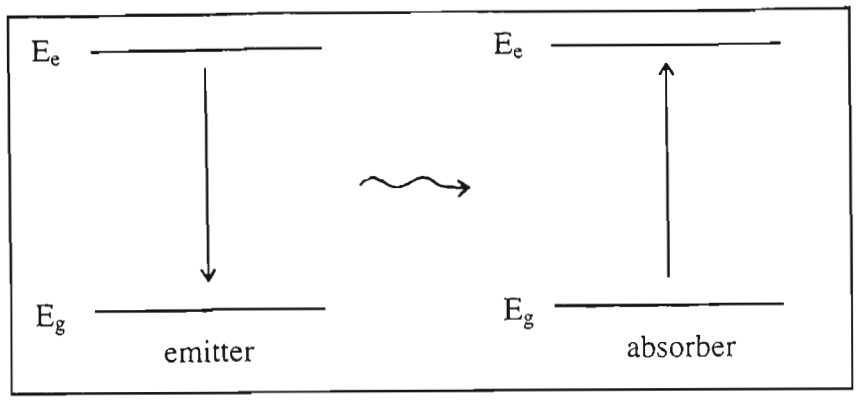

Fig. 2.1. Mössbauer Resonance Fluorescence between Emitter and Absorber

Thus, recoil of the source on emitting the γ-photon results in the energy carried away by the photon being less than the resonance energy by an amount equal to the energy of recoil $E_R = \frac{E_0^2}{2Mc^2}$. On the other hand, recoil of the absorber on accepting the γ-photon means that for resonance absorption to occur, the energy of the incident quantum must be greater than the resonance energy by the same amount. Hence, the maxima of the emission and absorption profiles are removed from each other by an amount $2E_R$ and if $2E_R >> \Gamma$, where Γ is the natural line width of the emission and absorption profiles, resonance fluorescence cannot occur. R.L.Mössbauer, in 1957 [MOS58], showed that this loss in energy to nuclear recoil could be avoided when the nucleus was embedded in a crystal lattice.

It is possible to describe the vibrational spectrum of atoms in a solid (the phonon spectrum) on the basis of a set of oscillators in potential wells, with characteristic frequencies which are multiples of some frequency ω_s (the Einstein model). The transition of an oscillator from a higher level to a lower level is accompanied by the absorption of phonons. The

opposite process is related to the excitation (emission) of phonons. In the general case, the phonon spectrum consists of a set of characteristic frequencies (the Debye model), and it is a function of the structure of the crystal, and can be characterised by some average vibrational energy $\hbar\omega_{av}$. As long as the energy of recoil during the emission or absorption of γ-quanta is less than the bonding energy between atoms in crystals, these bonds will not be broken. In such a case, all the excitations related to the momentum of recoil (due to the emission or absorption of the γ-quanta) becomes collective, and all the oscillators remain in their potential wells. Under these conditions they can only pass from one energy level to another. Therefore, there is no transfer of momentum to the oscillator, and the momentum of recoil is absorbed by the entire lattice as a unit. However, part of the transition energy can be transferred to the oscillators, i.e. it can be used to excite phonons. Then the direct relation between the energy and the momentum of recoil, which is the characteristic for a transition in a free nucleus, breaks down. Only in the particular case when excitation of phonons do not take place, such a direct relation holds and both the energy and the momentum are distributed between the γ-quantum and the crystal as a unit.

The momentum of recoil of a free nucleus mv is now essentially equal to the momentum of recoil of the crystal MV where M is the mass of the entire crystal. This means that the energy of recoil of the crystal, $E_{crys} = \frac{MV^2}{2}$, is $\frac{M}{m}$ times smaller than the energy of recoil of a single free nucleus, E_R. . Thus, in the case of a crystal recoiling as a unit, and without the excitations of phonons, the condition $E_{crys} << \Gamma$ becomes valid, and it is possible to

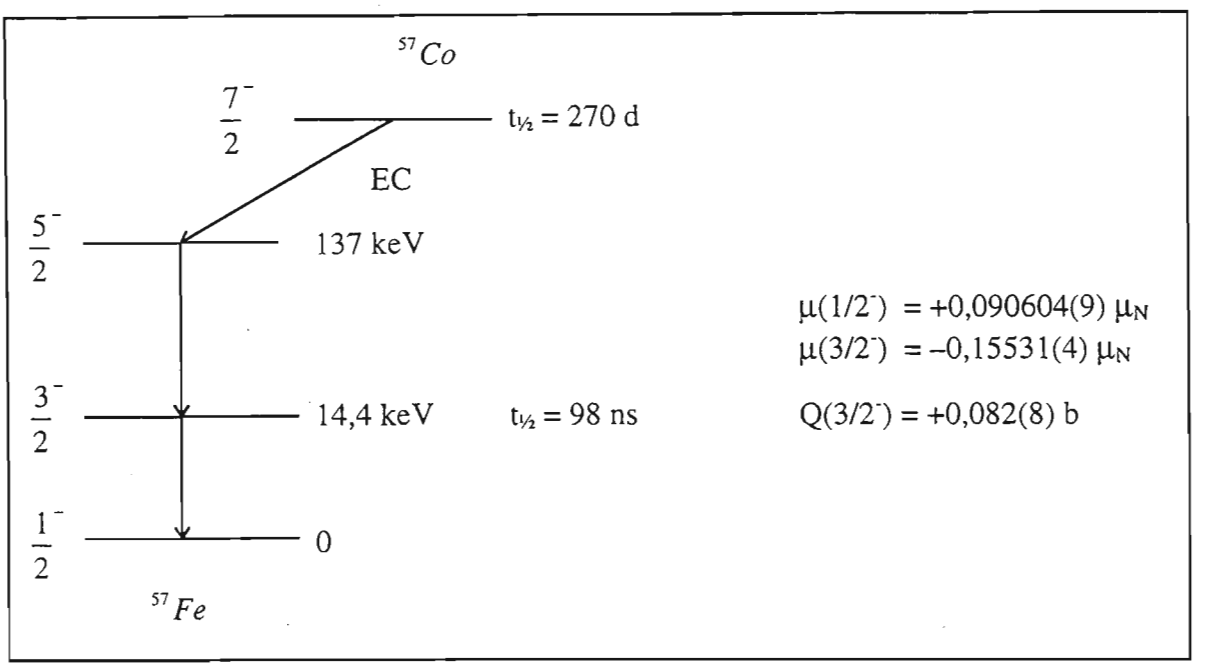

Fig. 2.2. Decay Scheme of ^{57}Co.

observe nuclear γ-resonance fluorescence on lines of natural width, i.e. the Mössbauer Effect.

Due to practical reasons, the absorption generally occurs when the nucleus makes the transition from the ground state to the first excited state. Therefore emission processes which lead only to the ground state should be considered.

In the present study, ^{57}Fe were used as the probe nuclei. The nuclear decay scheme of ^{57}Co to this isotope is shown in Fig. 2.2; the Mössbauer line results from the 14.4 keV $\frac{3}{2}^- \rightarrow \frac{1}{2}^-$ transition. The nuclear properties of the levels are shown above.

2.2.2 The Debye-Waller Factor

The fraction of recoil-free emitted gamma rays (those which do not create phonons in the crystal) is called the Debye-Waller factor f_D. Using the Debye model for phonons in a crystal, this factor can be written as, in the case of low temperatures [SHA96]

$$f_D(T) = \exp\left\{-\frac{\hbar^2 k^2}{2M}\frac{3}{2k_B\Theta}\left[1+\frac{2\pi^2}{3}\left(\frac{T}{\Theta}\right)^2\right]\right\}$$

where k is wave number of the emitted radiation, k_B is the Boltzmann factor, and Θ is the Debye temperature.

$f_D(T)$ is strongly dependent on the emitter temperature, and takes its maximum value at T = 0 K.

2.2.3 The Isomer Shift

In a typical Mössbauer experiment, the emitting nucleus (the source) moves at some velocity v relative to the absorbing nucleus (the absorber). Continuing with the notation used in §2.2.1, we assume that the source and absorber nuclei have the energies E_g and E_e associated with the ground state and the first excited state of the nuclei.

Let the frequency ω_0 be defined as

$$\omega_0 = \frac{E_e - E_g}{\hbar}$$

If a stationary source emits a γ ray of energy $\hbar\omega_0$, then a source moving with a velocity v will emit a γ ray of energy

$$\left[\hbar\omega_0\left(1+\frac{v}{c}\right) \quad + \quad \ldots \quad\right]$$

along the direction of its motion.

Including the effect of the change in mean square radius $\langle r^2 \rangle$ of the nucleus from the excited state to the ground state, the energy of the γ ray emitted by the source will be

$$E(\gamma_s) = \hbar\omega_0\left(1+\frac{v}{c}\right) + \frac{Ze^2}{6\varepsilon_0}|\Psi_s(0)|^2\left(\langle r_e^2\rangle - \langle r_g^2\rangle\right). \qquad 2.6$$

In Eqn. (2.6), $\langle r_e^2 \rangle$ and $\langle r_g^2 \rangle$ are the average radii of the nucleus in the excited and ground states, respectively, and $|\Psi_s(0)|^2$ is the probability of finding the *s* electrons of the probe atom at the nucleus.

Similarly, the energy of the γ needed to excite the stationary absorber ($v = 0$) will be

$$E(\gamma_a) = \hbar\omega_0 + \frac{Ze^2}{6\varepsilon_0}|\Psi_a(0)|^2\left(\langle r_e^2\rangle - \langle r_g^2\rangle\right). \qquad 2.7$$

Here $|\Psi_a(0)|^2$ is the probability of finding the *s* electrons of the probe atom at the nucleus of the absorber.

In order for there to be resonance absorption, $E(\gamma_s) = E(\gamma_a)$, we obtain the result that the source must then move at the velocity v_{res} with respect to the absorber,

$$v_{res} = \frac{Ze^2c}{6\varepsilon_0\hbar\omega_0}\left(|\Psi_a(0)|^2 - |\Psi_s(0)|^2\right)\left(\langle r_e^2\rangle - \langle r_g^2\rangle\right). \qquad 2.8$$

This resonant velocity represents the relative energy shift in the transition energy between emitter and absorber, and is referred to as the isomer shift δ. In the present work, with the source kept stationary, the only factors that contribute to changes in the isomer shifts are the wave functions $\Psi_a(0)$ of the electrons at the probe nuclei in the various absorbers.

2.2.4 The Electric Quadrupole Interaction

The effects of the electrical quadrupole interaction between the electric quadrupole moment, Q, of the probe nucleus and the electric field gradient at the nucleus will be discussed specifically in terms of the ^{57}Fe nucleus. From Eqn. (2.3), in the presence of an electric field gradient, the energy levels of the ^{57}Fe nucleus will be split into the levels shown in Fig. 2.3. The splittings depend on M^2 , rather than M, and therefore only two absorption (emission) lines will be occur. Using Eqn. (2.3), the energy difference between the two levels is given by

$$\Delta E = \hbar\omega_0 \frac{\delta v}{c}. \qquad 2.9$$

Here, $\delta v = v_2 - v_1$, where v_1 and v_2 are the resonant velocities at which absorption line 1 and absorption line 2 occurs.

Using Eqn. (2.4), δv can be rewritten as

$$\delta v = \frac{eQV_{zz}c}{2\hbar\omega_0}. \qquad 2.10$$

Thus, if the experiment yields results for δv, then the z component of the electric field gradient, V_{zz}, can be determined.

For powder samples, the orientation of the electric field gradient is randomly distributed, i.e. there does not exist any correlation between the electric field gradient and the direction of emission of the γ ray. As a result, in calculating the intensities for the different transitions using the nuclear matrix elements for the transitions, it is found that the intensities of both the absorption lines are equal.

2.2.5 The Magnetic Dipole Interaction

The interaction of the magnetic dipole moment of the nucleus with a magnetic field external to the nucleus leads to equidistant splittings of the nuclear levels. The splitting for the case of ^{57}Fe is shown in Fig. 2.4. Due the selection rules that $\Delta m = 0, \pm 1$, six of the eight possible transitions are allowed.

The energy required by the absorber to make a transition from one of the sublevels of the ground state to one of the sublevels of the first excited state is given by

$$E_o = \hbar\omega_0 - \left(\frac{\upsilon_e}{I_e} M_e - \frac{\upsilon_g}{I_g} M_g\right) B .$$

Ideally, the source should not be in the presence of any magnetic fields or electric field gradients. The energy of the γ ray emitted will then be

$$E_S = \hbar\omega_0 \left(1 + \frac{v}{c}\right).$$

In order for resonance absorption to occur, E_o must be set equal to E_s. The condition for resonance absorption is then,

$$v_{res} = -\frac{c}{\hbar\omega_0}\left(\frac{\upsilon_e}{I_e}M_e - \frac{\upsilon_g}{I_g}M_g\right)B \qquad 2.11$$

i.e. the source must move at one of six velocities defined by the above equation in order to display the Mössbauer Effect.

For powder samples, the orientation of the magnetic field is randomly distributed, with the result that the intensity of the six absorption lines will display the ratio of 3:2:1:1:2:3.

2.2.6 The Second Order Doppler Shift

If one uses the relativistic formula to evaluate the Doppler effect, then the frequency of the emitted or absorbed γ ray will be

$$\omega = \omega_0 \frac{\sqrt{1-\frac{v^2}{c^2}}}{1-\frac{v}{c}} = \frac{\omega_0}{1-\frac{v}{c}}\left(1-\frac{v^2}{2c^2}+\ldots\right). \qquad 2.12$$

In a crystal lattice, during the lifetime of the excited nucleus, the lattice would experience oscillations with typical values for the period of oscillations being 10^{-13} s. Since this period is much smaller than the lifetime, τ_N $(10^{-7}\ s)$, of the ^{57}Fe Mössbauer state, the average velocity of the atoms in the lattice during a Mössbauer transition will be zero.

From Eqn. (2.12) we obtain the average frequency of emission $\langle\omega\rangle$ as

$$\langle\omega\rangle = \omega_0 - \frac{\omega_0}{Mc^2}\frac{\langle Mv_{lat}^2\rangle}{2}.$$

Here, $\frac{\langle Mv_{lat}^2\rangle}{2}$ is the average value of the kinetic energy of any one lattice point.

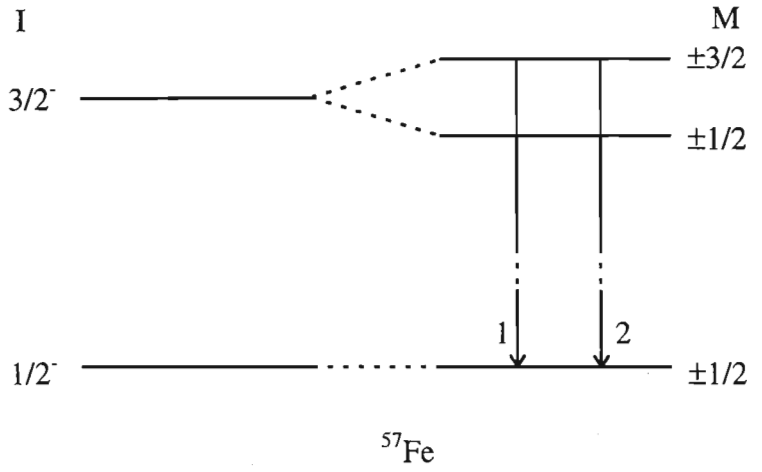

Figure 2.3. Quadrupole splitting of the ^{57}Fe Mössbauer transition.

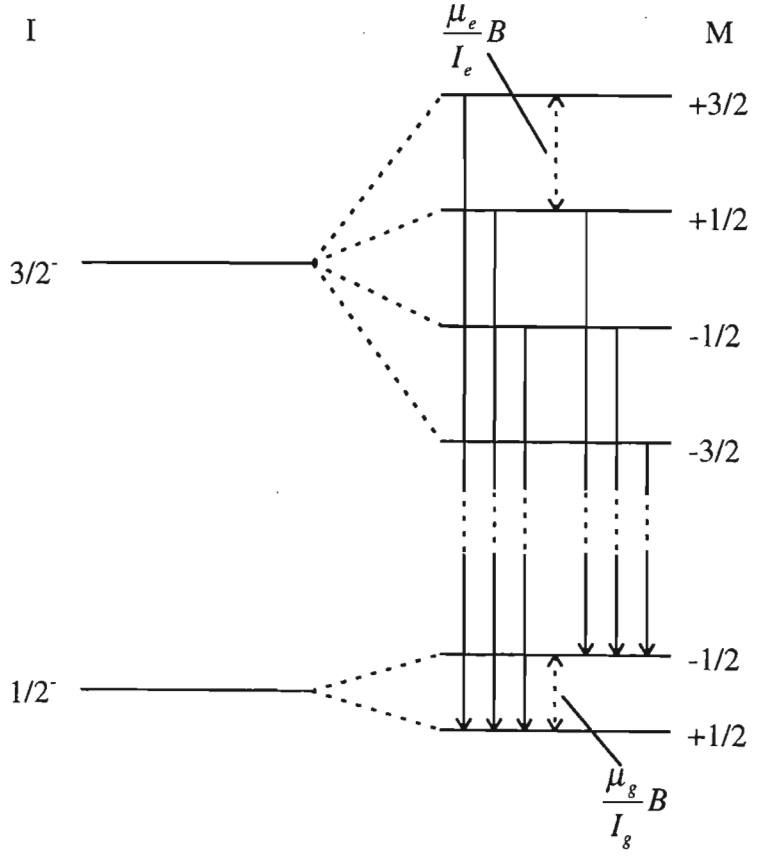

Figure 2.4. Splittings of the nuclear levels of ^{57}Fe in a $\vec{B}$ field.

For an harmonic oscillator, the average kinetic energy is half the total energy. Writing this in terms of the molar energy, one obtains

$$E_{mol} = 2N_A \frac{M\langle v_{lat}^2 \rangle}{2}$$

where N_A is Avagadro's constant.

Then

$$\langle \omega \rangle = \omega_0 - \omega_0 \frac{E_{mol}}{Mc^2 2N_A}.$$

Using the definition for the heat capacity, $C_{mol} = \frac{dE_{mol}}{dT}$, and differentiating $\langle \omega \rangle$ with respect to the temperature T, the frequency shift per degree is obtained,

$$\frac{d\langle \omega \rangle}{dT} = -\omega_0 \frac{C_{mol}(T)}{Mc^2 2N_A}. \qquad 2.13$$

The experimental observation of this frequency shift is then that the isomer shift decreases linearly with increasing temperature of the sample.

2.3 TIME DIFFERENTIAL PERTURBED ANGULAR CORRELATIONS

2.3.1 Principle of Perturbed Angular Correlations

Suppose that a nucleus decays from an initial state $|I_i, M_i\rangle$ to an intermediate state $|I, M\rangle$ by emitting a γ- ray, γ_1, with wave vector $\vec{k}_1$ and polarisation σ_1, and then to a final state $|I_f, M_f\rangle$ by emitting a second γ- ray, γ_2, with wave vector $\vec{k}_2$ and polarisation σ_2, as shown in Fig. 2.5.

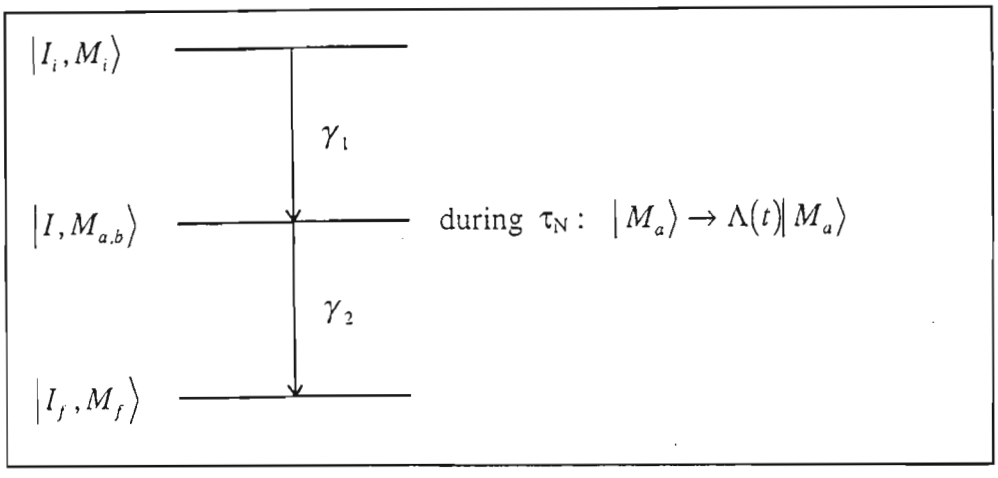

Fig. 2.5. The γ-γ cascade of a TDPAC probe, where the intermediate state has a mean lifetime τ_N

If the nucleus is subject to an hyperfine interaction, such that when the nucleus is in the intermediate state, a substantial repopulation or phase change of the magnetic substates of the intermediate state results before the emission of the γ_2, then the time evolution of the substate will be

$$|M_a\rangle \rightarrow \Lambda(t)|M_a\rangle = \sum_{M_b} |M_b\rangle\langle M_b|\Lambda(t)|M_b\rangle$$

where $\Lambda(t)$ is the time-development operator. The shorthand notation for the matrix element is used in the equation and the index a refers to the initially populated intermediate sublevel and b to the intermediate sublevels that evolve from $|M_a\rangle$.

With H_1 and H_2 representing the Hamiltonian operators for the emission of the γ_1 and the γ_2, respectively, the angular correlation in terms of the matrix elements for a specific transition from M_i to M_f is then

$$W(\vec{k}_1,\vec{k}_2,t) = \sum_{\substack{M_i,M_f,\sigma_1,\sigma_2,\\ M_a,M_a',M_b,M_b'}} \langle M_f|H_2|M_b\rangle\langle M_b|\Lambda(t)|M_a\rangle\langle M_a|H_1|M_i\rangle \times \langle M_f|H_2|M_b'\rangle^*\langle M_b'|\Lambda(t)|M_a'\rangle^*\langle M_a'|H_1|M_i\rangle^*$$

from which the following equation results

$$W(\vec{k}_1,\vec{k}_2,t) = \sum_{k_1,k_2,N_1,N_2} A_{k_1}(1)A_{k_2}(2)G_{k_1k_2}^{N_1N_2}(t)\frac{1}{\sqrt{(2k_1+1)(2k_2+1)}}\times \times Y_{k_1}^{N_1*}(\theta_1,\phi_1)Y_{k_2}^{N_2}(\theta_2,\phi_2) \qquad 2.14$$

The coefficient $A_{k1}(1)$ depends only on the first transition and the coefficient $A_{k2}(2)$ depends only on the second. Their values are tabled [FER65].

The perturbation factor is defined as

$$G_{k_1k_2}^{N_1N_2}(t) = \sum_{M_a,M_b}(-)^{2I+M_a+M_b}\sqrt{(2k_1+1)(2k_2+1)}\times \times \begin{pmatrix} I & I & k_1 \\ M_a' & -M_a & N_1 \end{pmatrix}\begin{pmatrix} I & I & k_2 \\ M_b' & -M_b & N_2 \end{pmatrix}\langle M_b|\Lambda(t)|M_a\rangle\langle M_b'|\Lambda(t)|M_a'\rangle^* \qquad 2.15$$

where the terms in the brackets are the Wigner 3j symbols, and are defined as

$$\begin{pmatrix} j_1 & j_2 & j_3 \\ m_1 & m_2 & m_3 \end{pmatrix} = (-)^{j_1-j_2-m_3}\frac{1}{\sqrt{2j_3+1}}(j_1,j_2,m_1,m_2|j_3,-m_3).$$

The bracket on the right of this definition are the Clebsch-Gordan coefficients.

For cases where the electric field gradients, which give rise to the perturbations, do not have any specific symmetry, the angular correlation is calculated numerically from Eqn. (2.14) and Eqn. (2.15).

For a static asymmetric electric field gradient, the perturbation function is written as [BOL87]

$$G_2(t) = \sum_{n=0}^{3} S_{2n}(\eta)\cos\left[\omega_n(\eta, \nu_Q)t\right]. \qquad 2.16$$

In Eqn. (2.16), the transition frequencies ω_n are related to the quadrupole coupling constant ν_Q, defined in Eqn. (2.4(b)), by

$$\omega_n = g_n(\eta)\nu_Q. \qquad 2.17$$

The amplitudes S_{2n} in Eqn. (2.16) and the functions $g_{ny}(\eta)$ in Eqn. (2.17) are calculated numerically [KAJ73].

2.3.2 The Perturbation Factor in the Case of an Axially Symmetric Interaction.

Assume that that the z quantisation axis is in the direction of an axially symmetric field. Then the matrix element of the time evolution operator when the nucleus is in the intermediate state is given by

$$\left\langle M_b\left|\Lambda(t)\right|M_a\right\rangle = \left\langle M_b\left|\exp\left(-\tfrac{i}{\hbar}Ht\right)\right|M_a\right\rangle =$$
$$= \exp\left[-\tfrac{i}{\hbar}E(M)t\right]\delta_{M,M_a}\delta_{M,M_b}$$

H is the Hamiltonian of the interaction and $E(M)$ is the corresponding eigen value.

The perturbation factor then becomes

$$G_{k_1k_2}^{NN}(t) = \sum_{M} \sqrt{(2k_1+1)(2k_2+1)} \begin{pmatrix} I & I & k_1 \\ M' & -M & N \end{pmatrix} \begin{pmatrix} I & I & k_2 \\ M' & -M & N \end{pmatrix} \times \times \exp\left\{-\tfrac{i}{\hbar}\left[E(M) - E(M')\right]t\right\}$$

If the interaction was a electric quadrupole interaction, then

$$E_Q(M) - E_Q(M') = 3\left|M^2 - M'^2\right|\hbar\omega_Q .$$

The perturbation factor then becomes

$$G_{k_1k_2}^{NN}(t) = \sqrt{(2k_1+1)(2k_2+1)} \sum_{M} \begin{pmatrix} I & I & k_1 \\ M' & -M & N \end{pmatrix} \begin{pmatrix} I & I & k_2 \\ M' & -M & N \end{pmatrix} \times \times \exp\left(-3i\left|M^2 - M'^2\right|\omega_Q t\right)$$

which can be written in the more clear form as

$$G_{k_1k_2}^{NN}(t) = \sum_{n} s_{nN}^{k_1k_2} \cos n\omega_Q^0 t \qquad 2.18$$

where

$\omega_Q^0 = 3\omega_Q$ and $n = \left|M^2 - M'^2\right|$ for integral I

$\omega_Q^0 = 6\omega_Q$ and $n = \left(\tfrac{1}{2}\right)\left|M^2 - M'^2\right|$ for half integral I

and

$$s_{nN}^{k_1k_2} = \sqrt{(2k_1+1)(2k_2+1)} \sum_{M,M'} \begin{pmatrix} I & I & k_1 \\ M' & -M & N \end{pmatrix} \begin{pmatrix} I & I & k_2 \\ M' & -M & N \end{pmatrix}.$$

In the special case where a polycrystalline sample is used, the perturbed angular correlation function can be written as

$$W(\theta,t) = \sum_{k\ even}^{k_{max}} A_{kk} G_{kk}(t) P_k(\cos\theta) \qquad 2.17$$

with $$G_{kk}(t) = \sum_{n=0}^{n_{max}} s_{kn} \cos n\omega_Q^0 t \qquad 2.17a$$

where

$$s_{kn} = \sum_{M,M'} \begin{pmatrix} I & I & k \\ M' & -M & M-M' \end{pmatrix}^2 . \qquad 2.17b$$

III MÖSSBAUER SPECTROSCOPY AND RELATED MEASUREMENTS ON Fe-V_2O_5

3.1 EXPERIMENTAL

3.1.1 Production of Fe-V_2O_5 samples

The Mössbauer measurements required Fe to be introduced into the V_2O_5 lattice. This was achieved using the solid state reaction similar to those used by other authors [ABD69, BAR74, BAR85, BUR76, BUR78, KOR82 and PEK80].

Appropriate molar percentages of V_2O_5 and natural Fe powder were mechanically mixed in a rotating glass flask for one hour for each sample, with glass beads used to agitate the powders. Each mixture was then placed in a borosilicate test tube in the furnace for six hours at a temperature of 1023 K. This temperature was chosen so that it was above the melting point of V_2O_5 of 963 K. The atmosphere of the furnace was air, except for the sample with 15% Fe in the melt, where a vacuum of 2×10^{-2} *mBar* was present. Each melt was allowed to cool to room temperature whilst still in the furnace, and then extracted from the test tube and ground into powder.

The furnace shown in Fig. 3.1 was specifically designed for this melting process with the maximum temperature of the furnace designed to be 1473 K.

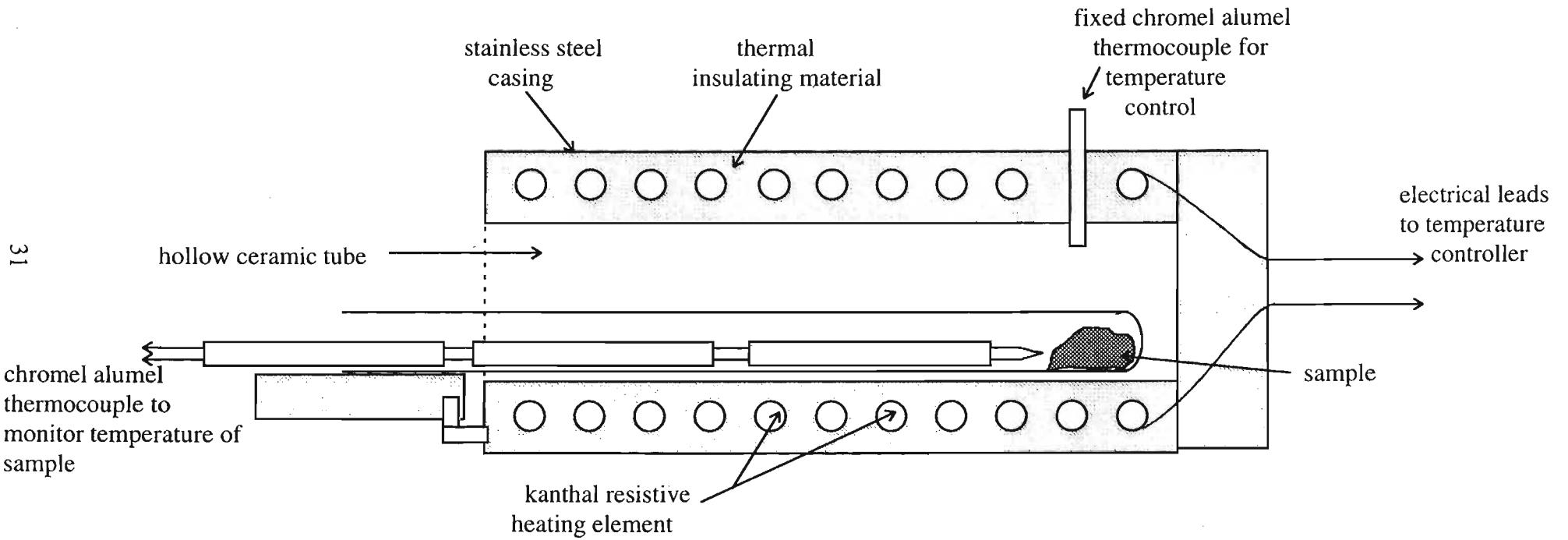

Fig. 3.1. Schematic design of furnace used to create Fe - V_2O_5 samples.

3.1.2. The Mössbauer Data Acquisition System

All the Mössbauer measurements were performed in transmission mode, using a ^{57}CoRh source. The measurements were made with a WISSEL GmBh Mössbauer system with the drive unit (MDU) coupled to a digital function generator operated in the triangular waveform. The error signal of the pickup coil in the MDU was 0.07% of the drive signal. The detection system comprised a proportional counter filled with *Kr-Co*$_2$ gas, a preamplifier, a linear amplifier, a single channel analyser (SCA) and a multichannel analyser. The windows of the SCA were set to select the 14,4 keV Mössbauer line. The multichannel analyser was operated in multichannel scaling mode with the start address and channel dwell time signals being fed externally from the MDU.

The computer code MOS3 was used to analyse the data, which was adapted from the Mössbauer code MOSFUN [MUL80] for interactive use. MOS3 uses a non-linear least squares routine to refine the parameters used to fit the spectrum. After each refinement step, the resulting fit could be immediately displayed to allow visual inspection of the fitted spectrum and changes could be made to the parameters whilst the program was running. A subroutine was also included so that parameters could be freed, fixed or changed in value after each refinement.

The parameters that could be refined were the positions, intensities and widths of the absorption lines, the base line, the geometrical factor and the folding point. In addition, relationships between parameters of the same type could be set using a correlation matrix in the input parameter file. For example, if the two lines of a quadrupole doublet were

required to be equal, this could be set in the correlation matrix, with one intensity parameter rather than two being then defined. However relationships between different types of parameters could not be set. For example, the intensity and width of a given absorption line could not be set to have a fixed ratio.

3.1.3 Design of sample holders and sample chamber

For room temperature Mössbauer measurements, the powders were loaded into a brass holder with 0,1 mm magnesium foil windows. A typical thickness and diameter of a sample was 0,5 mm and 10,0 mm, respectively.

For the temperature dependent Mössbauer measurements, a sample chamber and a sample holder with a heater element fixed onto it was constructed. The diagram of this apparatus is shown in Fig. 3.2. The walls of the sample chamber were constructed from aluminium of 5 mm thickness. Mylar foil was used as the gamma ray windows. The sample was placed in the brass holder, which was then bolted onto a copper plate which was in thermal contact with the heater filament.

The heater filament was made of nichrome wire of diameter 0,1 mm, turned into a coil, of total resistance 50 Ω. It was mounted onto the copper plate, as shown in Fig. 3.2, using the high temperature ceramic glue *Thermoguss*, which has the property of being an electrical insulator. Thin mica strips were used to separate the various turns of the nichrome wire as it was set into place on the copper plate. This heating unit was attached from the top cover of the chamber by means of a stainless steel rod.

To monitor the temperature of the sample, a chromel-alumel thermocouple was attached to the sample holder. The temperature of the sample was controlled by regulating the voltage supplied by an ac power supply to the heater element. The fluctuation in the temperature of the sample using this method of control was ±2.5 K.

3.1.4 Annealing of the Fe-V_2O_5 samples

In order to test the stability of the phases created, a few of the oxide samples were annealed after being produced. This was achieved by placing the powders in borosilicate test tubes, and maintaining them for 24 hours at 573 K in the furnace described in §3.1.1. Mössbauer spectra before and after annealing were taken on these samples.

3.1.5 X-Ray Diffraction Measurements of Fe-V_2O_5 samples

To complement the Mössbauer measurements, x-ray diffraction spectra of the samples were taken, with a Philips PW3710 diffractormeter equipped with a 10/50/47 goniometer. Cobalt radiation of mean wavelength 1.7901970 Å was used. A monochromatic crystal was used in the emergent beam so that only the K_α x-ray was allowed to strike the sample.

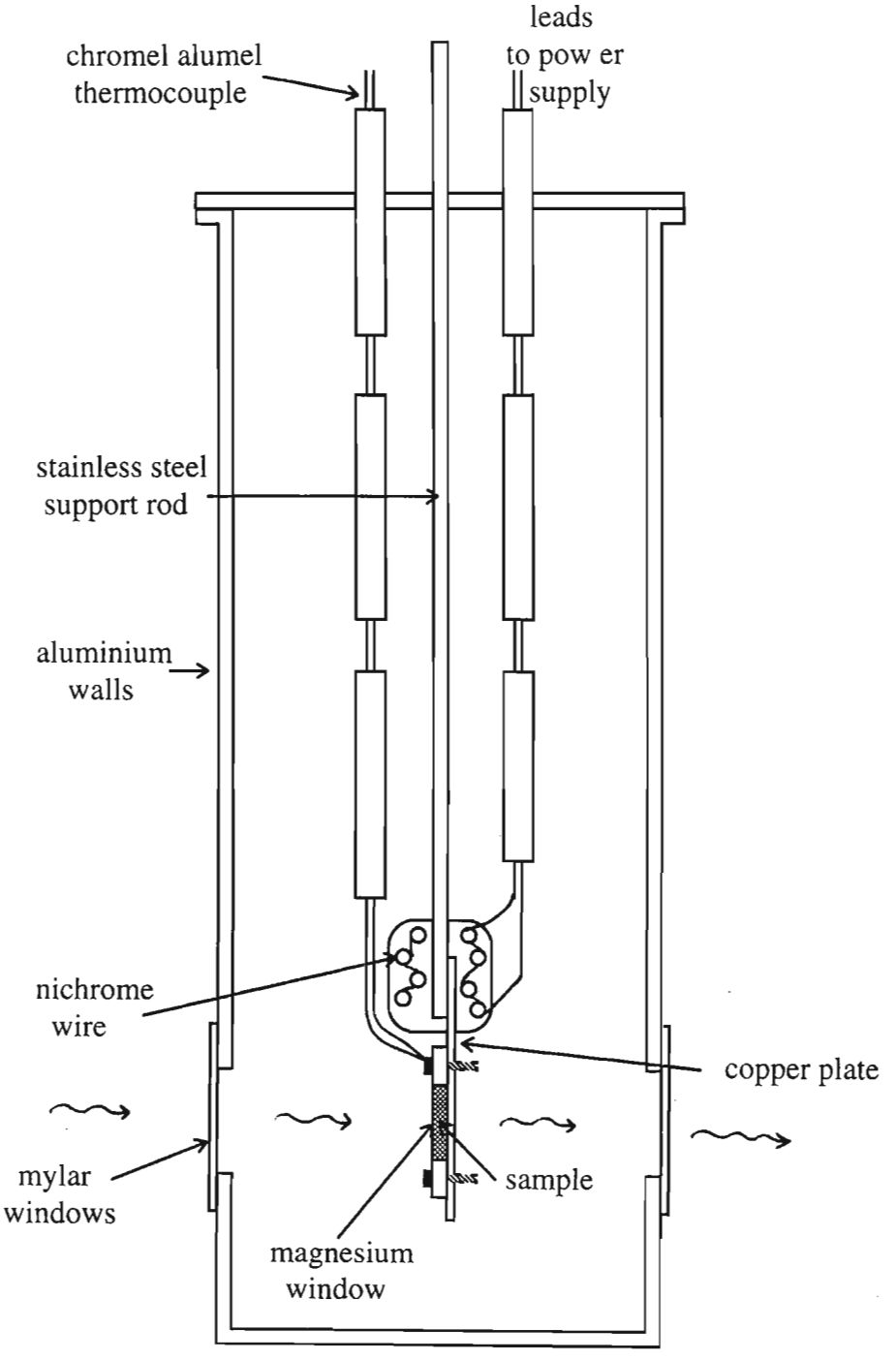

Fig. 3.2. Sample chamber with holder used for temperature dependent Mössbauer measurements.

3.1.6 The electric conductivity measurements on the Fe-V_2O_5 samples.

For a few samples, the electrical conductivity was measured as a function of the temperature. The apparatus designed to measure the electric conductivity is shown in Fig. 3.3. It consisted of a flat, 4 mm thick piece of mica with a cylindrical cavity of 5 mm diameter drilled through the centre. The cavity was then filled with the oxide. The bottom and top opening on the mica was covered using copper plates, which were held together through the mica sheet using brass nuts and bolts.

Two thin platinum wires, spaced 2 mm apart and parallel to each other, were fed through the side of the mica cylinder into the space of the cylinder. It was ensured that the platinum wires were not in electrical contact with each other, with the copper plates and with the brass bolts. In this way, electrical contact was made between the platinum wires only when a semiconducting or metallic powder was placed in the mica cylinder in such a way that it covered both the platinum wires.

A dc mains power supply was used to provide the potential between the two wires, and two Goldstar multimeters were used to determine the current through the powder and the voltage across the powder, respectively. A chromel-alumel thermocouple was silver soldered onto the bottom copper plate at the position shown in Fig. 3.3, to measure the temperature of the powder. The temperature gradient through the copper plate was neglected.

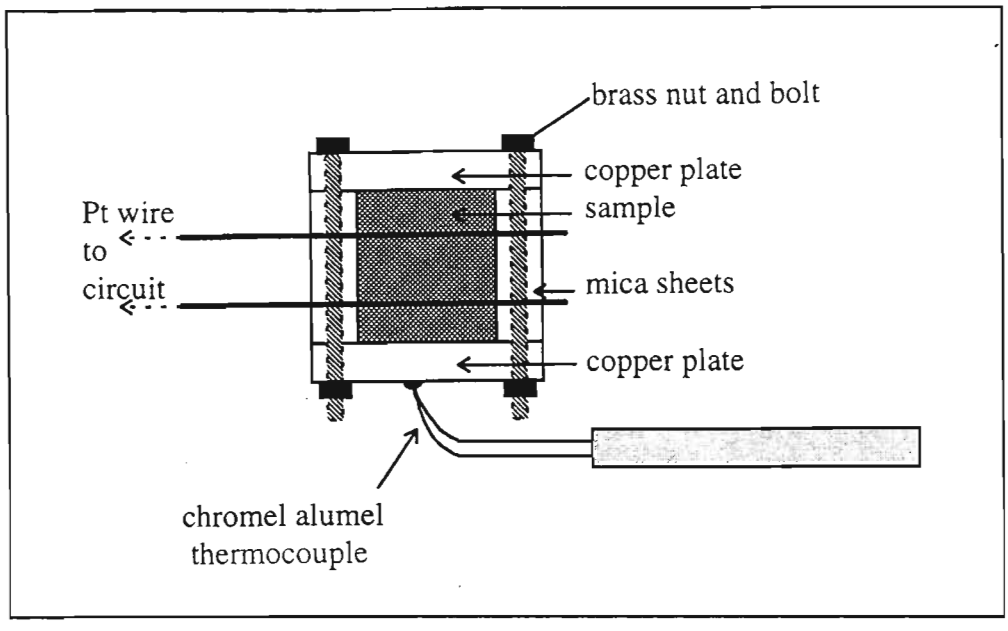

Fig. 3.3. Schematic diagram of apparatus used to measure the electric conductivity as a function of temperature.

To perform an electrical conductivity measurement, the entire unit with the powder loaded in the cylinder was placed in the furnace, and a dc voltage of 30V was applied across the two platinum wires. The furnace temperature was raised to 723 K, after which the heating was turned off and the unit was allowed to cool gradually. Current and voltage measurements as a function of the temperature was taken, starting when the powder temperature was at 673 K and ending when the powder had reached room temperature (300K).

3.2. RESULTS AND ANALYSIS

Three series of Mössbauer measurements were made, with different experimental factors controlled in each. These are detailed below as

i) measurements as a function of annealing temperature

ii) measurements as a function of the Fe concentration

iii) measurements as a function of the measuring temperature.

3.2.1. The Fitting Strategy for the Mössbauer Spectra

Before the results are presented, a discussion on the fitting strategy is necessary. The nature of the Mössbauer spectra collected were such that it would have been quite possible to obtain good fits using different combinations of several components, but this approach would not have led to valid physical interpretations.

Further, a general correlation of parameters between the various spectra were kept in mind. This meant that sudden changes in the fitted parameters were dealt with cautiously.

As a general rule, the following strategy was adopted in analysing the spectra.

1. If doublets were expected in the spectra, the ratio of the intensities of the two lines were taken to lie between 0.9 and 1.1, i.e. they were assumed to be symmetric.
2. If sextets were expected, then the inner two lines were set to have equal intensities. This condition was relaxed for the outer four lines, since their velocities did not lie within the region of interest for the vanadium- iron-oxide systems under investigation.
3. The lower limits for the line widths were equal to that of α-Fe and the upper limits were

set (arbitrarily) to thrice that of α-Fe.

4. For consistency, the set of parameters that were finally accepted were those that could simultaneously fit all the spectra in a series, allowing for the expected change in the isomer shift with temperature if necessary.
5. In most cases six doublets, labelled as a, b, c, d, e and f, and one sextet, g, were needed to fit the spectra.

3.2.2. Mössbauer measurements as a function of annealing temperature.

The first series of measurements were carried out to test the stability of the oxides in terms of their hyperfine parameters. Fe-V_2O_5 samples with Fe concentrations 5%, 15% and 80% were chosen for this study so that the full range of concentrations were spanned. The samples were annealed in air for 24 hours at a temperature of 573 K, which is about half that of the melting point of pure vanadium pentoxide. After annealing, the samples were first visually examined, and since no observable physical change were evident, the Mössbauer measurements were preceded with.

Two Mössbauer spectra were acquired for each of these annealed samples, one before and one after annealing. The spectra are shown in Fig. 3.4 (a), (b) and (c), together with the fitted components (as discussed in §3.2.1.).

The hyperfine parameters obtained by fitting these spectra are listed in Tables 3.1 (a), (b) and (c). Comparison of these parameters obtained before and after annealing show that the differences lie within the experimental accuracy. Further, from the physical appearance of

the fits, no significant changes could be observed in the spectra before and after annealing. This therefore implies that for these three samples, the properties investigated by the Mössbauer effect were well defined and not modified with heat treatment. Since the rest of the samples produced had Fe concentrations in the range spanned by these three samples, it was therefore assumed that all the samples were in stable states as defined by the Mössbauer measurements.

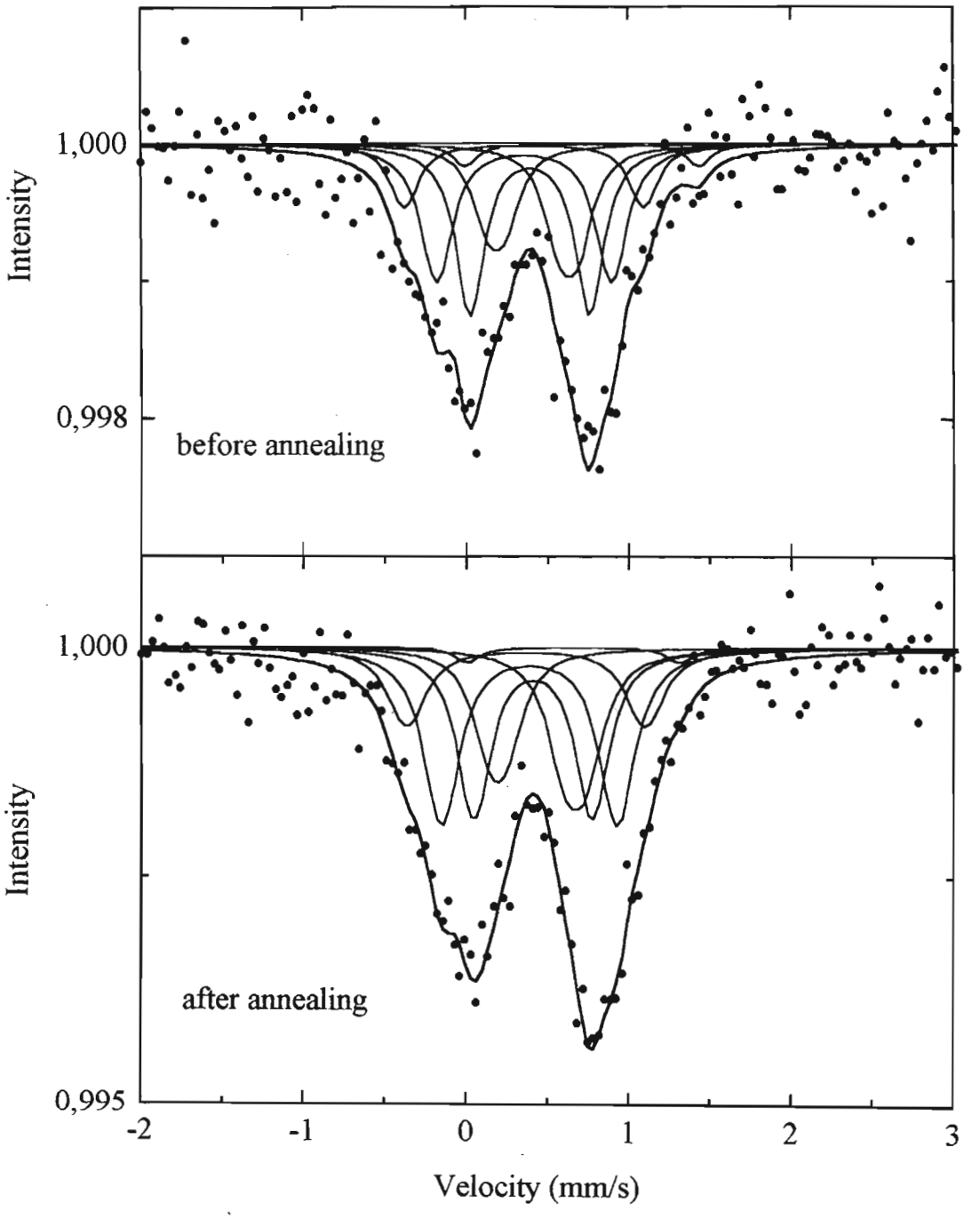

Fig. 3.4(a). Mössbauer spectra of sample with 5% Fe in the melt, before and after annealing.

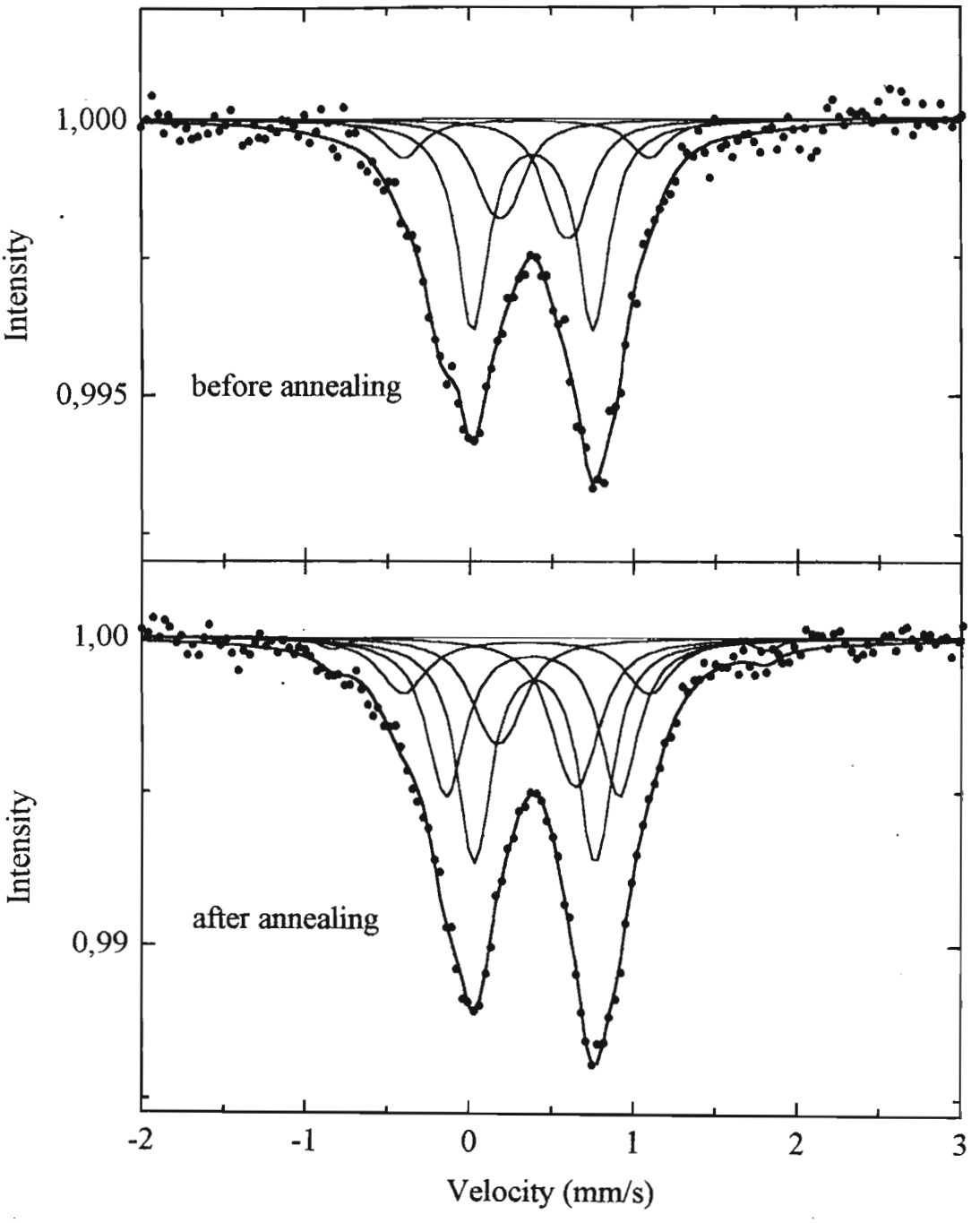

Fig. 3.4(b). Mössbauer spectra of sample with 15% Fe in the melt, before and after annealing.

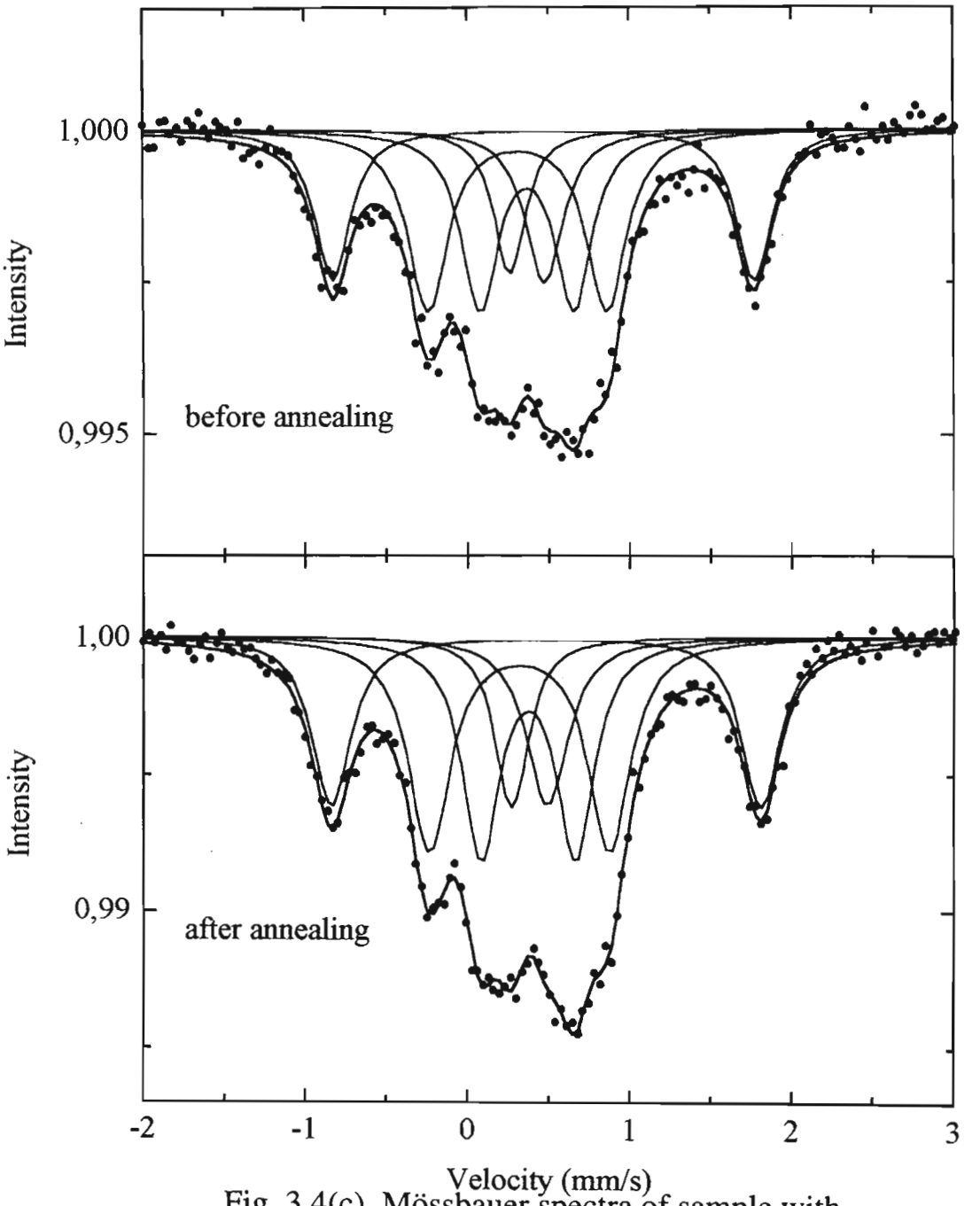

Fig. 3.4(c). Mössbauer spectra of sample with 80% Fe in the melt, before and after annealing.

Table 3.1(a). Hyperfine parameters of sample with 5% Fe in the melt.

	Before Annealing				After Annealing				
	δ (mm/s)	ΔE_Q (mm/s)	% I	Γ/2 (mm/s)	δ (mm/s)	ΔE_Q (mm/s)	% I	Γ/2 (mm/s)	assign ment
a	0,39(3)	0,73(5)	30(5)	0,10(3)	0,41(3)	0,72(5)	26(5)	0,12(3)	
b	0,35(4)	1,07(6)	28(5)	0,11(4)	0,38(4)	1,07(6)	30(5)	0,13(4)	
c	0,71(6)	1,44(8)	4(2)	0,09(6)	0,65(6)	1,30(8)	2(1)	0,09(6)	
d	0,35(4)	1,47(6)	12(3)	0,11(4)	0,36(4)	1,46(6)	14(4)	0,14(3)	
e	0,63(4)	0,11(6)	16(4)	0,11(4)	0,67(4)	0,13(6)	16(4)	0,13(4)	Fe_2O_3
f	0,19(4)	0,11(6)	12(3)	0,11(4)	0,19(4)	0,11(6)	12(3)	0,12(4)	

Table 3.1(b) Hyperfine parameters of sample with 15% Fe in the melt.

	Before Annealing				After Annealing				
	δ (mm/s)	ΔE_Q (mm/s)	% I	Γ/2 (mm/s)	δ (mm/s)	ΔE_Q (mm/s)	% I	Γ/2 (mm/s)	assign ment
a	0,38(3)	0,73(5)	34(6)	0,11(3)	0,40(3)	0,74(5)	31(6)	0,12(3)	
b	0,36(3)	1,06(5)	29(5)	0,13(3)	0,38(3)	1,05(5)	25(5)	0,13(3)	
d	0,35(4)	1,49(6)	8(3)	0,14(4)	0,34(4)	1,49(6)	11(3)	0,17(4)	
e	0,59(4)	0,11(6)	13(4)	0,13(4)	0,64(4)	0,10(6)	14(4)	0,14(4)	Fe_2O_3
f	0,18(4)	0,12(6)	11(3)	0,13(4)	0,17(4)	0,12(6)	11(3)	0,15(4)	
g*	0,48(6)	2,64(8)	6(2)	0,22(6)	0,48(6)	2,64(8)	8(3)	0,09(6)	Fe_2O_3

Table 3.1(c) Hyperfine parameters of sample with 80% Fe in the melt.

	Before Annealing				After Annealing				
	δ (mm/s)	ΔE_Q (mm/s)	% I	Γ/2 (mm/s)	δ (mm/s)	ΔE_Q (mm/s)	% I	Γ/2 (mm/s)	assign ment
a	0,36(5)	0,58(7)	11(3)	0,13(5)	0,37(4)	0,58(6)	11(3)	0,13(4)	
b	0,31(4)	1,10(6)	13(4)	0,14(4)	0,32(3)	1,10(5)	13(4)	0,15(3)	
e	0,47(5)	- -	11(3)	0,13(5)	0,49(4)	- -	10(3)	0,15(4)	Fe_2O_3
f	0,26(6)	- -	8(3)	0,11(6)	0,27(5)	- -	8(3)	0,11(5)	
g*	0,47(3)	2,59(5)	57(7)	0,12(3)	0,48(3)	2,64(5)	57(7)	0,14(3)	Fe_2O_3

g* is the magnetic splitting of the inner two lines of the sextet.

3.2.3 Mössbauer measurements as a function of Fe concentration.

The second series of Mössbauer measurements were taken as a function of the Fe concentration in the melt. The experimental spectra, together with their fitted components, are shown in Fig. 3.5 (a), (b) and (c). The parameters resulting from the most consistent fit to the data are listed in Tables 3.2 (a), (b), (c) and (d).

The results indicate that there is both a major similarity and a major difference between the spectra. The similarity is that the isomer shifts, quadrupole splittings and magnetic splitting of the various components remain the same for the different spectra, i.e. these parameters do not change with the Fe concentration, as is shown in Fig. 3.6 (a) and (b). This can also be seen in Table 3.2 (a) and (b), by comparing the mean of each parameter with the individual parameters.

The difference in the spectra is that the relative intensities of the various components change with Fe concentration, as is shown in Fig. 3.7. The intensities of the sample with 80% Fe in the melt are not shown, since for this refinement, doublets c and d were not included in the fit due to the closeness in velocity of the third and fourth line of sextet g to components c and d, and since e and f were treated as singlets rather than doublets. These approximations would give ratios for the intensities which would be to some extent not consistent with the other concentrations.

The following observations can be drawn from the intensities of the various components in the spectra:

1. Doublets a and b are the strongest for Fe concentrations below 30%,.
2. Doublets c and d have a slightly larger contribution at Fe concentrations below 30% in comparison with their concentrations above 30%.
3. Doublets e and f remain fairly constant. However for Fe concentrations less than 30% they are smaller in contribution to doublets a and b, whereas for larger Fe concentrations, they have the same intensity contribution.
4. Sextet g, which is attributed to Fe_2O_3, increases in intensity, as expected, as the Fe concentration increases.

The assignments of the components observed are presented in §3.2.6 in conjunction with the results from the the x-ray spectra.

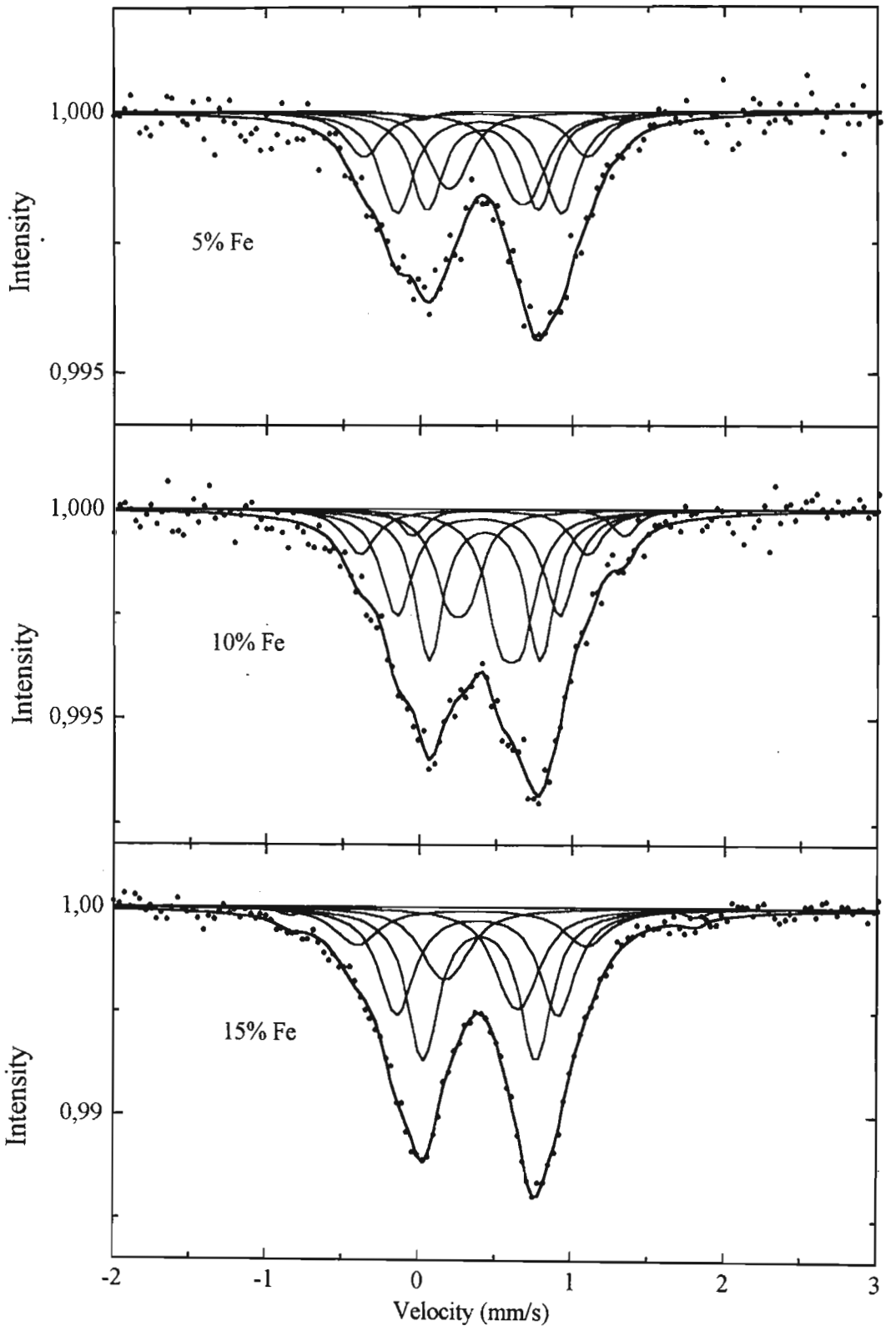

Fig. 3.5(a). Mössbauer spectra of samples with 5%, 10% and 15% Fe concentration

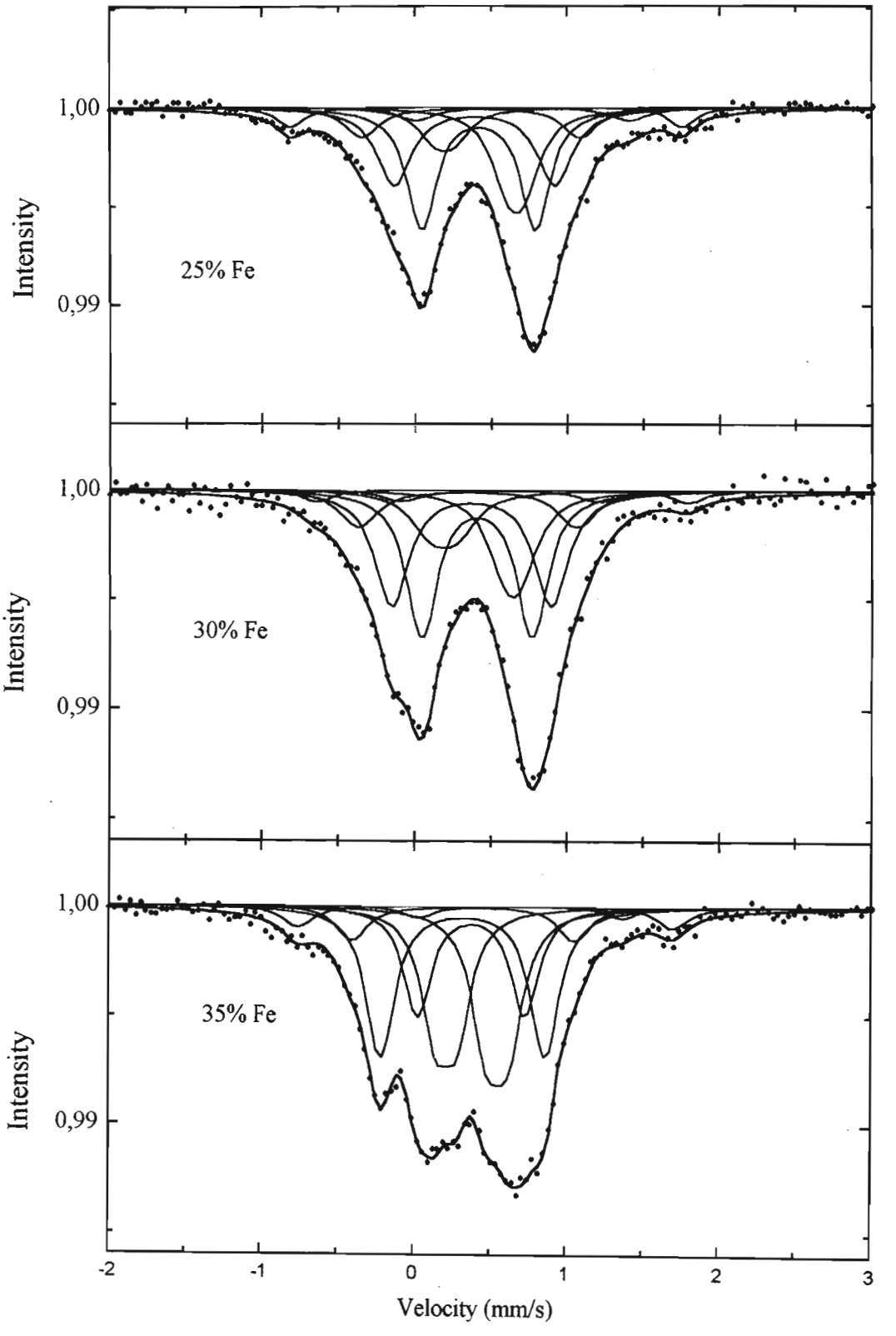

Fig. 3.5(b). Mössbauer spectra of samples with 25%, 30% and 35% Fe concentration

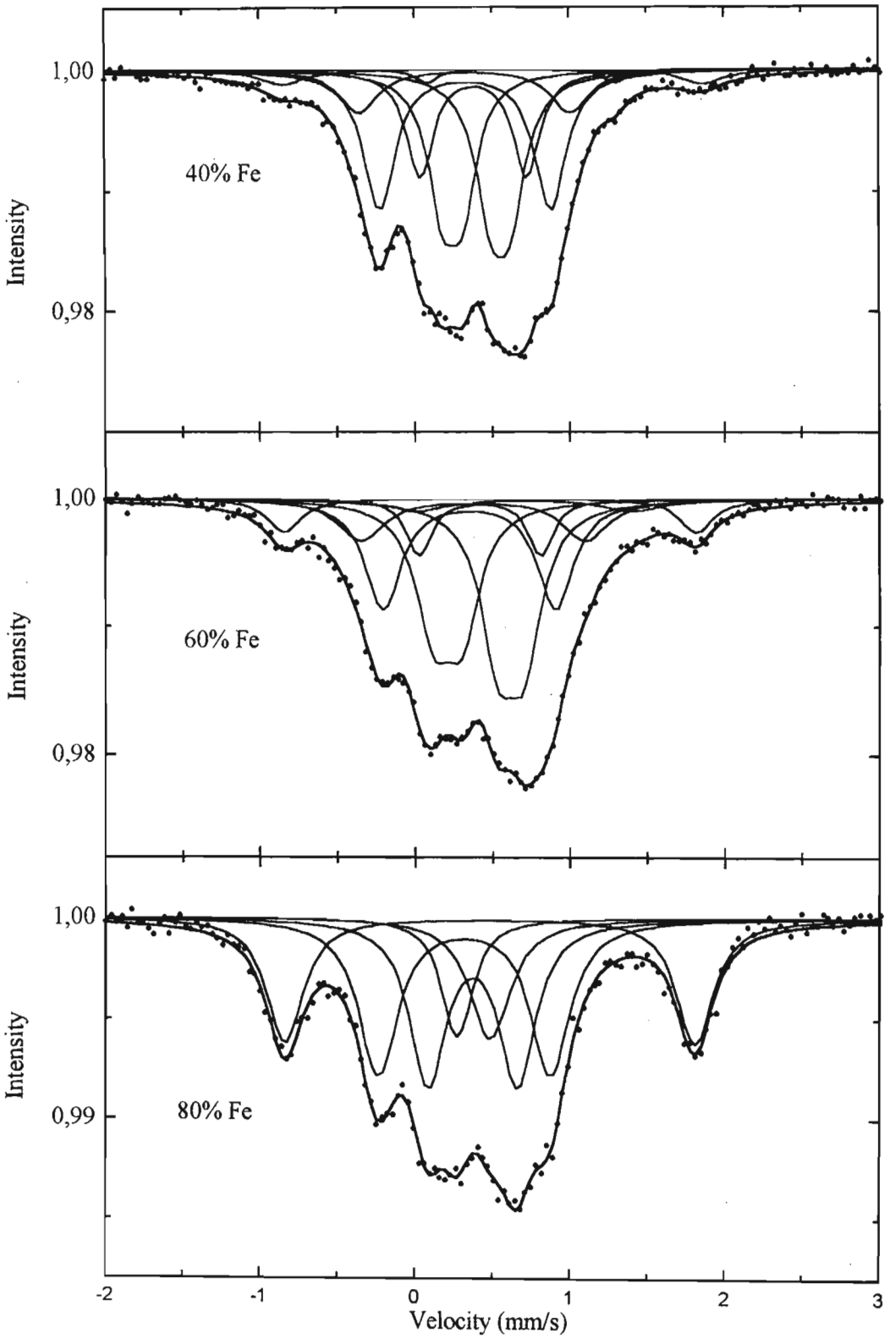

Fig. 3.5(c). Mössbauer spectra of samples with 40%, 60% and 80% Fe concentration

Table 3.2 (a). Isomer shifts (mm/s) of the seven components observed in the samples with varying Fe concentration.

Fe	Component						
conc	*a*	*b*	*c*	*d*	*e*	*f*	*g**
5%	0,41(3)	0,38(4)	0,65(6)	0,36(4)	0,67(4)	0,19(4)	-
10%	0,42(3)	0,38(3)	0,64(6)	0,35(4)	0,59(6)	0,25(6)	-
15%	0,40(3)	0,38(3)	- -	0,34(4)	0,64(5)	0,17(5)	0,48(5)
25%	0,42(3)	0,39(3)	0,71(6)	0,37(5)	0,66(6)	0,19(6)	0,47(4)
30%	0,41(3)	0,37(3)	0,55(6)	0,34(5)	0,64(6)	0,19(6)	0,57(6)
35%	0,38(4)	0,32(3)	0,69(6)	0,32(6)	0,55(6)	0,21(6)	0,47(5)
40%	0,38(5)	0,32(3)	0,69(9)	0,32(5)	0,55(6)	0,24(6)	0,50(5)
60%	0,41(5)	0,35(4)	0,70(6)	0,37(4)	0,61(4)	0,21(4)	0,48(3)
80%	0,37(5)	0,32(4)	- -	- -	0,48(5)	0,27(5)	0,48(4)
average	0,40(2)	0,36(3)	0,66(6)	0,35(2)	0,60(6)	0,21(3)	0,49(4)

Table 3.2 (b) Quadrupole splittings (mm/s) of the seven components observed in the samples with varying Fe concentration. Component g* is due to Fe_2O_3 and the splitting is the magnetic splitting of the two innermost components.

Fe	Component						
conc	*a*	*b*	*c*	*d*	*e*	*f*	*g**
5%	0,72(5)	1,07(6)	1,30(8)	1,46(6)	0,13(6)	0,11(6)	- -
10%	0,72(5)	1,06(5)	1,38(8)	1,48(6)	0,14(7)	0,13(7)	- -
15%	0,74(5)	1,05(5)	- -	1,49(6)	0,10(7)	0,12(7)	2,64(8)
25%	0,74(5)	1,05(5)	1,40(8)	1,42(7)	0,11(8)	0,13(8)	2,56(6)
30%	0,72(5)	1,04(5)	1,29(8)	1,43(7)	0,10(8)	0,17(8)	2,43(8)
35%	0,70(6)	1,07(5)	1,34(8)	1,45(8)	0,14(8)	0,14(8)	2,45(7)
40%	0,68(7)	1,10(5)	1,2(2)	1,36(7)	0,12(8)	0,13(8)	2,70(7)
60%	0,78(7)	1,11(6)	1,39(8)	1,44(6)	0,17(8)	0,18(8)	2,65(6)
80%	0,57(7)	1,10(6)	- -	- -	- -	- -	2,64(5)
average	0,71(6)	1,07(3)	1,33(7)	1,44(4)	0,13(2)	0,14(2)	2,6(1)

Table 3.2 (c). Fractional contribution of the five Fe-V_2O_5 components observed as a function of the Fe concentration.

Fe	Component				
conc.	*a*	*b*	*c*	*d*	*f*
5%	31(5)	36(5)	2(1)	17(4)	14(3)
10%	35(5)	29(5)	6(2)	13(3)	18(4)
15%	40(6)	32(5)	- -	15(3)	14(3)
25%	41(5)	32(5)	6(2)	12(3)	10(3)
30%	38(5)	33(5)	4(2)	12(3)	13(3)
35%	25(4)	37(5)	3(1)	9(2)	26(4)
40%	23(4)	34(5)	3(1)	13(3)	27(4)
60%	12(3)	33(4)	7(2)	15(3)	34(4)

Table 3.2(d) Linewidths (half widths in mm/s) of the seven components observed in the samples with varying iron concentration.

Fe	Component						
conc.	*a*	*b*	*c*	*d*	*e*	*f*	*g**
5%	0,12(3)	0,13(4)	0,09(6)	0,14(4)	0,13(4)	0,12(4)	- -
10%	0,10(3)	0,12(3)	0,09(6)	0,12(4)	0,11(6)	0,11(6)	- -
15%	0,12(3)	0,13(3)	- -	0,17(4)	0,14(4)	0,15(4)	0,09(5)
25%	0,11(3)	0,14(3)	0,14(6)	0,13(5)	0,13(5)	0,12(5)	0,11(4)
30%	0,11(3)	0,13(3)	0,16(6)	0,14(5)	0,13(5)	0,15(5)	0,12(6)
35%	0,10(4)	0,11(3)	0,12(5)	0,12(5)	0,11(6)	0,11(6)	0,12(5)
40%	0,10(5)	0,12(3)	0,09(8)	0,15(5)	0,12(5)	0,11(5)	0,17(5)
60%	0,10(5)	0,14(4)	0,23(6)	0,18(4)	0,13(4)	0,13(4)	0,13(3)
80%	0,13(5)	0,15(4)	- -	- -	0,15(5)	0,11(5)	0,14(3)

Table 3.2 (e). Intensity contributions as a fraction of component *b* of the seven components observed in the samples with varying iron concentration.

Fe	Component						
conc	*a*	*b*	*c*	*d*	*e*	*f*	*g**
5%	87	100	7	47	53	40	- -
10%	122	100	22	43	87	61	- -
15%	123	100	- -	46	58	42	15
25%	127	100	18	36	82	32	59
30%	115	100	11	35	54	38	31
35%	68	100	8	24	80	72	48
40%	67	100	8	38	83	79	42
60%	37	100	21	47	126	105	89
80%	95	100	- -	- -	40	30	235

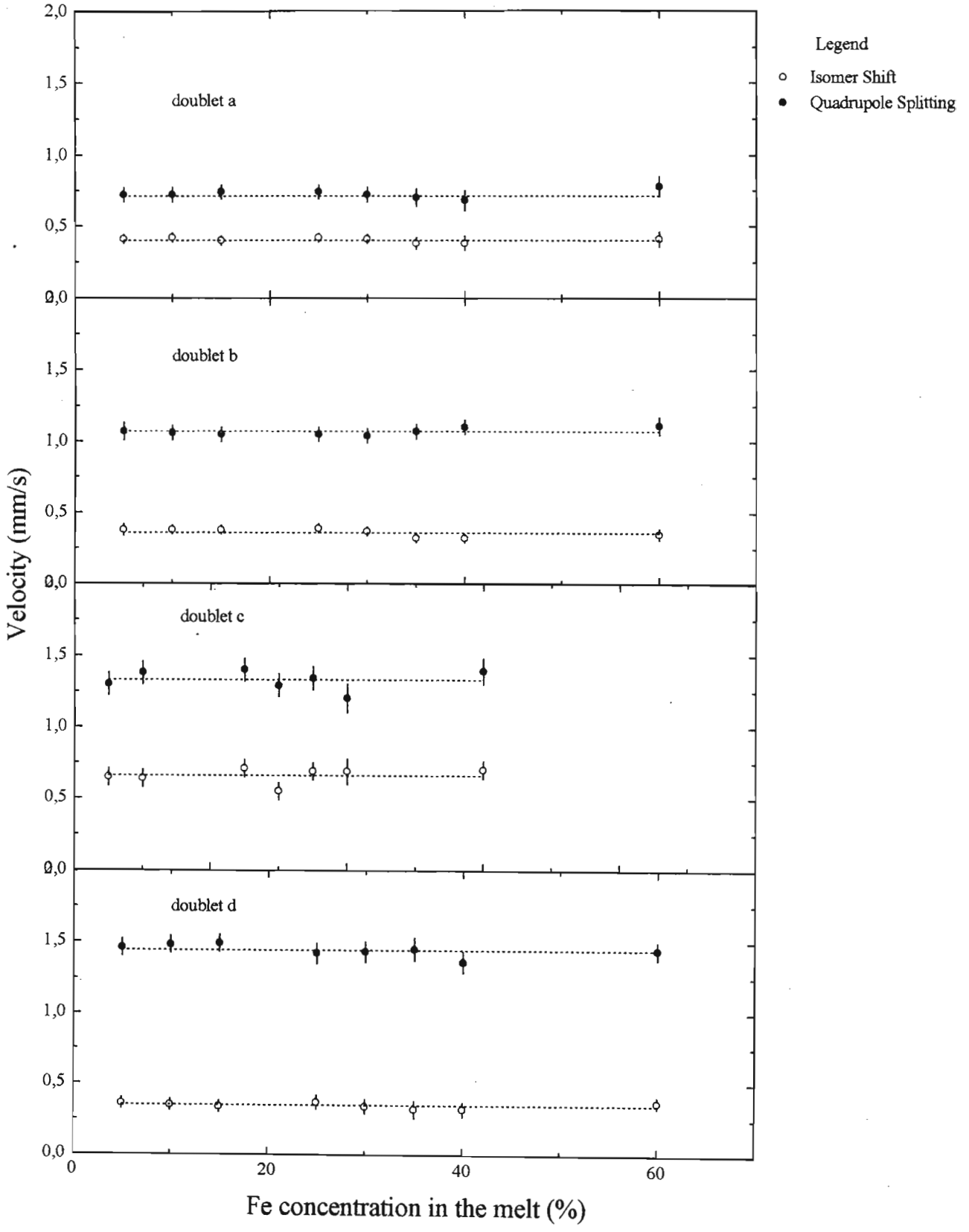

Fig. 3.6(a). Isomer shift and quadrupole splitting of components a to d as a function of Fe concentration

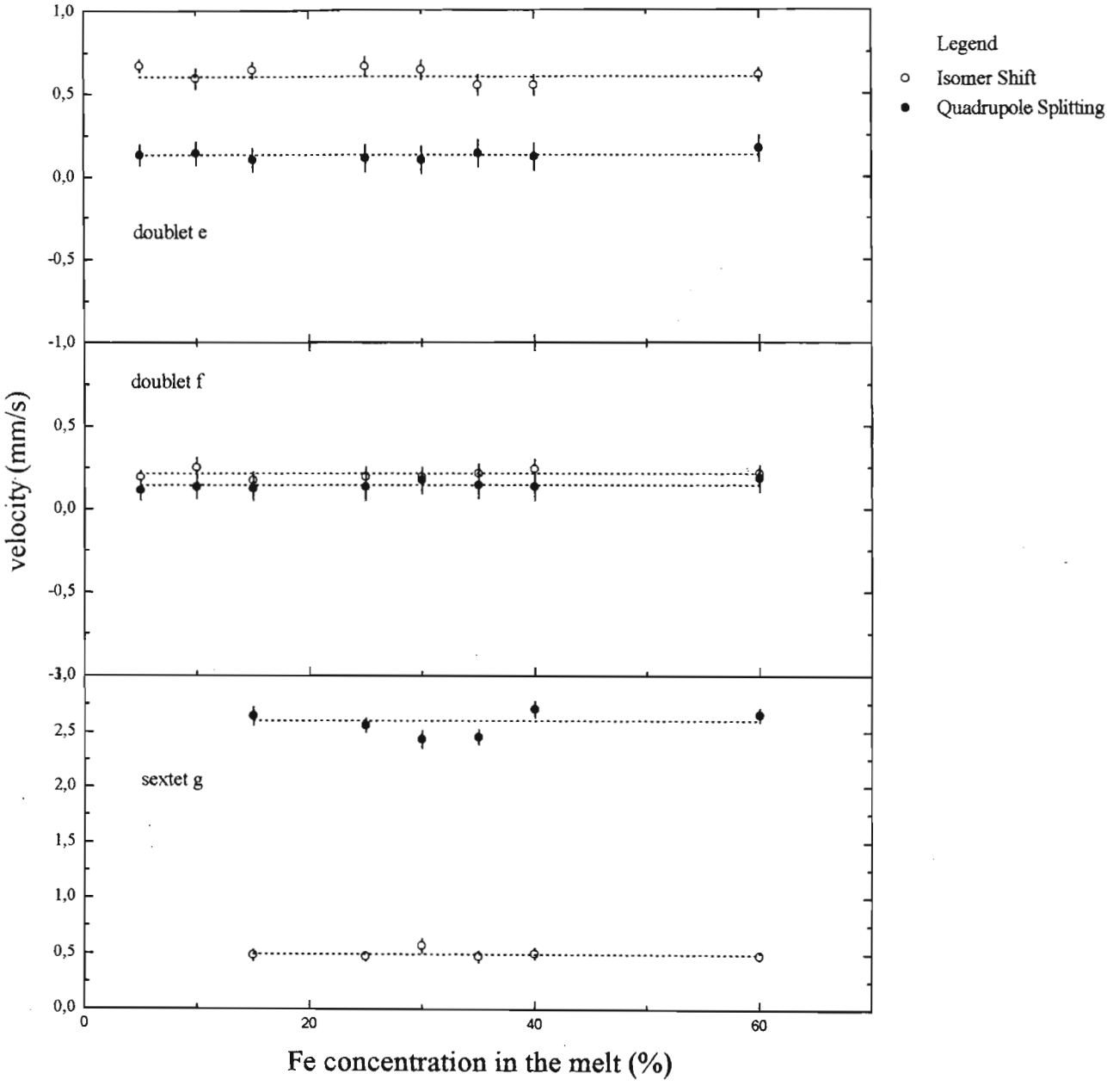

Fig. 3.6(b). Isomer shift and quadrupole splitting of components e, f and g as a function of Fe concentration

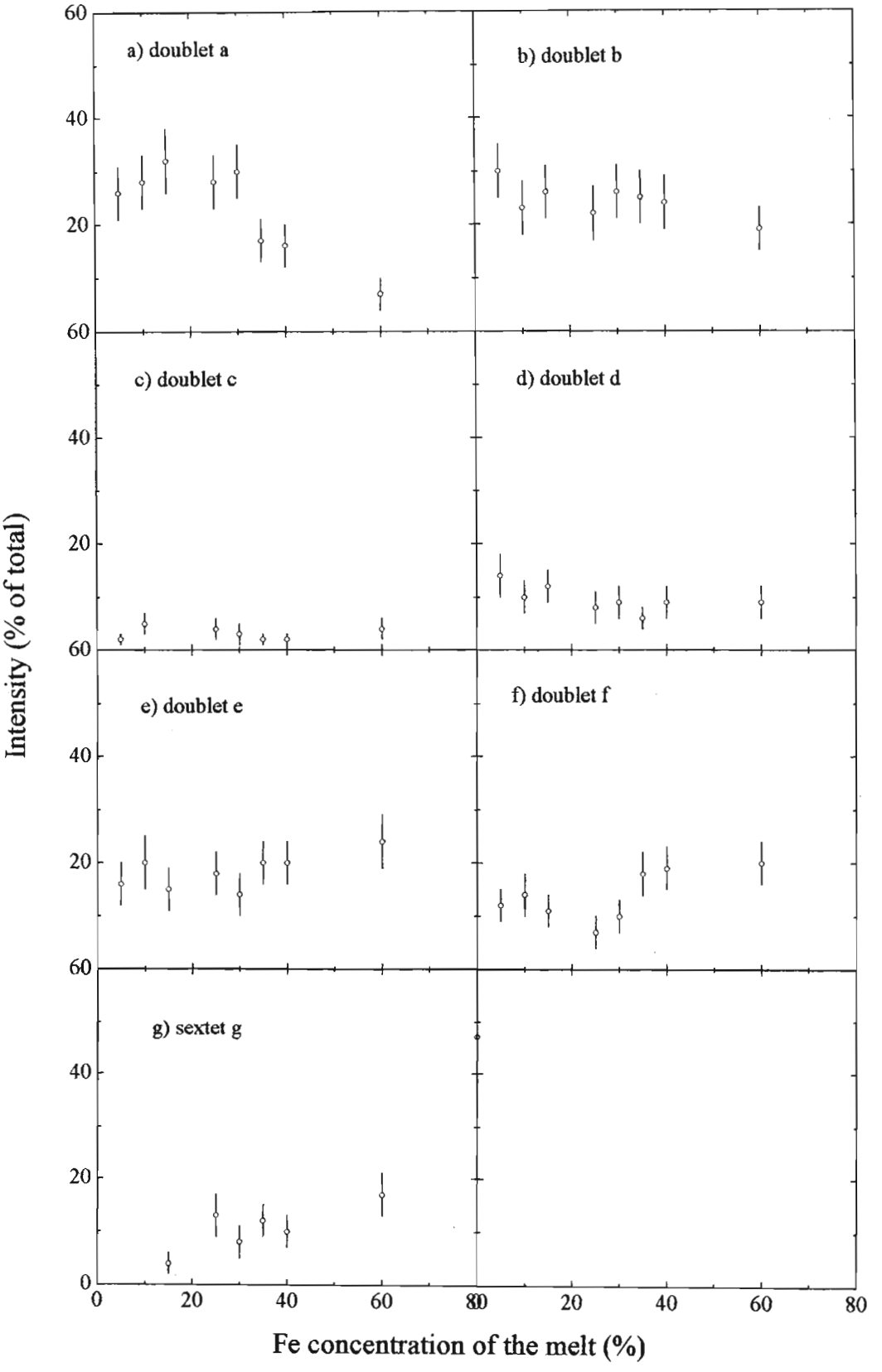

Fig. 3.7. Intensities of the various components as a function of the fit

3.2.4. Temperature dependent Mössbauer Measurements

The third series of Mössbauer results were those which involved temperature dependent measurements. These measurements were performed only on the annealed samples, namely, those with 5%, 15% and 80% Fe concentrations.

The spectra, displayed in Figs. 3.8 (a), (b) and (c), show that the fractional contribution of some of the components do change with sample temperature. In the analysis, each spectrum was again resolved in terms of six doublets and a sextet due the various sites in the Fe-V_2O_5 system and the two Fe_2O_3 components.

In fitting these spectra the following steps were employed.

1. The intensity of c was kept fixed at 3%, the mean value determined from the spectra displayed in Figs. 3.4 and 3.5.
2. The intensity of the left and right components of the remaining doublets were taken as equal, although it was accepted that they could show an asymmetry with temperature.

The parameters resulting from the fit are listed in Table 3.3 (a), (b) and (c) and are illustrated in Figs. 3.9 (a) and (b).

From the Fig. 3.9a we note that the isomer shifts for the doublets display only the characteristic linear dependence due to the second order Doppler shift given in Eqn. 2.13, there is no gradual or sudden appearance of components in comparison with the room temperature measurements.

The quadrupole splittings of the doublets a, b, d, e and f remain constant with increasing temperature for all the concentrations studied, as shown in Fig. 3.9(b). However the magnetic splitting of component g* shows a decrease with increasing temperature.

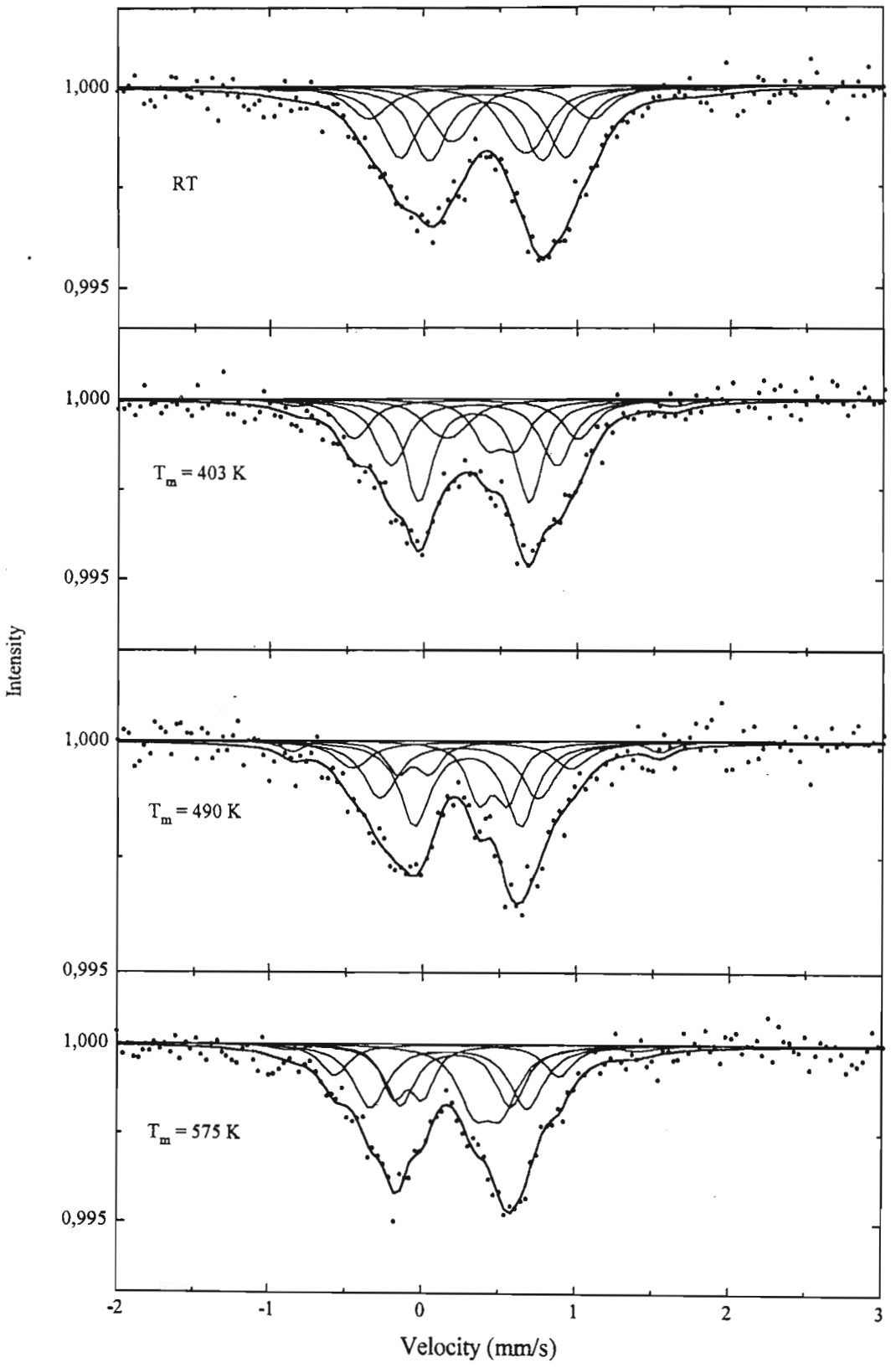

Fig. 3.8(a). Temperature dependent Mössbauer spectra of samples with 5% Fe.

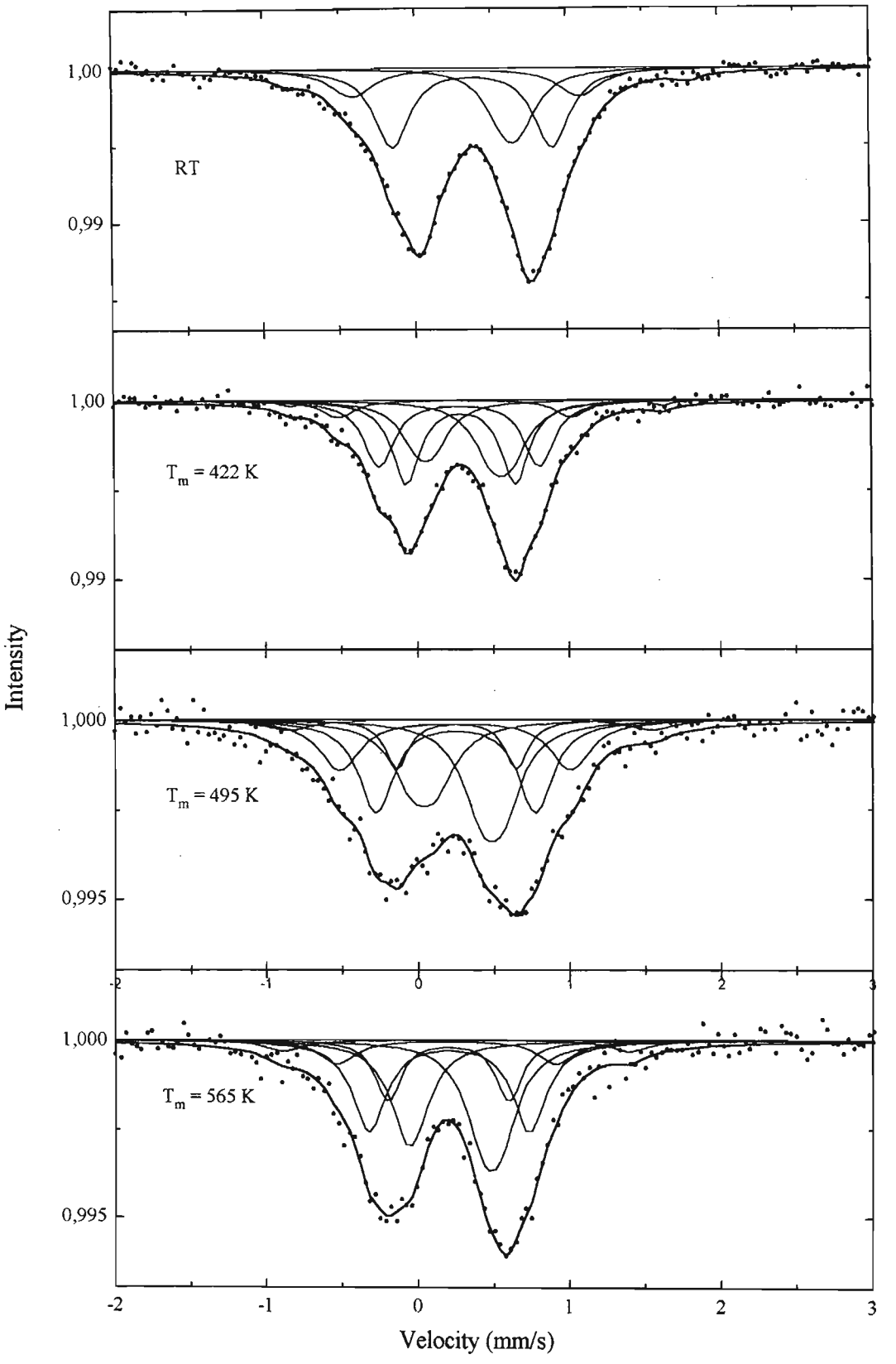

Fig. 3.8(b). Temperature dependent Mössbauer spectra of samples with 15% Fe.

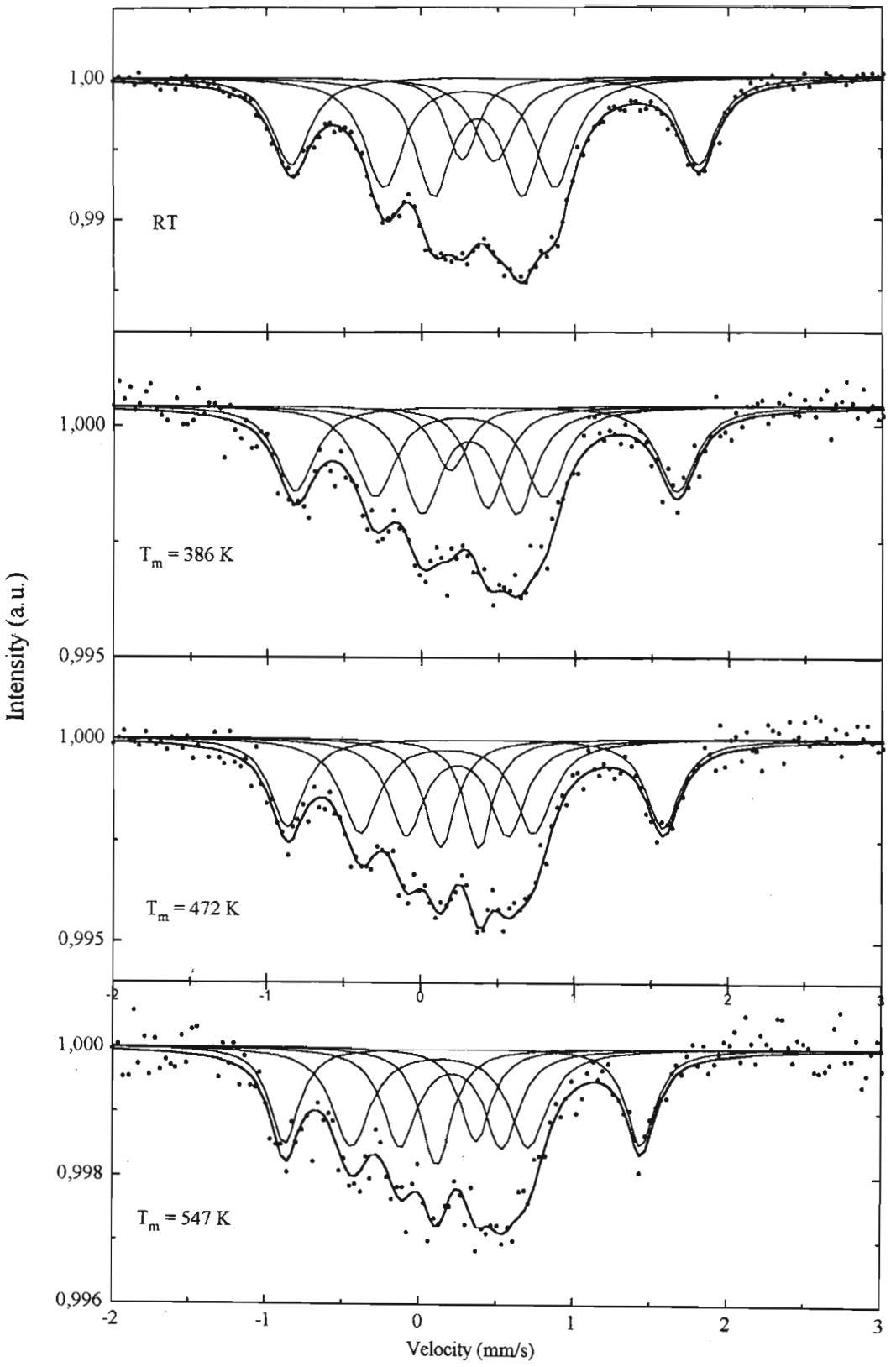

Fig. 3.8(c). Temperature dependent Mössbauer spectra of samples with 80% Fe.

Table 3.3(a). Isomer shift (δ), quadrupole splitting (ΔE_Q), linewidth (Γ/2) and line intensity (I) of the different components in the Mössbauer spectra of the sample with 5% Fe molar concentration at various temperatures

	300 K				403 K			
Component	δ (mm/s)	ΔE_Q (mm/s)	I (%)	Γ/2 (mm/s)	δ (mm/s)	ΔE_Q (mm/s)	I (%)	Γ/2 (mm/s)
a	.41(3)	0.73(5)	23(4)	.13(4)	.33(3)	.72(5)	29(4)	.10(4)
b	.39(3)	1.07(8)	24(4)	.13(4)	.33(3)	1.07(8)	22(4)	.12(4)
d	.37(4)	1.45(6)	12(5)	.14(4)	.28(4)	1.45(6)	13(5)	.12(4)
e	.67(4)	.12(6)	14(6)	.13(4)	.51(4)	.18(6)	12(6)	.10(4)
f	.19(4)	.11(6)	10(6)	.12(4)	.15(4)	.12(6)	9(6)	.13(4)
g*	.48(6)	2.64(6)	17(5)	.26(6)	.41(6)	2.45(6)	15(5)	.13(6)

	490 K				573 K			
Component	δ (mm/s)	ΔE_Q (mm/s)	I (%)	Γ/2 (mm/s)	δ (mm/s)	ΔE_Q (mm/s)	I (%)	Γ/2 (mm/s)
a	.29(5)	.69(5)	28(8)	.12(5)	.22(5)	.72(5)	20(8)	.11(5)
b	.24(4)	1.3(9)	22(6)	.13(5)	.18(4)	1.01(9)	23(6)	.13(5)
d	.25(5)	1.2(7)	11(7)	.14(5)	.16(5)	1.46(7)	10(7)	.11(5)
e	.46(5)	.19(5)	14(8)	.09(5)	.43(5)	.18(5)	18(5)	.12(5)
f	-.06(4)	.20(6)	8(6)	.09(5)	-.09(4)	.19(6)	12(6)	.09(5)
g*	.35(7)	2.38(7)	17(7)	.09(7)	.26(7)	2.27(7)	15(7)	.15(7)

Table 3.3(b). Isomer shift (δ), quadrupole splitting (ΔE_Q), linewidth (Γ/2) and line intensity (I) of the different components in the Mössbauer spectra of the sample with 15% Fe molar concentration at various temperatures

	300 K				422 K			
Component	δ (mm/s)	ΔE_Q (mm/s)	I (%)	Γ/2 (mm/s)	δ (mm/s)	ΔE_Q (mm/s)	I (%)	Γ/2 (mm/s)
a	.40(3)	.74(5)	31(3)	.12(3)	.29(3)	.72(5)	27(3)	.11(3)
b	.38(3)	1.05(8)	25(3)	.13(3)	.28(3)	1.05(8)	24(3)	.12(3)
d	.34(4)	1.49(6)	11(4)	.17(4)	.25(4)	1.53(6)	7(4)	.13(4)
e	.64(4)	.10(6)	14(4)	.14(4)	.55(4)	.12(6)	19(4)	.15(4)
f	.17(4)	.12(6)	11(4)	.15(4)	.06(4)	.10(6)	14(4)	.14(4)
g*	.48(6)	2.64(6)	8(5)	.09(6)	.39(6)	2.45(6)	9(5)	.09(6)

	495 K				565 K			
Component	δ (mm/s)	ΔE_Q (mm/s)	I (%)	Γ/2 (mm/s)	δ (mm/s)	ΔE_Q (mm/s)	I (%)	Γ/2 (mm/s)
a	.26(4)	.78(6)	8(4)	.09(4)	.20(4)	.79(6)	12(4)	.10(4)
b	.25(4)	1.05(9)	22(4)	.14(4)	.20(4)	1.05(9)	24(4)	.13(4)
d	.25(5)	1.52(7)	14(5)	.16(5)	.19(5)	1.44(7)	7(5)	.15(5)
e	.49(5)	.14(7)	19(5)	.15(5)	.48(5)	.11(7)	22(5)	.14(5)
f	.04(5)	.15(7)	15(5)	.16(5)	-.05(5)	.04(7)	15(5)	.14(5)
g*	.35(7)	2.38(7)	20(6)	.18(7)	.25(7)	2.27(7)	20(6)	.15(7)

Table 3.3(c). Isomer shift (δ), quadrupole splitting (ΔE_Q), linewidth (Γ/2) and line intensity (I) of the different components in the Mössbauer spectra of the sample with 80% Fe molar concentration at various temperatures

	300 K				386 K			
Component	δ (mm/s)	ΔE_Q (mm/s)	I (%)	Γ/2 (mm/s)	δ (mm/s)	ΔE_Q (mm/s)	I (%)	Γ/2 (mm/s)
a	.37(5)	.57(7)	13(4)	.13(4)	.31(6)	.61(7)	13(5)	.14(6)
b	.32(4)	1.10(6)	14(4)	.15(4)	.25(5)	1.09(6)	12(5)	.14(5)
e	.48(5)	- -	6(6)	.15(5)	.43(6)	- -	6(7)	.13(6)
f	.27(5)	- -	6(4)	.11(5)	.19(6)	- -	4(7)	.12(6)
g*	.48(3)	2.64(5)	63(3)	.14(3)	.42(3)	2.47(5)	65(3)	.14(3)

	472 K				547 K			
Component	δ (mm/s)	ΔE_Q (mm/s)	I (%)	Γ/2 (mm/s)	δ (mm/s)	ΔE_Q (mm/s)	I (%)	Γ/2 (mm/s)
a	.24(7)	.66(9)	12(6)	.14(7)	.21(7)	.66(9)	12(6)	.13(7)
b	.17(6)	1.12(8)	13(6)	.15(6)	.13(6)	1.15(8)	14(6)	.15(6)
e	.38(7)	- -	5(8)	.11(7)	.37(7)	- -	5(8)	.12(7)
f	.13(7)	- -	6(8)	.12(7)	.11(7)	- -	7(8)	.12(7)
g*	.36(3)	2.44(5)	64(3)	.13(3)	.28(3)	2.31(5)	62(3)	.11(3)

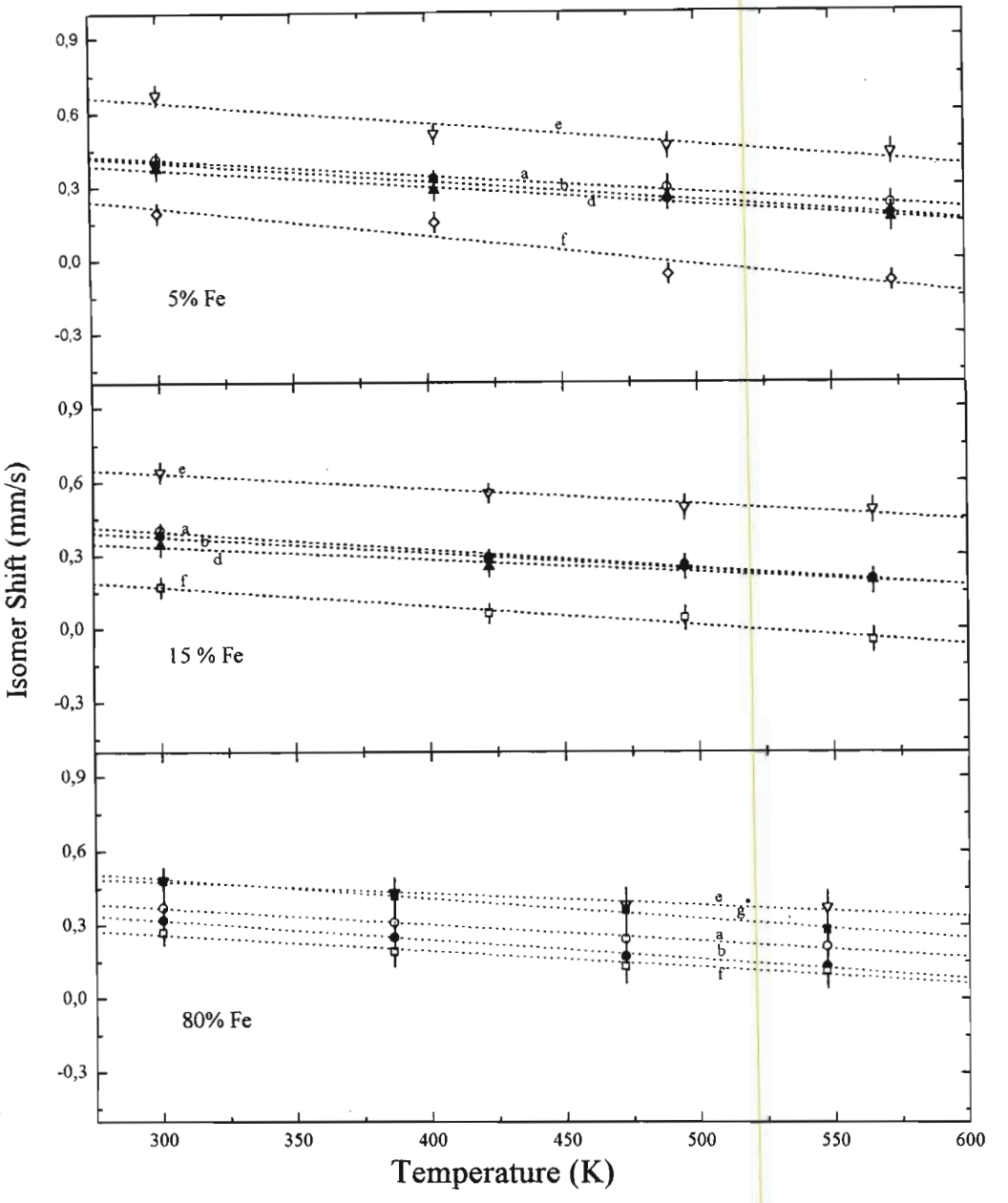

Fig. 3.9(a). Isomer shifts of components a, b, d, e, f and g, observed in spectra of 5%, 15% and 80% Fe concentration samples, as a function of sample temperature

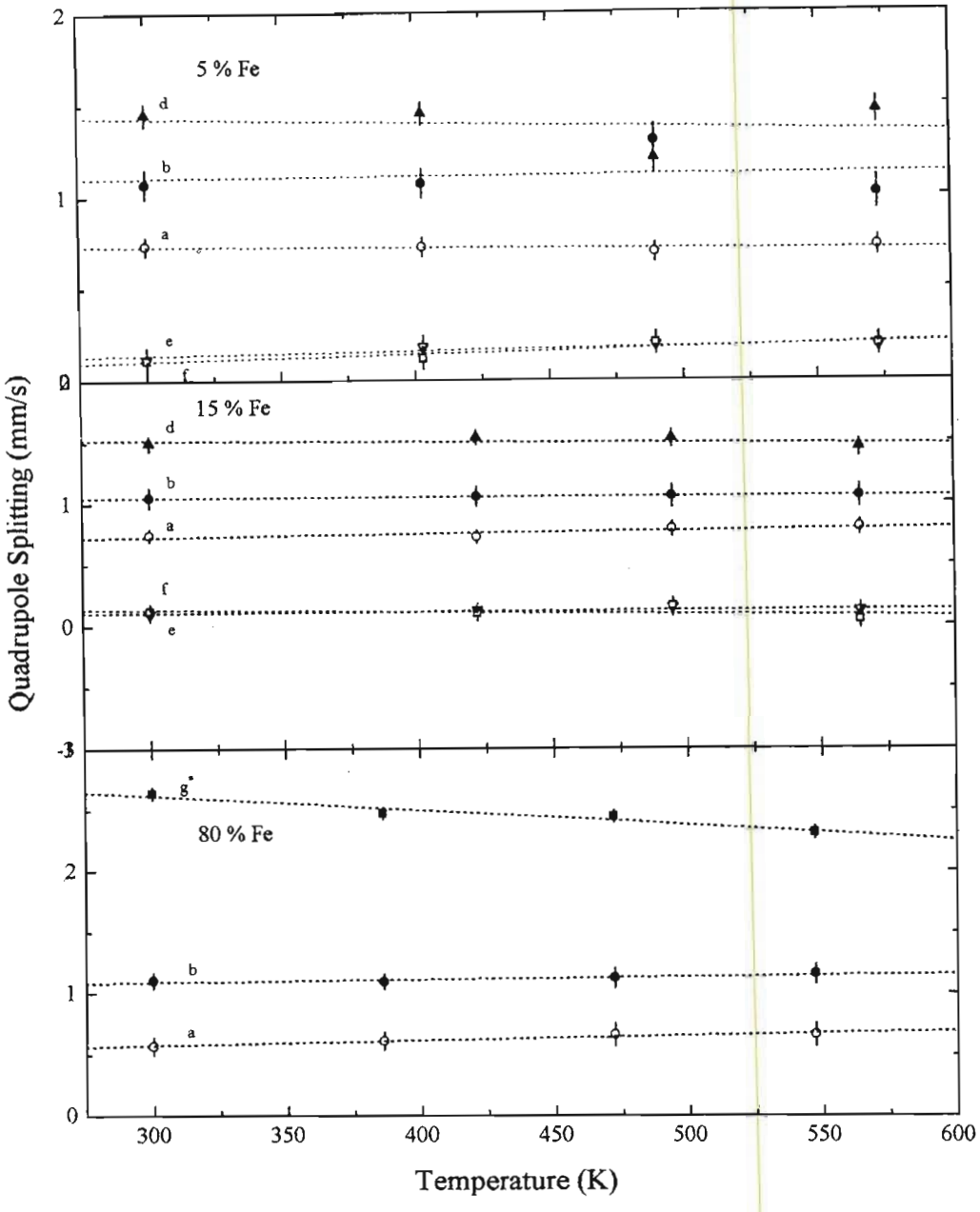

Fig. 3.9(b). Quadrupole splittings of components a, b, d, e, f and g, observed in spectra of 5%, 15% and 80% Fe concentration samples, as a function of sample temperature

3.2.5. The x-ray diffraction data on the Fe-V_2O_5 samples.

The x-ray diffraction data collected on all the powders created are shown in Fig. 3.10 (a), (b), (c) and (d). The positions and intensities of the peaks were determined by fitting Lorenzian line shapes to the spectra and the results are listed in Table 3.4(a), (b), (c), (d) and (e), where they are listed in terms of the structure that they represent.

In order to determine the phases present in the spectra, it was assumed that the three main phases, orthorhombic V_2O_5, monoclinic VOB and tetragonal Fe_2O_3, were present in the spectra. Approximate 2θ positions for each of these phases were calculated from the lattice parameters of Borisenko et al., [BOR70], Galy et al., [GAL67] and Brown [BRO86] respectively.

Comparing these starting 2θ positions with those present in the spectra, it was observed that there were peaks in the spectra which could be assigned exclusively to one of these three phases. These peaks are listed in Table 3.5(a), (b) and (c) and were set as the list of observables for the least squares procedures, which were developed to determine the lattice parameters of each phase. However, it must be noted that they were represented as the reciprocal lattice plane spacings

$$D(h,k,l) = \left(\frac{1}{d(h,k,l)}\right)^2$$

rather than 2θ values. This conversion was calculated from Bragg's Law

$$2\,d\,\sin(\theta) = \lambda.$$

The equations used to model the observables with the theoretical values were:

(i) for the orthorhombic case:

$$D(h,k,l) = Ah^2 + Bk^2 + Cl^2$$

(ii) for the tetragonal case:

$$D(h,k,l) = A\left(h^2 + k^2\right) + Cl^2$$

(iii) for the monoclinic case:

$$D(h,k,l) = \frac{\left(\frac{h}{c}\right)^2 + \left(\frac{l}{c}\right)^2 - 2\left(\frac{hl}{ac}\right)\cos\beta}{\sin^2\beta} + \left(\frac{k}{b}\right)^2$$

In these equations, *h,k and l* are the Miller indices of the lattice planes and *a, b, c* and β are the lattice constants, with

$$A = \frac{1}{a^2},\ B = \frac{1}{b^2} \text{ and } C = \frac{1}{c^2}$$

In the least squares procedure the variables were *h, k* and *l* and the constants that were optimised were the lattice constants *a, b, c* and β.

For the orthorhombic and tetragonal cases, linear least squares routines could be used, whereas for the monoclinic case, a non-linear least squares routine had to be used. In this latter case, the starting values for the lattice constants were taken from Galy et al. [GAL67].

The entire program used for the monoclinic case is listed in appendix C, together with the alternate subroutines needed for the tetragonal and orthorhombic phases.

The lattice parameters obtained for all the three phases are listed in Table 3.6(a), (b) and (c) in terms of the Fe concentration. From these optimised lattice parameters, the complete list of peak positions for each phase were then generated, after which individual peaks in the spectra were identified as belonging to any one of these phases. At this stage of the analysis it was possible that any one observed peak could be assigned to two or more expected (*hkl*) reflections, but this was no longer critical in terms of evaluating the structure. The remaining observed peaks which did not belong to any of these three phases were then attributed to an unknown phase.

The complete list of all the assignments are shown in Table 3.4(a), (b), (c) and (d).
Table 3.4(e) lists those observed peaks which could not be assigned to any one of the three main phases. The reflection positions of these peaks have the same value for all the Fe concentrations, and we can therefore attribute them to a single unknown phase, the structure of which is not yet determined.

To compare the contributions from the different phases as a function of the Fe concentration in the samples, the strongest lines from each phase was used, i.e. (001) in V_2O_5, (003) in θ-VOB and (0012) and (205) in Fe_2O_3.

Fig. 3.11 shows the ratio of the intensity of each of the above lines to the total intensity of all the lines in each spectrum. From these figures, the following trends in the concentrations of the various phases are observed.

1. The V_2O_5 is dominant at 5% Fe concentration but decreases in contribution as the Fe concentration increases to 25%. At 30% Fe concentration, it becomes dominant again and once more decreases in contribution as the Fe concentration increases.
2. The θ-VOB phase increases in contribution as the Fe concentration increases from 5% to 25%, at which concentration it is at a maximum, and also the dominant phase. Beyond this concentration, its contribution is again low, and remains low and constant as the Fe concentration increases to 80%.
3. The Fe_2O_3 phase is weak in contribution up to 25% Fe concentration, after which its contribution gradually increases. It does not show any dominance at any Fe concentration.
4. The unknown phase is very weak at 5% and 10% Fe concentration. From 15% Fe concentration onwards, its contribution increases gradually.
5. From 30 % Fe concentration and onwards, the three phases θ-VOB, Fe_2O_3 and the unknown phase have equal contributions within the limits of the experimental accuracy.

The V_2O_5 phase can also be considered as having equal contributions in terms of the other phases in this region, with the exception of the 30% and 40% Fe concentration, where this V_2O_5 phase is dominant.

Further to these points, it is also worthwhile to compare the intensities of the V_2O_5 2Θ lines in terms of

(i) the ratio of lines which correspond to the same crystallographic direction

(ii) the ratio of lines which correspond to different crystallographic directions.

Fig. 3.12(a) and Fig. 3.12(b) illustrates the ratio between lines in the <001> and <200> crystallographic directions respectively. Fig. 3.12(c) illustrates the ratio between lines from the <001> direction with lines from the <200> direction. In these figures, the dotted line indicates the expected ratio [BOR70]. From these figures, the ratios of reflection intensities of lattice planes in the same directions are as expected, but the ratio of intensities of lattice planes from different crystallographic directions are not the same.

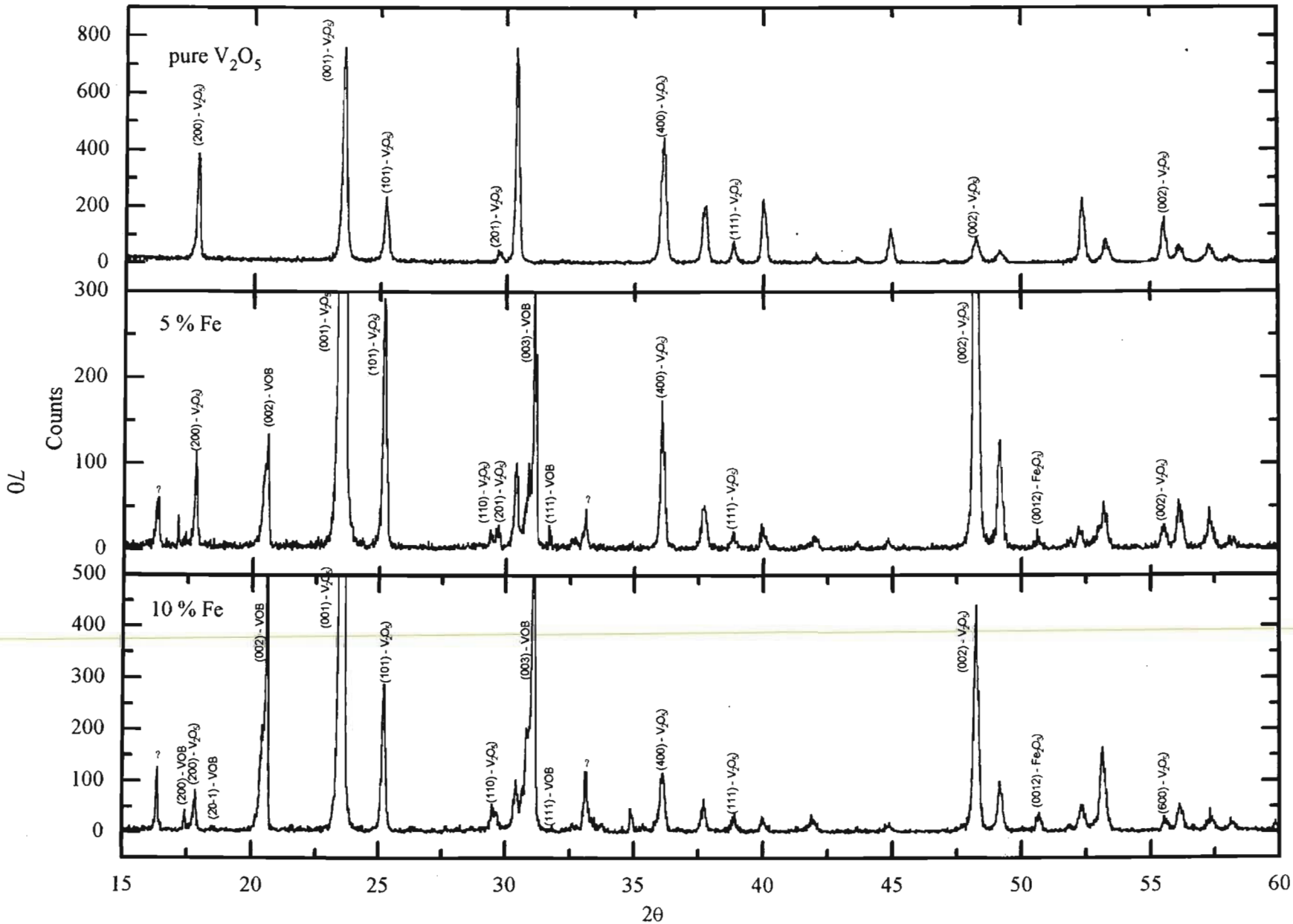

Fig. 3.10(a). X-ray spectra of V_2O_5 with various concentrations of Fe.

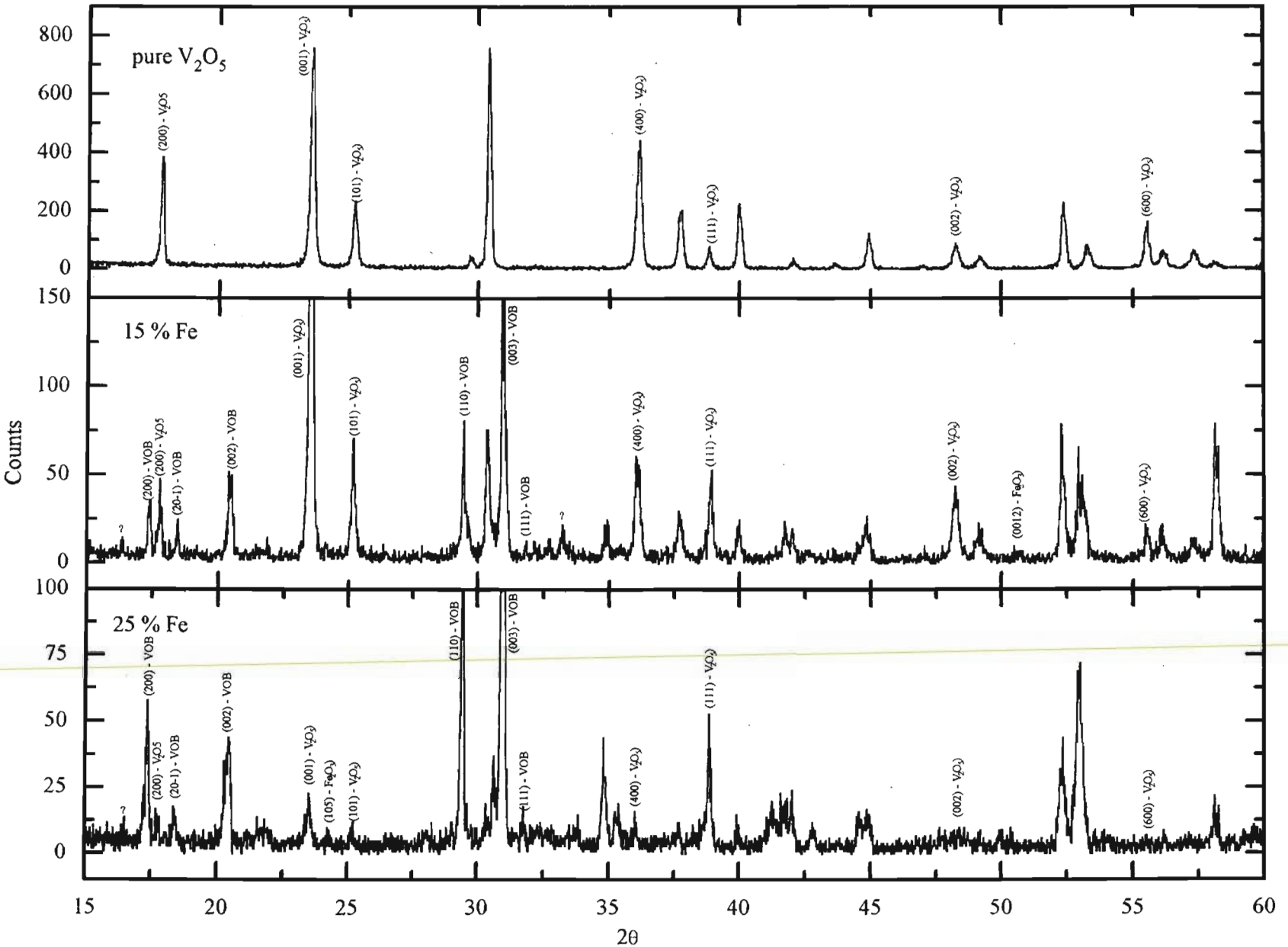

Fig. 3.10(b). X-ray spectra of V_2O_5 with various concentrations of Fe.

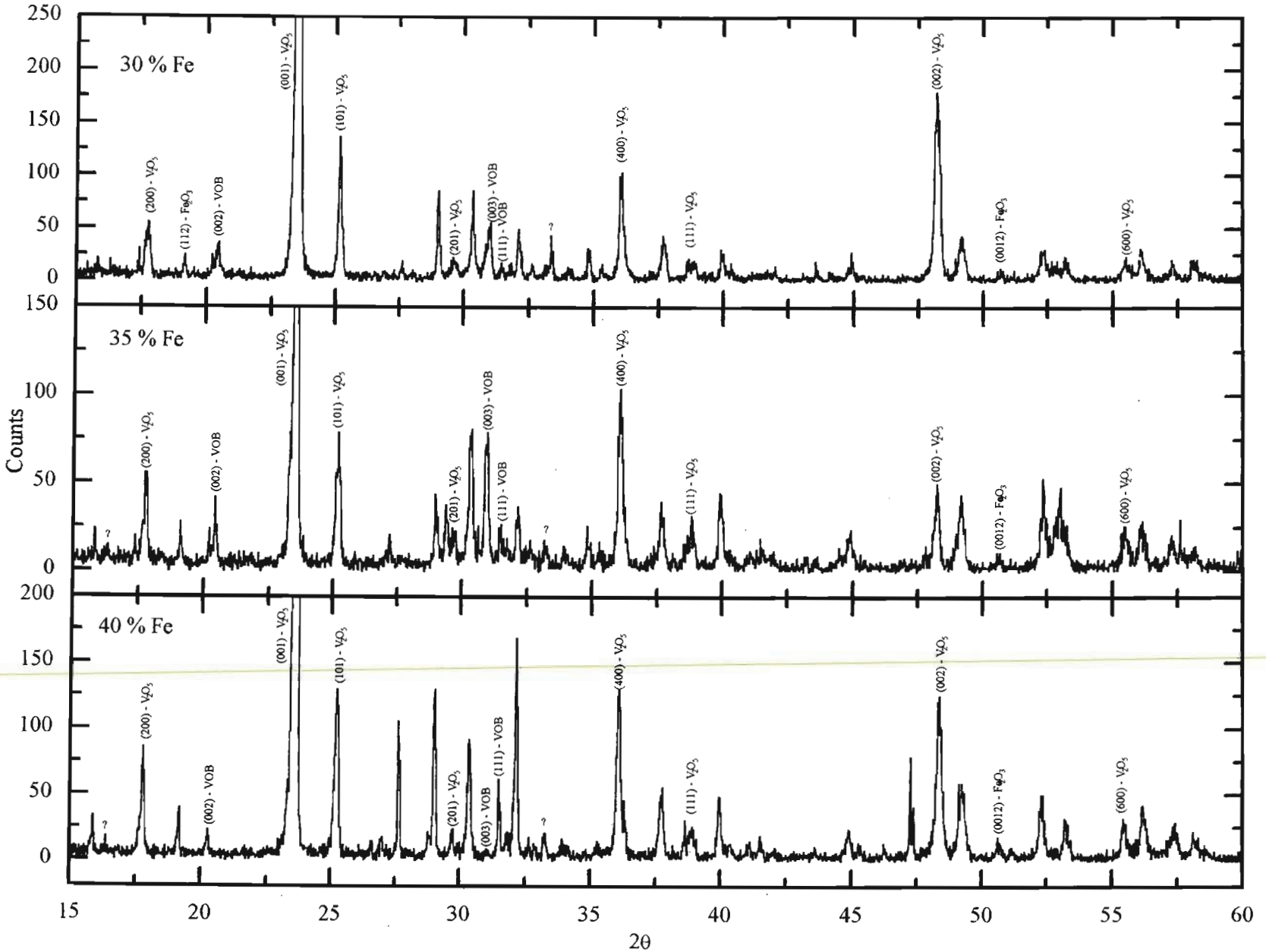

Fig. 3.10(c). X-ray spectra of V_2O_5 with various concentrations of Fe.

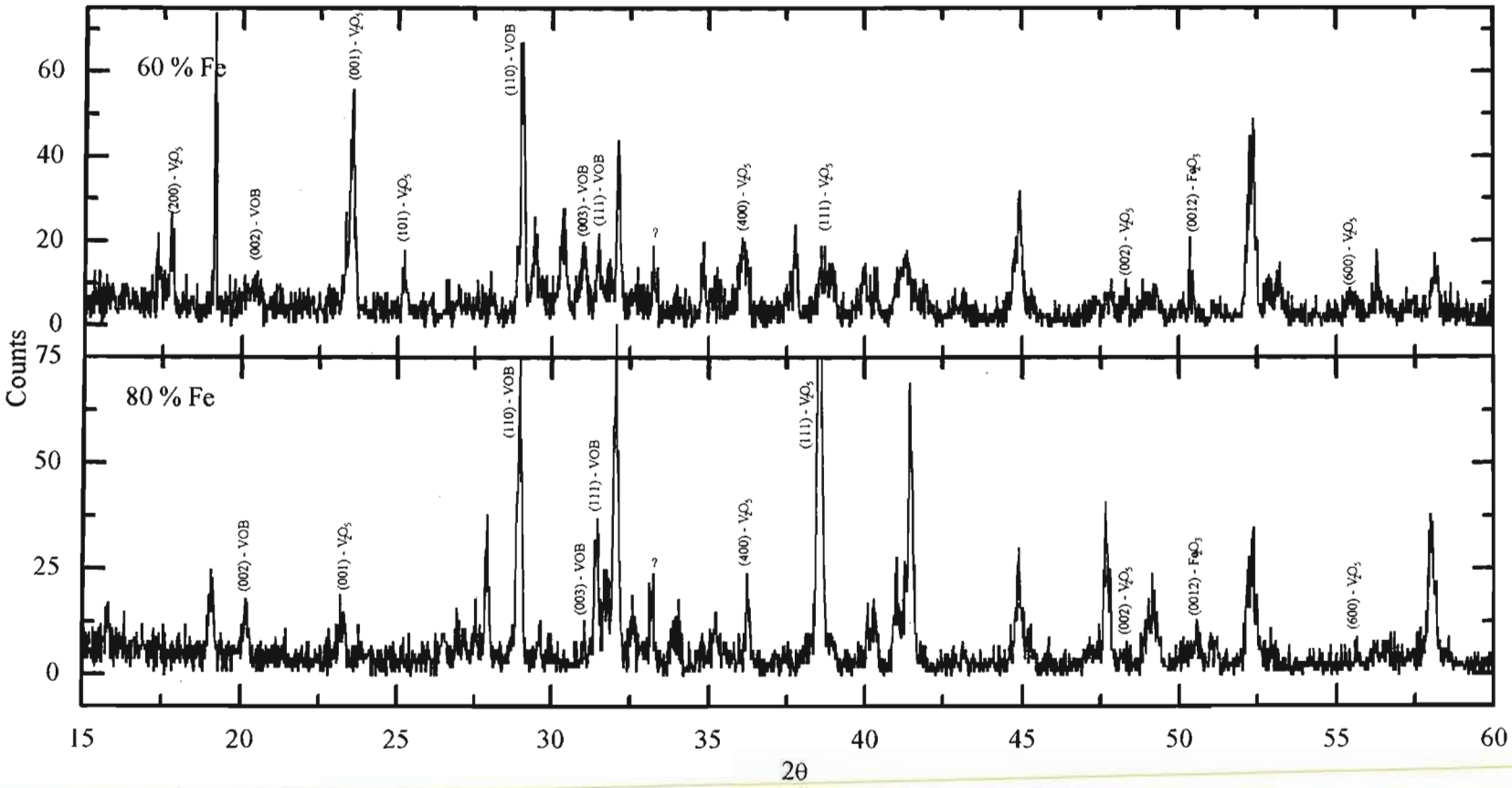

Fig. 3.10(d). X-ray spectra of V_2O_5 with various concentrations of Fe.

Table 3.4(a) 2θ positions for V_2O_5 phase of all concentrations

	Fe concentration								
hkl	5%	10%	15%	25%	30%	35%	40%	60%	80%
200	17,75 15	17,78 13	17,75 8	17,71 1	17,71 14	17,73 12	17,75 14	17,73 2	--
001	23,50 788	23,52 565	23,49 70	23,46 7	23,49 271	23,48 74	23,57 196	23,50 13	23,21 7
101	25,17 54	25,19 49	25,17 13	25,15 5	25,15 23	25,17 17	25,21 26	25,19 4	--
201	29,67 6	--	29,55 2	--	29,60 3	29,72 6	29,73 2	29,74 3	--
400	36,07 32	36,09 29	36,06 16	35,98 1	36,05 22	36,07 24	36,07 23	36,07 8	36,24 4
310	39,97 7	40,00 8	39,98 6	39,97 4	39,97 7	39,95 11	39,96 10	39,96 2	40,07 1
002	48,23 147	48,24 98	48,23 14	--	48,21 47	48,23 12	48,36 34	48,28 3	48,27 3
102	49,15 31	49,17 25	49,16 8	--	49,14 14	49,15 13	49,22 19	--	49,09 9
202	52,25 5	52,33 10	52,32 16	52,32 11	52,29 10	52,31 11	52,30 13	52,30 13	52,31 11
600	55,50 7	55,54 8	55,50 5	--	55,51 8	55,46 9	55,46 8	55,46 1	55,65 1
302	56,13 16	56,12 11	56,11 7	--	56,12 8	56,12 9	56,18 14	56,31 1	--

Table 3.4(b) 2θ positions for θ-VOB phase of all concentrations

	Fe concentration								
hkl	5%	10%	15%	25%	30%	35%	40%	60%	80%
20-1	--	--	18,41 2	18,36 5	--	18,29 1	--	--	--
002	20,46 31	20,43 103	20,42 12	20,38 13	20,37 11	20,36 9	20,23 4	20,31 8	--
201	--	--	--	21,73 8	--	--	--	--	--
110	29,40 5	29,55 19	29,43 6	29,42 19	29,60 3	29,39 7	--	29,40 5	29,54 1
003	31,10 52	31,05 126	30,94 34	30,96 34	30,93 15	30,92 11	31,00 2	30,97 7	31,05 1
111	31,69 2	--	31,80 1	31,75 3	31,77 2	31,69 11	31,70 2	31,70 4	31,74 8
20-3	32,64 2	32,73 11	32,65 1	32,80 1	32,60 1	32,58 6	--	--	32,62 6
40-3	--	--	42,62 1	42,76 3	--	--	--	--	--

Table 3.4(c) 2θ positions for Fe_2O_3 phase of all concentrations

	Fe concentration								
hkl	5%	10%	15%	25%	30%	35%	40%	60%	80%
112	--	--	--	--	19,142	19,095	19,145	19,117	19,066
105	--	--	--	24,213	--	--	--	--	--
203	--	--	--	28,022	27,592	--	27,6311	--	27,738
205	--	--	32,141	32,323	32,128	32,145	32,1422	--	32,0512
206	--	--	--	35,312	35,313	35,254	35,301	--	35,231
209	--	--	--	--	--	--	45,353	--	--
316	--	--	--	--	--	--	47,329	47,303	--
0012	50,564	50,659	50,623	--	50,643	50,626	50,634	50,404	50,453

Table 3.4d 2θ positions for mixed phases of all concentrations

Phase			Fe concentration								
V_2O_5	Fe_2O_3	VOB	5%	10%	15%	25%	30%	35%	40%	60%	80%
--	103	200	--	17,414	17,356	17,3410	17,365	17,342	--	17,362	--
110	116	--	30,3721	30,4017	30,3717		30,3315	30,3213	30,3616	30,325	--
--	--	40-1 400 11-2	--	34,899	34,907	34,828	34,795	34,804	34,832	34,803	--
011	216	--	37,6814	--	37,698	--	37,6910	37,6410	37,7112	37,716	--
111	--	401	38,835	38,878	38,8911	38,878	38,7411	38,7711	38,7910	38,749	38,5422
211 401	226 119	11-3 004	41,917	41,8912	41,857	41,826	41,972	41,694	41,523	--	41,4513
--	--	113 402	44,843	44,828	44,789	44,727	44,875	44,877	44,876	44,8810	44,884
411	--	005 510	53,1319	53,1345	53,0221	52,9622	52,775	52,9420	--	--	--
012	406	--	57,3212	57,3212	57,316	--	57,287	57,237	57,3210	--	--
112	--	020	58,216	58,197	58,1819	58,096	58,148	58,017	58,2711	58,115	58,0211

Table 3.4(e). 2θ positions for lines of unknown phase

Fe concentration								
5%	10%	15%	25%	30%	35%	40%	60%	80%
--	--	--	--	15,801	15,821	15,846	--	15,761
16,2712	16,3314	16,341	--	--	16,281	16,375	--	--
--	--	--	--	--	--	--	--	20,145
--	--	--	--	--	--	26,551	--	26,451
--	--	--	--	--	--	26,953	--	26,931
--	--	--	--	--	--	--	28,073	--
--	--	--	--	29,0112	29,068	29,0219	29,0111	28,9513
--	--	--	--	31,432	31,462	31,507	31,464	31,386
33,088	33,1324	33,192	--	33,366	33,205	33,254	33,223	33,224
--	33,735	--	33,744	34,032	33,986	33,996	--	33,945
--	--	--	--	--	--	--	40,311	40,274
--	--	--	41,263	--	41,072	41,064	41,3614	41,037
--	--	--	--	--	--	42,054	--	--
--	--	--	--	--	--	--	43,016	--
43,644	--	--	--	43,602	--	--	--	--
--	--	--	--	44,061	44,422	--	--	--
--	--	--	--	--	--	46,232	--	--
--	--	--	--	--	--	--	47,802	47,679
--	--	--	--	--	--	51,152	--	51,083
--	--	--	--	53,226	--	53,238	--	--

Table 3.5(a) 2θ positions for well defined x -ray lines identified with the V_2O_5 phase in Fe-V_2O_5 as a function of Fe molar concentration

hkl	0%	5%	10%	15%	25%	30%	35%	40%	60%	80%
200	17,79	17,76	17,78	17,75	17,71	17,71	17,73	17,75	17,73	--
001	23,53	23,50	23,52	23,49	23,46	23,49	23,48	23,57	23,50	23,21
101	25,20	25,17	25,19	25,17	25,15	25,15	25,17	25,21	25,19	--
201	29,76	29,67	--	--	--	29,61	29,73	29,73	29,74	--
400	36,11	36,07	36,09	36,06	35,98	36,05	36,07	36,07	36,07	36,24
111	38,85	38,83	38,87	38,89	38,87	38,74	38,77	38,87	38,74	38,54
002	48,26	48,23	48,24	48,23	--	48,21	48,23	48,36	48,28	48,27
202	52,20	52,25	52,33	52,32	52,32	52,29	52,31	52,30	52,30	52,31
600	55,52	55,50	55,54	55,50	--	55,51	55,46	55,46	55,46	55,65

Table 3.5(b) 2θ positions for well defined x -ray lines identified with the θ-VOB phase in Fe-V_2O_5 as a function of Fe molar concentration

hkl	0%	5%	10%	15%	25%	30%	35%	40%	60%	80%
200		--	17,41	17,35	17,34	17,36	17,34	--	17,36	--
20-1		--	18,47	18,41	18,36	--	18,29	--	--	--
002		20,46	20,43	20,42	20,38	20,38	20,36	20,23	20,31	20,43
110		29,40	--	29,43	29,42	--	29,39	--	29,41	--
003		31,10	31,05	30,94	30,96	30,93	30,92	31,00	30,97	31,05
111		31,69	31,75	31,80	31,75	31,77	31,69	31,70	31,70	31,74

Table 3.5(c) 2θ positions for well defined x -ray lines identified with the Fe_2O_3 phase in Fe-V_2O_5 as a function of Fe molar concentration

hkl	0 %	5%	10%	15%	25%	30%	35%	40%	60%	80%
103		--	17,41	17,35	17,34	17,36	17,34	--	17,36	--
112		--	--	--	--	19,14	19,09	19,14	--	--
105		--	--	--	24,21	--	--	--	--	--
203		--	--	--	--	27,59	--	27,63	--	--
209		--	--	--	--	--	--	45,34	--	--
316		--	--	--	--	--	--	47,28	--	--
0012		50,56	50,65	50,62	--	50,64	50,62	50,63	50,40	50,45

Table 3.6(a) Lattice constants of V_2O_5 for all Fe concentrations

Fe concentration	a	b	c
5%	11.5403	3.5725	4.3838
10%	11.5324	3.5676	4.3822
15%	11.5404	3.5636	4.3832
25%	11.5460	3.5673	4.3819
30%	11.5409	3.5850	4.3863
35%	11.5466	3.5812	4.3837
40%	11.5470	3.5721	4.3729
60%	11.5469	3.5894	4.3791
80%	11.5092	3.6194	4.3836
Mean	11.54(1)	3.58(2)	4.382(4)
Theory	11.51	3.559	4.371

Table 3.6(b) Lattice constants of θ-VOB for all Fe concentrations

Fe concentration	a	b	c	γ
5%	12.1170	3.6955	10.2137	101°05'
10%	12.0590	3.6953	10.2230	100°52'
15%	12.0882	3.6903	10.2524	101°01'
25%	12.1077	3.6930	10.2544	101°02'
30%	12.0939	3.6932	10.2631	101°05'
35%	12.1039	3.6973	10.2581	100°50'
40%	12.0980	3.6965	10.2498	100°53'
60%	12.0973	3.6967	10.2513	100°53'
80%	12.0956	3.6948	10.2483	101°01'
Mean	12.10(2)	3,695(2)	10.25(2)	100°58'(6)
Theory	12.19(2)	3.68(1)	10,23(2)	102°30'

Table 3.6(c) Lattice constants of Fe_2O_3 for all Fe concentrations

Fe concentration	a	c
5%	8.3421	25.1474
10%	8.3491	25.1113
15%	8.3467	25.1249
25%	8.3430	25.1436
30%	8.3493	25.1154
35%	8.3471	25.1258
40%	8.3459	25.1231
60%	8.3298	25.2087
80%	8.3369	25.1894
Mean	8.343(6)	25.14(3)
Theory	8.34	25.02

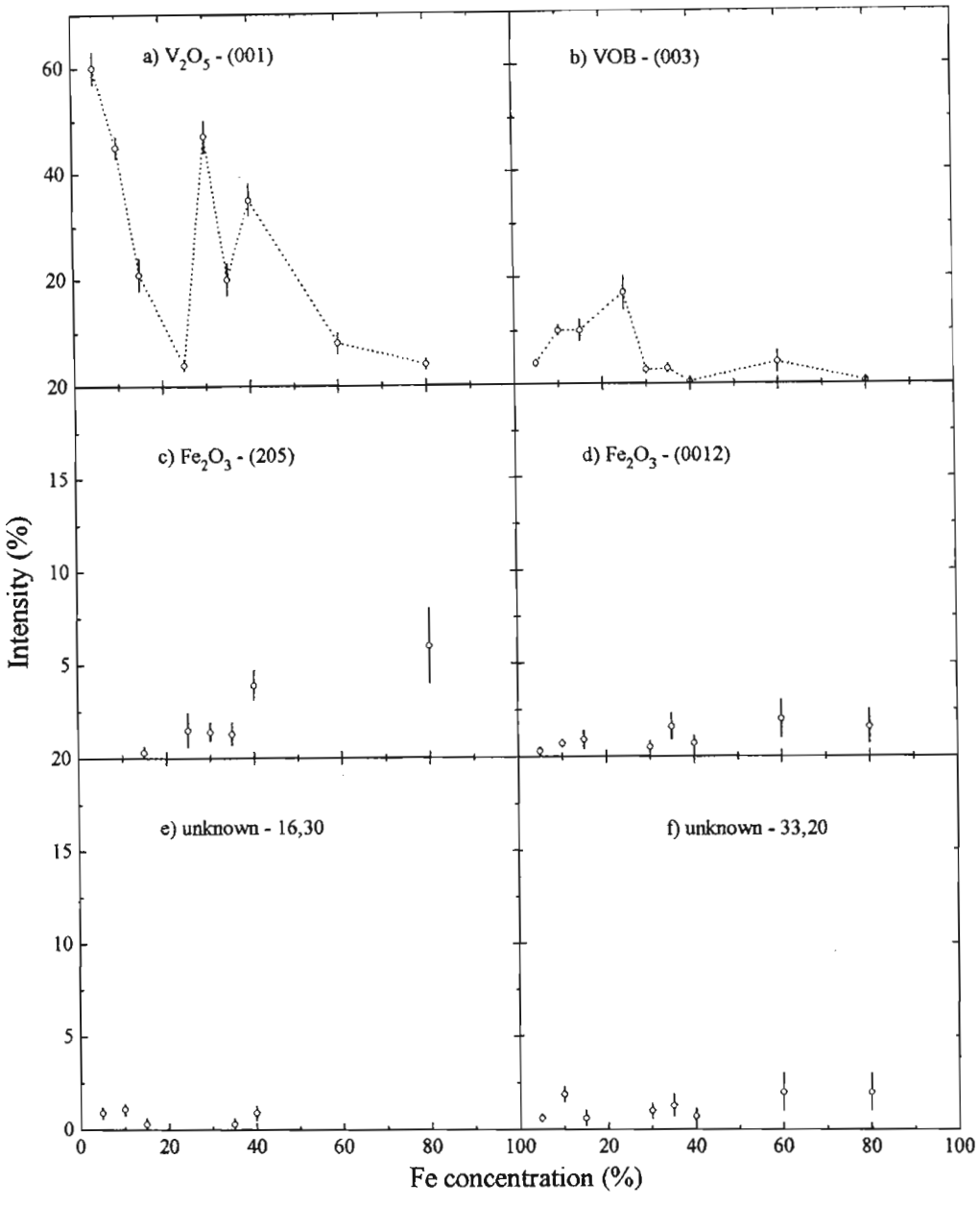

Fig. 3.11. Intensity contributions of the identified phases in Fe-V_2O_5 as determined from diffraction measurements

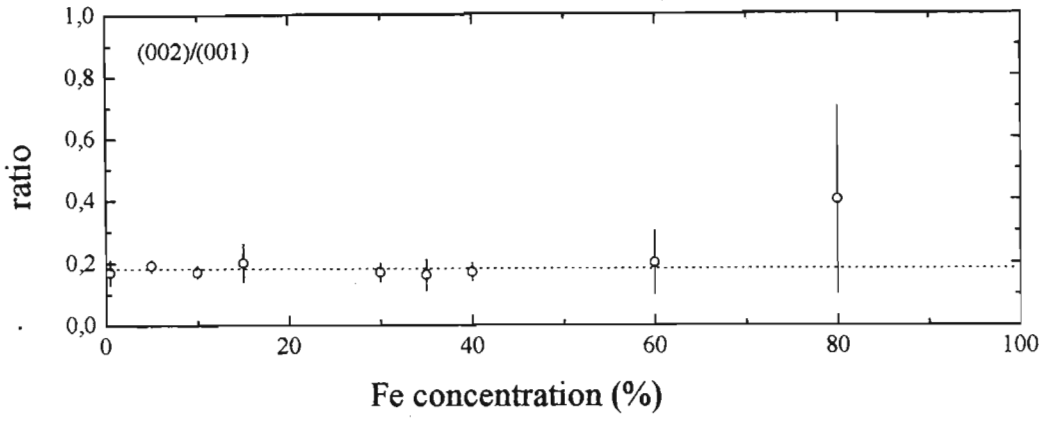

Fig. 3.12(a). Ratio of x-ray reflections of V_2O_5 in ⟨001⟩ crystallographic direction. The dotted line represents the expected ratio [BOR70]

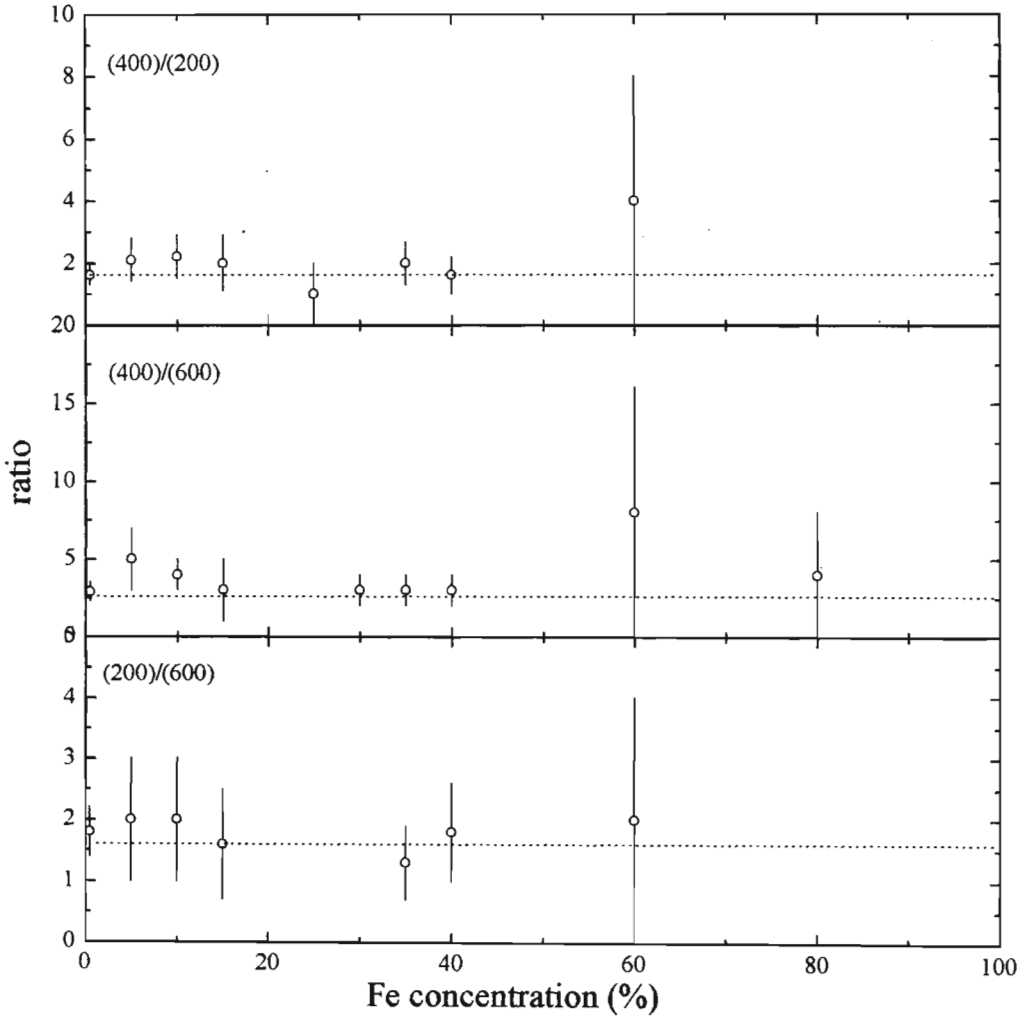

Fig. 3.12(b). Ratio of x-ray reflections of V_2O_5 in ⟨200⟩ crystallographic direction. The dotted line represents the expected ratio [BOR70]

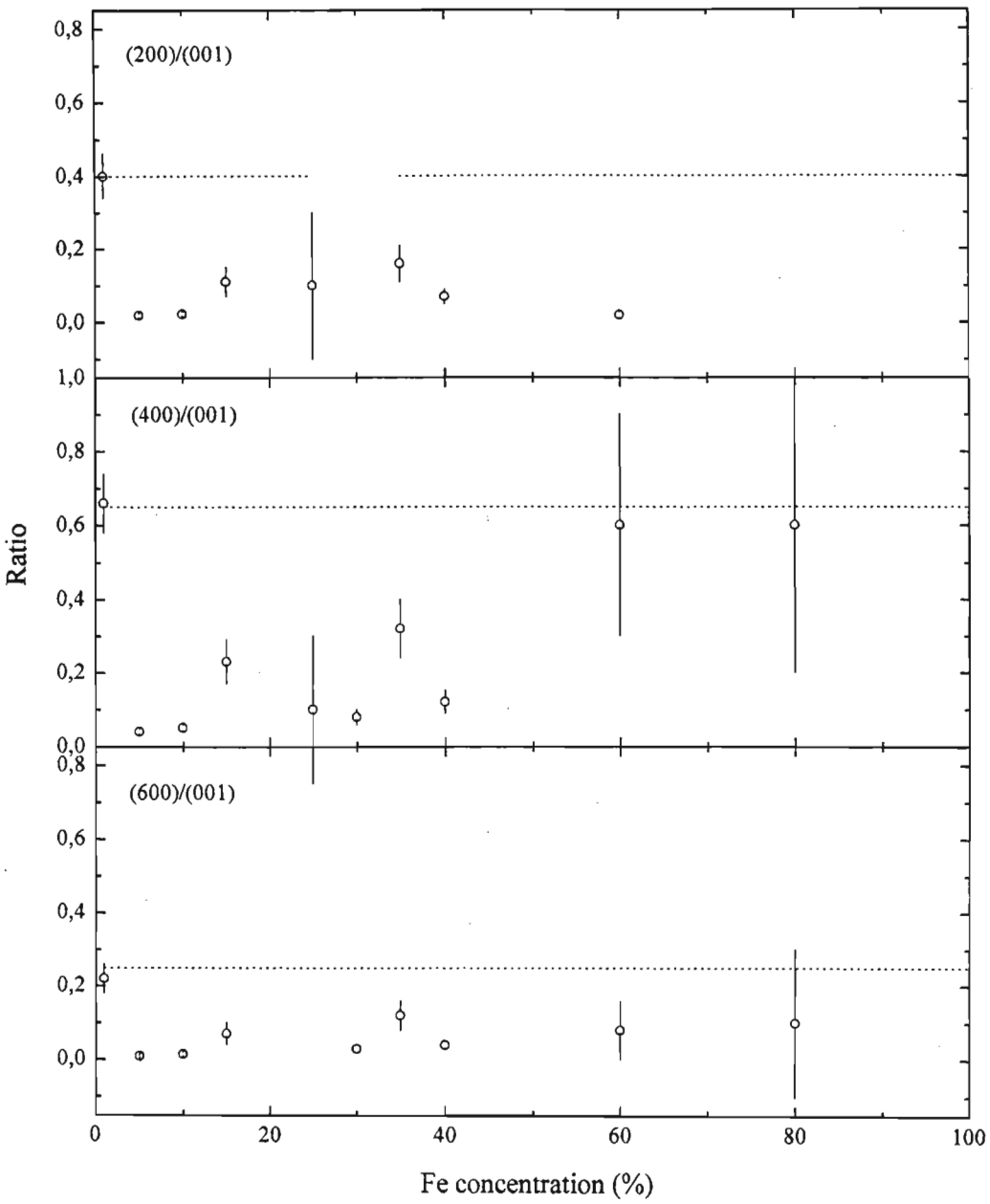

Fig. 3.12(c). Ratio of x-ray reflections of V_2O_5 in ⟨200⟩ and ⟨001⟩ crystallographic direction. The dotted line represents the expected ratio [BOR70]

3.2.6 Assignment of components in the Mössbauer spectra.

In order to assign the various components observed in the Mössbauer spectra to the four phases observed in the x-ray diffraction spectra, it is advisable to consider first how these different phases arise in the preparation of the samples.

In preparing the samples, the temperature of the mixture (1023 K) was just above the melting point of V_2O_5 (943 K) but quite far from the melting point of Fe (1808 K). This then means that during the time that the mixture was at 1023 K, the V_2O_5 material was in the molten state, but the Fe particles were still in the solid state. Thus in the molten state, the V_2O_5 phase would absorb single Fe ions from the solid Fe particles into its structure and the Fe particles will decrease in size as they lose Fe ions. When the melt is allowed to cool gradually, the V_2O_5 phase assumes solid state crystalline structure. However, the type of crystal structure that results will depend on the amount of Fe ions trapped in the molten state.

If the Fe concentration is very small, the initial orthorhombic structure of V_2O_5 is formed again, but as Fe doped V_2O_5. If the concentration of the Fe ions in the molten V_2O_5 state is large, then on cooling, a modified structure of the orthorhombic V_2O_5 will form, the monoclinic vanadium oxide bronze, θ-VOB.

There is a maximum limit of Fe ions needed to create the vanadium oxide bronze [GAL67]. This means then that the fraction of Fe particles that will take part in the creation process to the total amount of Fe present will depend on the ratio of the molar

concentration of the V_2O_5 powder and the Fe powder in the initial mixture. This fraction of Fe particles will therefore decrease as the molar concentration of the Fe powder in the preparation mixture increases. Stated another way, the percentage of Fe particles left unchanged, i.e. not losing their size, compared to the total Fe concentration will increase.

During the cooling process of the melt, the Fe particles will be oxidised to Fe_2O_3, since the reaction is conducted in air. However, depending on the size of the iron particles, the iron oxide will either be superparamagnetic or ferromagnetic [KUN66]. The superparamagnetic phase corresponds to the small iron oxide particles of size $d \approx 10$ nm (those particles involved in the creation of the vanadium oxide phases), the ferromagnetic phase will correspond to large iron oxide particles (those particles which did not interact with the molten V_2O_5). The Mössbauer component of a superparamagnetic phase should therefore present itself as doublet [KUN66], and the ferromagnetic phase as a normal magnetic sextet.

From the x-ray spectra, it is observed that the ferromagnetic α-Fe_2O_3 phase increases in contribution as the Fe concentration of the melt increase (see Fig. 3.11 (c) and (d)). Correspondingly, the intensity of the magnetic sextet *g* of the Mössbauer spectra (Fig. 3.7(g)) also increases in percentage contribution. The splitting of the inner two lines of this sextet of 2,6(1) mm/s corresponding to a hyperfine field, B_{hf} = 52,2(5) T, together with the isomer shift δ = 0,49(4) mm/s, is in close agreement with that observed by other authors as listed in Greenwood, pg 241, [GRE71]. Here the isomer shift is reported as 0,38

mm/s with the magnetic field of 51,5 T. We can therefore assign sextet g as belonging to the ferromagnetic α-Fe_2O_3.

To assign a doublet to the superparamagnetic α-Fe_2O_3 phase, we note that Kundig et al. [KUN66], in observing both the superparamagnetic and ferromagnetic components of Fe_2O_3, have found that the isomer shifts of both the components to be equal. Further they observed that for the grain sizes ranging from below 10 nm to 18 nm, the doublet splitting, ΔE_Q, was observed to lie between 0,68 mm/s and 0,44 mm/s, with the larger grains displaying smaller splittings in comparison with the smaller grains. Doublets with ΔE_Q in this range were therefore expected to be observed in the Mössbauer spectrum.

From our results, we note that doublets e and f have small quadrupole splittings of 0,13(2) mm/s and 0,14(2) mm/s, respectively. However, the isomer shift of doublet e of 0,60(6) mm/s is closer to the isomer shift of the magnetic component g than doublet f. On the basis of this we can assign doublet e to the superparamagnetic phase of α-Fe_2O_3. We further note that the intensity contribution of this component in the Mössbauer spectra remains fairly constant, implying that there is an upper limit to the amount of Fe absorbed into the vanadium oxide systems under consideration. This assignment is also in agreement with those of Abdullaev et al. [ABD69], and Burzo et al. [BUR78]. Both these authors had prepared doped V_2O_5 using Fe_2O_3 instead of Fe powder as the second partner in the solid state reaction.

To assign the components of the Mössbauer spectra to the θ-VOB phase, we need to consider the sample with 25% molar Fe concentration in the melt. The intensities of the reflections in the x-ray spectra, shown in Figs. 3.11 (a) and (b), indicate that the θ-VOB phase is dominant at this concentration, and the intensities of the components in the Mössbauer spectra, shown in Fig. 3.7, indicates that the doublets a and b are dominant at this concentration. We therefore conclude that doublets a and b belong to the θ-VOB phase.

In order to assign the remaining components c, d and f of the Mössbauer spectra to sites in the doped V_2O_5 phase we need to consider the following:

1. We have assigned components to sites in the θ-VOB phase, magnetic α-Fe_2O_3 phase, and the superparamagnetic α-Fe_2O_3 phase. The remaining components c, d and f should therefore correspond to either sites in Fe doped V_2O_5 or an unknown phase.
2. The intensity contribution of the Mössbauer spectra of doublet c remains constant, and doublet d shows a decrease as the Fe concentration of the melt increases, whereas doublet f shows an increase in intensity contribution with increasing Fe concentration. (Fig. 3.7(c), (d) and (f)).
3. The x-ray spectra indicates that the doped V_2O_5 phase decreases in concentration as the Fe concentration increases, whereas the unknown phase increases in concentration as the Fe concentration increases (Fig. 3.11 (a) and (f)).
4. The quadrupole splittings of doublets c and d can be taken as equal in comparison with the quadrupole splittings of doublet f and are much more larger than the f.

(Table. 3.2 (b))

5. Abdulleav et al. [ABD69] and Burzo et al. [BUR78], who have made Mössbauer measurements on Fe_2O_3 - V_2O_5, have observed only two components which correspond to doublets c and d, and they do not report the presence of a component with the parameters of the unknown phase required to fit the present data.

It is therefore concluded that the doublets c and d correspond to sites in the Fe doped V_2O_5 phase and doublet f belongs to an hitherto undetermined phase.

For Fe concentrations at 40% or lower, the reflection intensities in the x-ray spectra, shown in Fig. 3.11, indicate that the V_2O_5 phase is dominant, with the exception at 15% and 35% Fe concentration, where the θ-VOB phase is dominant. Therefore, the Mössbauer components corresponding to the θ-VOB phase, doublets a and b, should display a sharp maximum at 25% Fe concentration, and the doublets c and d, corresponding to Fe doped V_2O_5, should display a dominance in the intensity contribution to the Mössbauer spectra at 5%, 10% and 30% Fe concentrations. However, as is seen in Fig. 3.7, the doublets *a* and *b* continue to display a dominance for entire range of Fe concentrations less than 40%.

The x-ray spectra, however, is the result of the interaction of all the ions present in the material with the x-rays, i.e. this includes both the V and Fe ions. The Mössbauer spectra, on the other hand, involves only the interaction of the ^{57}Fe nuclei in the material. In the θ-VOB phase, with the structure written as $Fe_xV_2O_5$, x can range between 0,33 and 0,38 [GAL67]. This means that the ratio of the Fe ions with the V ions will be between 0,33/2 and 0,38/2.

In the Fe doped V_2O_5 phase, where the structure remains essentially the same as pure V_2O_5, even if one assumes that Fe substitutes V by 1%, the ratio between the Fe in the Fe doped V_2O_5 phase to that of the V ions in this phase will be 1/100. Thus even if one took equal concentration of the θ-VOB phase and the Fe doped V_2O_5 phase, in the Mössbauer spectra, the intensity contribution from the θ-VOB phase will be much greater than the intensity contribution from the Fe doped V_2O_5 phase, i.e. doublets a and b should contribute more strongly than doublets c and d for Fe concentrations below 40%. This therefore explains the dominance of the a and b doublets for the Fe concentrations lower than 40%.

To further support the assumption that Fe is actually substituting V in the Fe doped V_2O_5 phase, one needs to compare the x-ray lines of the doped V_2O_5 phase with pure V_2O_5. Looking at the x-ray spectra of 5%, 10%, 15%, and 25%, we first note that the (001) and (002) reflections are much greater than the (200), (400) and (600) reflections, which is an indication of a preferred orientation in the samples, (Fig 3.10 and 3.12(c)). However, in comparing the (001)/(002), (400)/200), (400)/600) and (200)/(600) intensity ratios, we notice that these ratios lies within the expected value, as is shown in Fig. 3.12(a) and (b). This confirms that the Fe ions are occupying substitutional sites in the V_2O_5 lattice. If these atoms were not at substitutional sites, then the structure factors of the $Fe_xV_2O_5$ crystal would change, resulting in a change of the intensity ratios. Further evidence for substitution lies in the results that the lattice constants for the doped V_2O_5 phase are the same as that of

the pure V_2O_5 phase, as shown in Table 3.6(a), implying that the Fe must be entering the V_2O_5 phase in small amounts, such that crystallographic unit cells remain unchanged.

3.2.7. Electrical conductivity measurements of Fe-V_2O_5 samples.

Electrical conductivity measurements were conducted on the pure V_2O_5 powder and samples containing 5%, 15%, and 80% Fe concentrations, as a function of the sample temperature. The voltage supplied across the powder was 30,0V, with a fluctuation of 0,2V. Fig 3.13 shows the results as a plot of $\ell n(I)$ *vs* $1/T$ where I is the measured current and T the temperature.

Materials which display semiconducting behaviour have their electrical conductivity described by the equation [KHA90, NII91]

$$\sigma = \sigma_0 \exp\left(-W/k_B T\right) \qquad 3.1$$

where W is the activation energy.

In terms of the current I passing through the material, this can be written as

$$I \propto \exp\left(C/T\right)$$

where C is taken as a constant defined by Eqn. (3.1). Thus a plot of $\ell n(I)$ *vs* $1/T$ should be linear. As can be seen from Fig. 3.13, this nature is indeed displayed by the materials that we have studied. We can thus conclude that the materials each displays semiconducting natures. These results are similar to the results of Bara et al., [BAR85]. However, they had only measured the electrical conductivity of the θ-VOB phase.

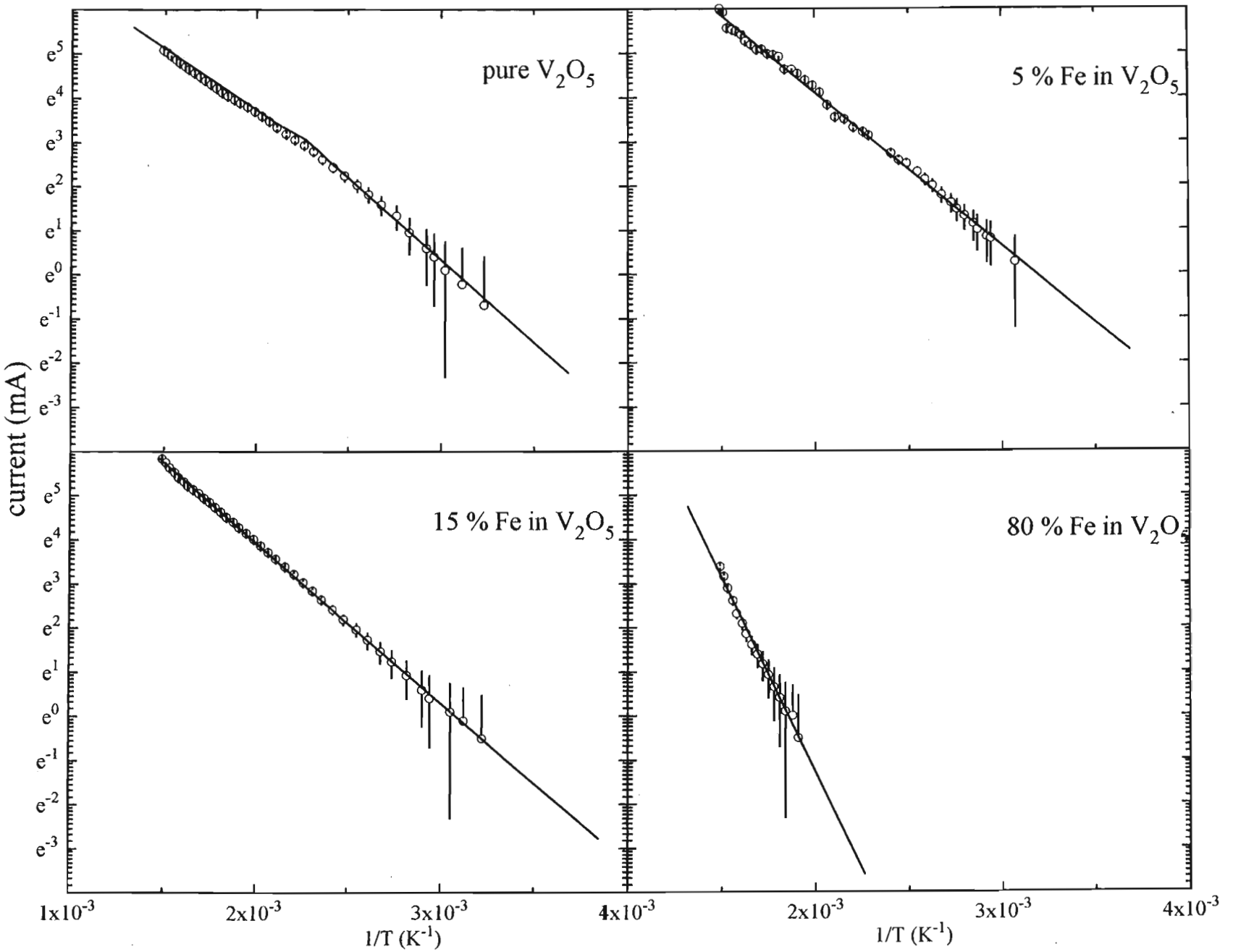

Fig. 3.13. Electrical conductivity measurements on V_2O_5 samples containing Fe

Further, as can be seen in Fig. 3.13, the pure V_2O_5 sample displays two regions of linearity, with the transition at $T_c = 458$ K, which is an indication that the semiconducting properties of the sample changes at this temperature.

Eqn. (3.1) can be rewritten as

$$\ell n(I) = \ell n(I_0) - \frac{W}{kT}$$

Comparing this equation with the general equation for a straight line

$$y = A + Bx,$$

with $y = \ell n(I)$ and $x = 1/T$, we get for the activation energy

$$W = -kB$$

Thus, the constants A and B, used to fit lines though the data for all the cases shown in Fig. 3.13, were evaluated, and the results are listed in Table 3.7, together with W.

Table 3.7. The activation energy W calculated for the samples with 0%, 5%, 15% and 80% Fe concentration.

Fe concentration	A	B	W (eV)
0% $< T_c$	11.426	-3718.8	0.321(5)
$> T_c$	9.164	-2764.9	0,238(5)
5%	11.050	-3471.7	0.299(5)
15%	11.229	-3646.5	0.314(5)
80%	16.323	-8801.8	0.758(5)

IV ^{111}In TIME DIFFERENTIAL PERTURBED ANGULAR CORRELATION AND RELATED MEASUREMENTS ON V_2O_5 AND VO_2.

4.1 EXPERIMENTAL

4.1.1 Ion implantation of V_2O_5 and VO_2 with ^{111}In.

The vanadium oxide targets were prepared by pressing commercially obtained powders onto various metallic backings: for V_2O_5 powders silver foils were used, and for the VO_2 powders silver, palladium and platinum foils were used. ^{111}In was ion implanted into these targets at 400 keV using the Göttingen heavy ion implanter IONAS [UHR85]. After implantation, the targets were placed into metallic pockets made out of the backing material. These samples were then placed in plastic sample holders for the TDPAC measurements.

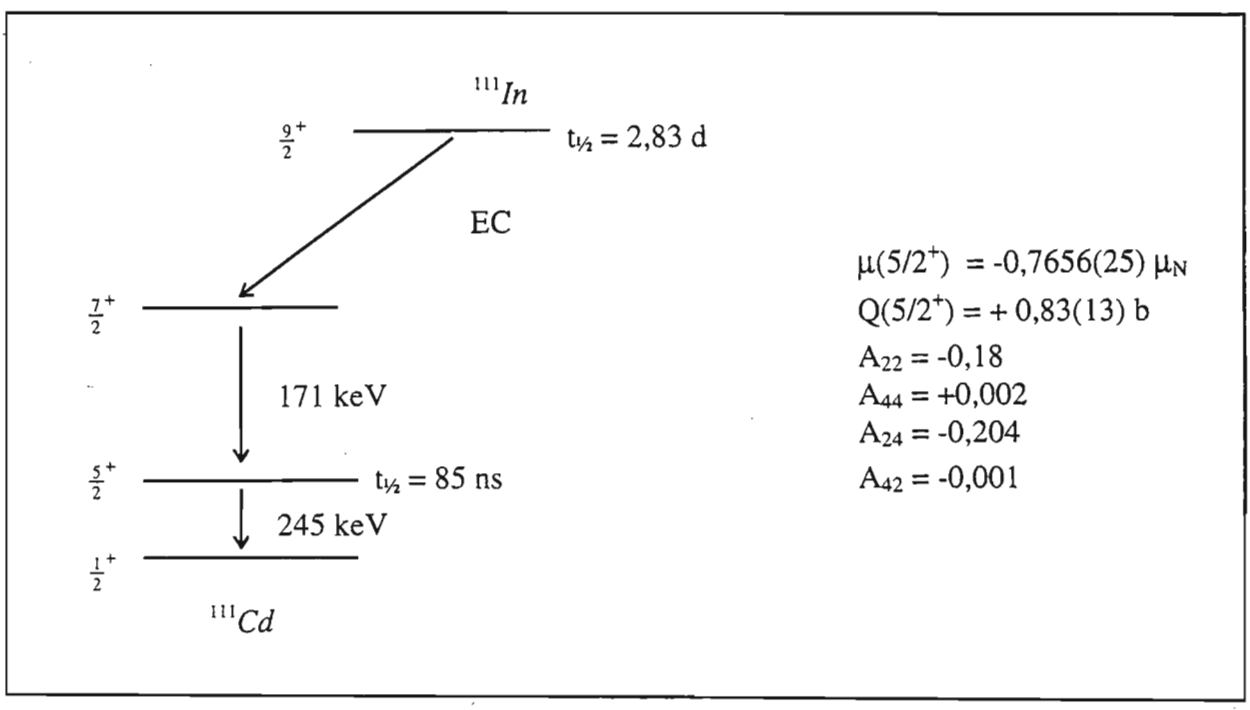

Fig.4.1. Decay Scheme of ^{111}In.

4.1.2 The TDPAC measuring apparatus

The source used for the TDPAC measurements was ^{111}In, and the nuclear decay scheme is shown in Fig. 4.1.

The TDPAC spectra were recorded using a conventional set-up of four NaI(Tl) detectors in 90° geometry, as shown in Fig. 4.2.

The two single channel analysers (SCA's) served to separate the ^{111}In gamma cascade photons (171 and 245 keV), and the constant fraction discriminator (CFD) was used to establish the time of either event. Thus, the first set of SCA's attached to each detector produced logic pulses whenever a γ_1 was observed (which was the start signal of energy 171 keV) and the second set of SCA's attached to each detector, produced a logic signal whenever γ_2 was observed (which was the stop signal of energy 245 keV). These logic signals together with those from the CFD's were then fed to a router which served two purposes. The first was to check the coincidence between the energy and the time logic signals, so that the event could be accepted as a true event or rejected as a false event. The second was to route the events in terms of the detectors that had produced the start and stop signals. In this set up, the entire four detectors could yield both start and stop signals and sixteen coincidence spectra were possible, of which only twelve were valid. Each of these spectra would then have the form

$$N_{ij}(\theta,t) = N_0 \exp\left(-t/\tau_N\right) W(\theta,t) + B .$$

where B is the random background, $W(\theta,t)$ is the time dependent angular correlation function, and θ is the angle between the detectors i and j. These twelve time spectra were collected on an Atari ST1040 computer [BAR93], which was interfaced with the router. From these twelve spectra, the $R(t)$ function was then calculated using the formula

$$R(t) = \frac{2}{3}\left[\sqrt{\frac{N_{13}(180^o,t)N_{24}(180^o,t)}{N_{14}(90^o,t)N_{23}(90^o,t)}} - 1\right]. \qquad 4.1$$

Eqn. 4.1. is related to Eqn. 2.16 [BOL87]:

$$R(t) = A_2^{eff} G_2(t), \qquad 4.2$$

where the effective anisotropy coefficient A_2^{eff} was measured separately using a sample which experienced an unperturbed angular correlation, $G_2(t) = 1$.

From Eqn. (2.16) and Eqn. (2.17), the periodic patterns which are observed in this experimental $R(t)$ function are therefore due to the transition frequencies ω_n. Therefore, the Fourier transformed experimental $R(t)$ function will exhibit a triplet of ω_n values, which then yields a unique determination of the coupling constant ν_Q and the asymmetry parameter η.

A least squares fit was therefore performed by comparing Eq. 4.1 with Eq. 4.2 using the code *NEUFIT* to yield the hyperfine parameters ν_Q and η. This code *NEUFIT* was developed by the TDPAC group at the Zweites Physikalishes Institut, Göttingen.

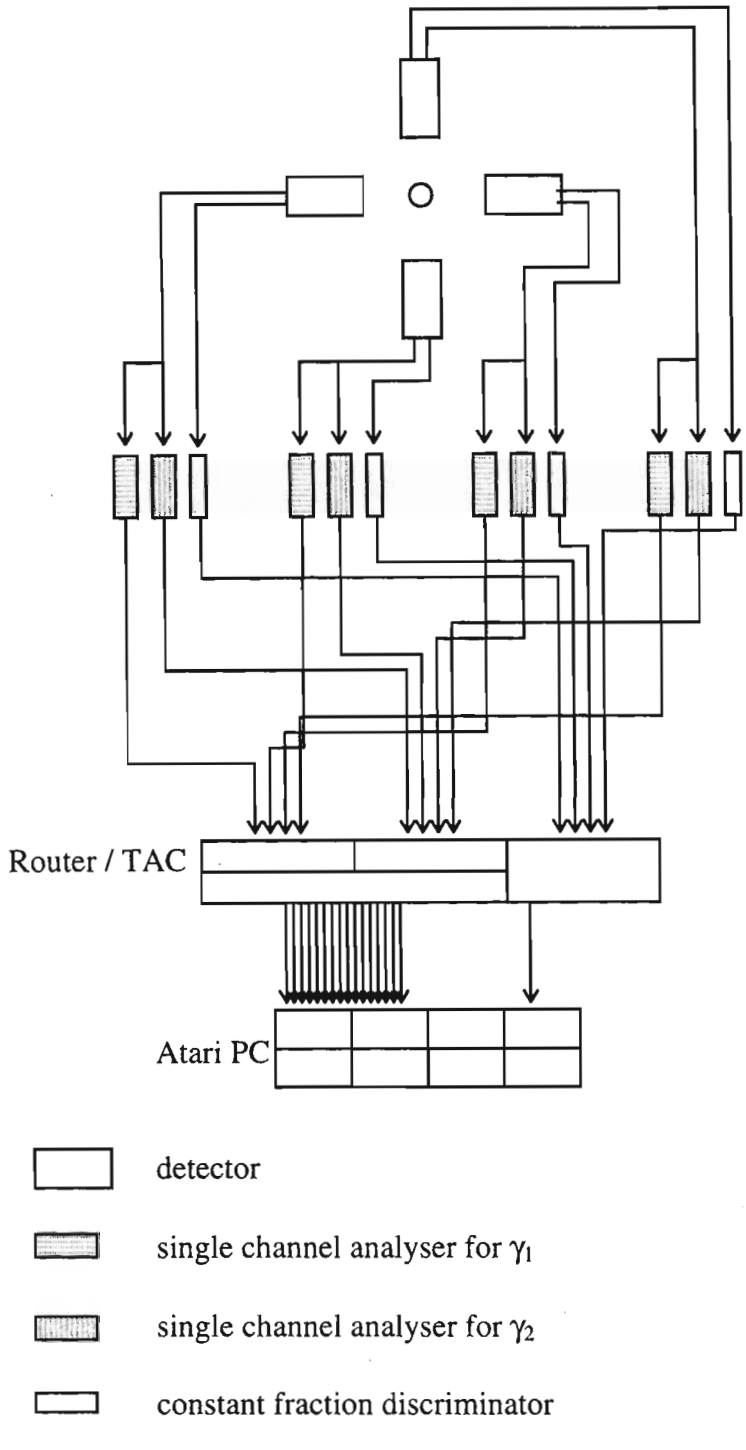

Fig 4.2. Schematic diagram of TDPAC apparatus.

4.1.3 Annealing of the samples implanted with ^{111}In

To remove radiation damage caused during the implantation, the samples were isochronally annealed at various annealing temperatures T_A, either in vacuum ($1x10^{-5}$ *mBar*) or in air. TDPAC spectra taken at room temperature in air after each annealing step were then performed to observe the effect of the annealing on the sample.

4.1.4 X-ray diffraction spectra related to TDPAC samples

Inactive V_2O_5 and VO_2 powders were annealed under similar conditions as those in the TDPAC measurements. X-ray powder diffraction spectra were subsequently performed on these powders, and the x-ray spectra were compared with those of Bryström et al. [BYS50]. These measurements were performed at the Mineröligische Petrologie Institüt, Universität Göttingen.

4.2 RESULTS AND ANALYSIS

4.2.1. V_2O_5

Two series of TDPAC measurements were performed on V_2O_5. In each series, the samples were annealed at increasing temperatures, and TDPAC spectra were acquired after each annealing step. The difference between the two series was that in the first series the sample was annealed in vacuum [$1x10^{-5}$ *mBar*], and in the second series the sample was annealed in air, with annealing times of one hour and 30 minutes for each series, respectively.

During the annealing of the first series, a reaction of V_2O_5 with the silver occurred at 923 K. This was seen as a black substance forming on the silver packet.

The resulting *R(t)* spectra together with their Fourier transform spectra are shown in Fig. 4.3 and Fig. 4.4, which were analysed using the standard fitting procedure *NEUFIT*.

4.2.1.1 Sample annealed in vacuum.

The *R(t)* spectra were analysed in terms of two components, f_1 and f_2, with quadrupole coupling frequencies ν_Q and spread δ listed in Table 4.1 (a). The contribution of f_1 (ν_Q = 90 MHz at 573 K) was observed to increase as a function of annealing temperature, increasing up to 74% at 873 K. Correspondingly, the second component, f_2, with ν_Q = 221 MHz and a very much broader distribuition δ = 31.9 MHz, was observed to decrease. This behaviour is illustrated in Fig. 4.5 (a).

4.2.1.2 Sample annealed in air.

Component f_1 (ν_Q = 91.4 Mhz, δ = 9.0 MHz) was again observed, but its contribution was observed to decrease from 46% to 25% with increasing annealing temperature. A broader frequency component f_3 (ν_Q = 265.3 MHz, δ = 61.4 MHz) was observed, with contribution increasing from 40% at T_A = 373 K to 63% at T_A = 613 K. An additional component with ν_Q = 224 MHz and δ = 9.9 MHz was required to fit the data. The behaviour of these components are illustrated in Fig. 4.5 (b).

To determine the crystallographic phases of the V_2O_5 powder as it underwent annealing, x-ray powder diffraction measurements were performed on inactive V_2O_5 powders subjected to the same annealing treatment as in series one and two. These spectra were then compared with those of Bryström et al. [BYS50]. The spectrum of the sample annealed at 870 K is shown in Fig. 4.6 together with the spectrum from Bryström et al.

These spectra show the samples remained in the V_2O_5 phase after the annealing treatment.

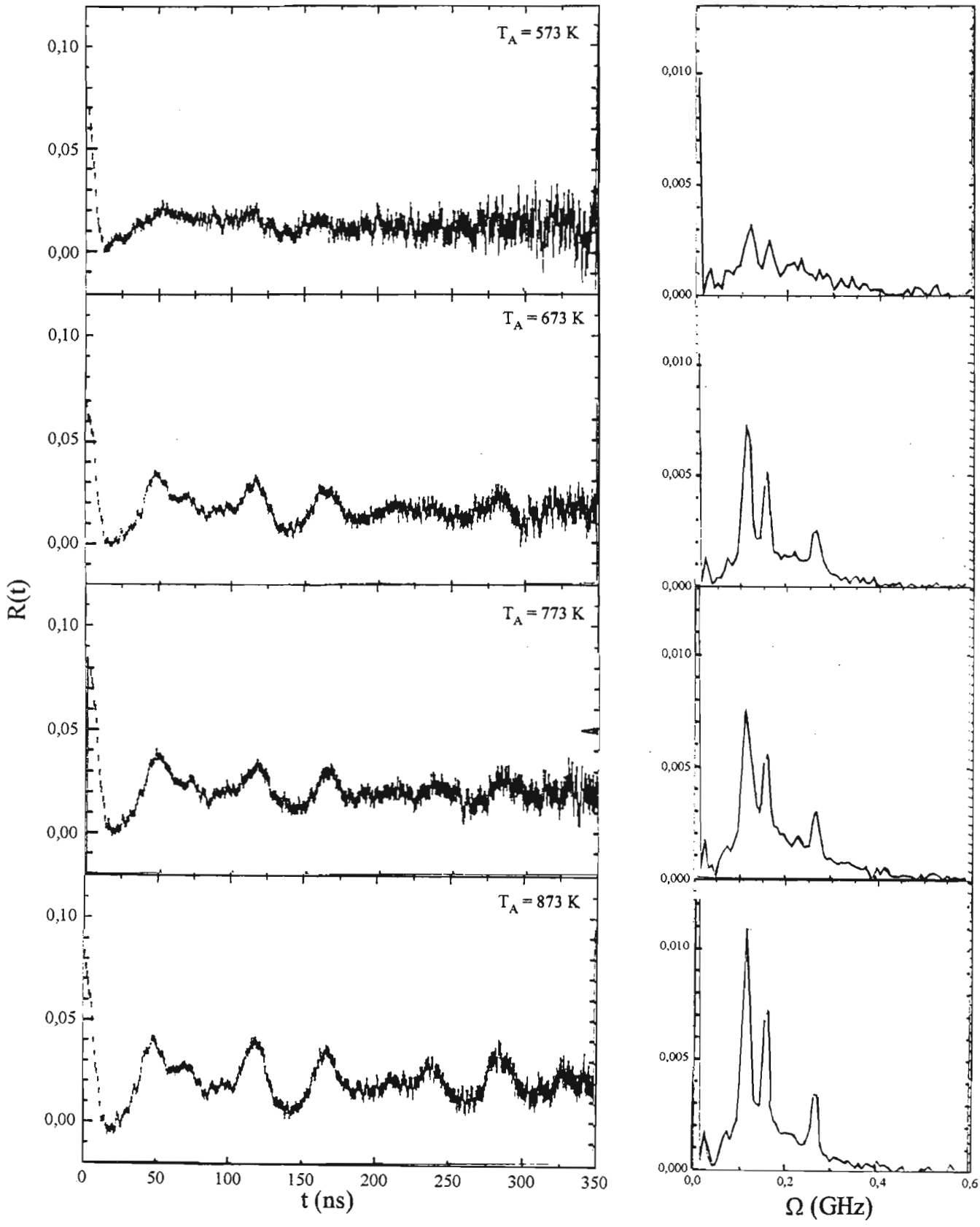

Fig. 4.3. R(t) spectra and the Fourier transforms of ^{111}In implanted V_2O_5 annealed in vacuum.

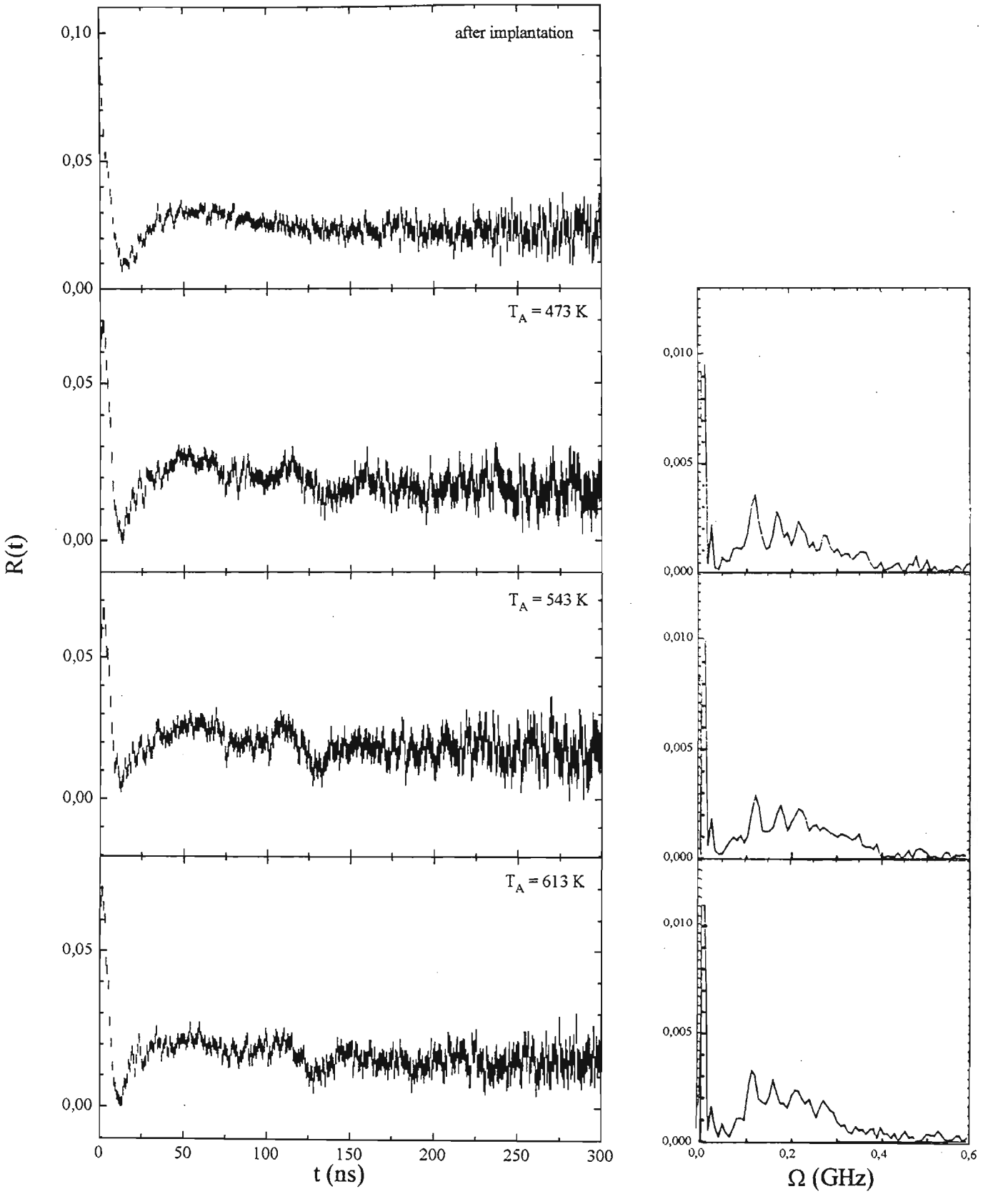

Fig. 4.4. R(t) spectra and the Fourier transforms of ^{111}In implanted V_2O_5 annealed in air.

Table 4.1a Hyperfine Parameters of V_2O_5 annealed in vacuum 1 x 10^{-5} mBar

	frequency f_1				frequency f_2			
T_A(K)	%	ν_Q(MHz)	η	δ(MHz)	%	ν_Q(MHz)	η	δ(MHz)
573	48	90,54	0,626	8,86	52	220,0	0,1	31,9
673	64	88,70	0,629	4,97	36	223,8	0,1	44,8
723	67	88,74	0,616	5,74	33	223,8	0,1	34,8
773	70	88,36	0,622	7,33	30	222,7	0,0	25,0
823	73	87,22	0,621	5,92	17	217,5	0,0	25,0
873	74	87,87	0,610	4,27	16	218,0	0,0	25,0
		88,1(3)	0,619(3)	5,6(5)				

Table 4.1b Hyperfine Parameters of V_2O_5 annealed in air

	frequency f_1				frequency f_3				frequency f_4			
T_A(K)	%	ν_Q(MHz)	η	δ(MHz)	%	ν_Q(MHz)	η	δ(MHz)	%	ν_Q(MHz)	η	δ(MHz)
373	46	90,57	0,604	9,93	40	265,3	0,0	51,4	14	216,5	0,0	10,0
473	28	91,13	0,602	7,86	62	265,3	0,0	68,6	10	222,8	0,0	9,9
543	28	92,45	0,631	9,15	66	265,3	0,0	97,9	6	229,2	0,0	9,7
613	25	98,46	0,544	9,91	63	265,3	0,0	64,5	12	229,2	0,0	9,9
		91,4(6)	0,612(9)	9,0(6)								

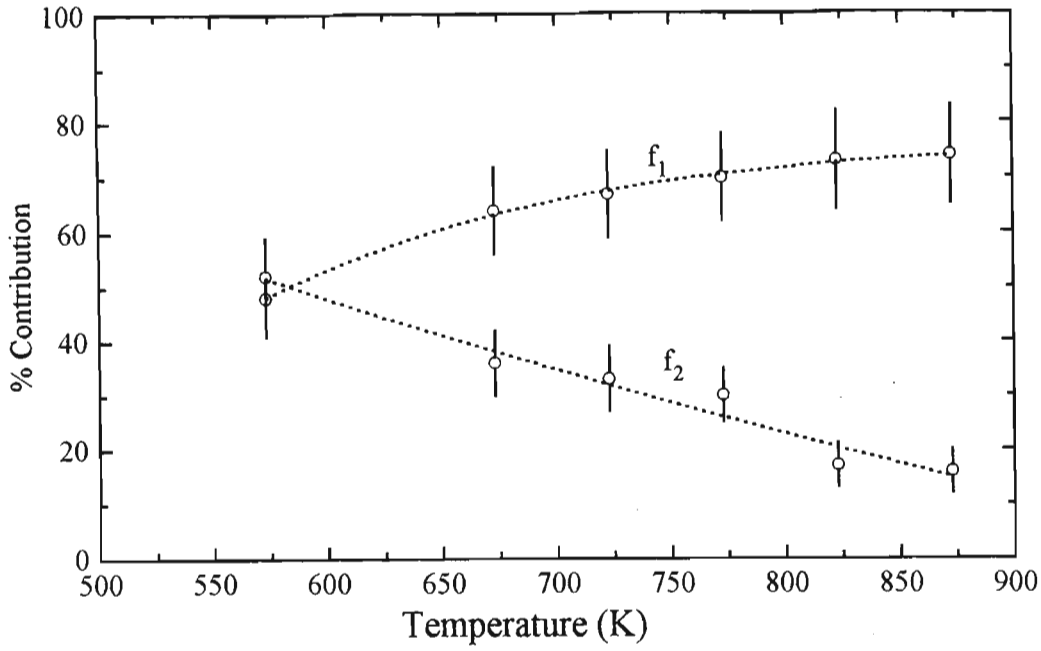

Fig. 4.5(a). Fractions observed in TDPAC spectra as a function of annealing temperature for V_2O_5 annealed in vacuum

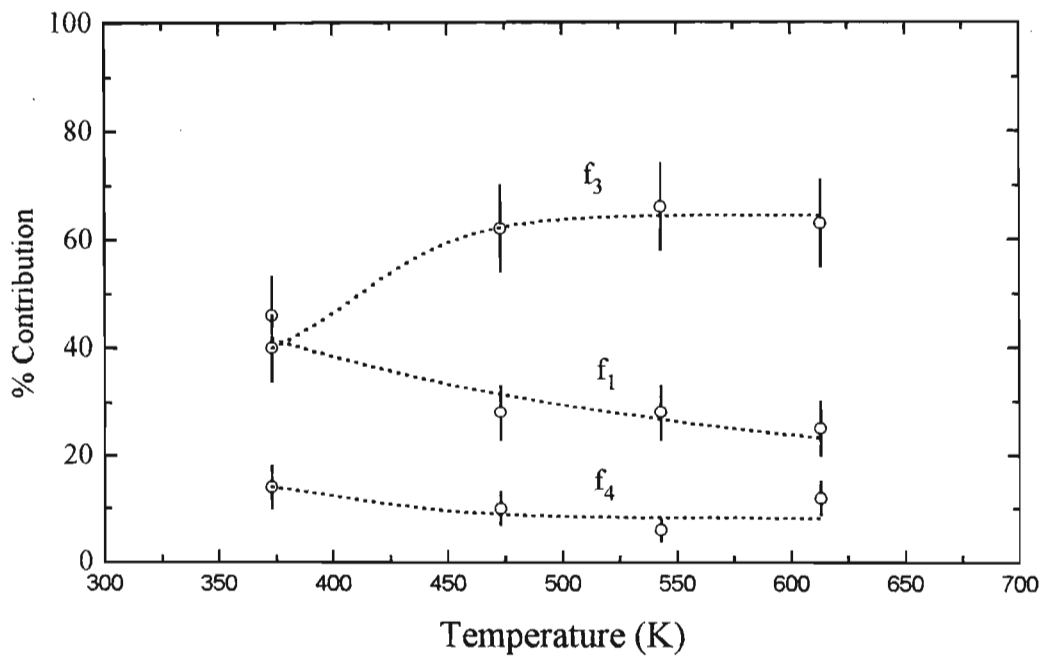

Fig. 4.5(b). Fractions observed in TDPAC spectra as a function of annealing temperature for V_2O_5 annealed in air

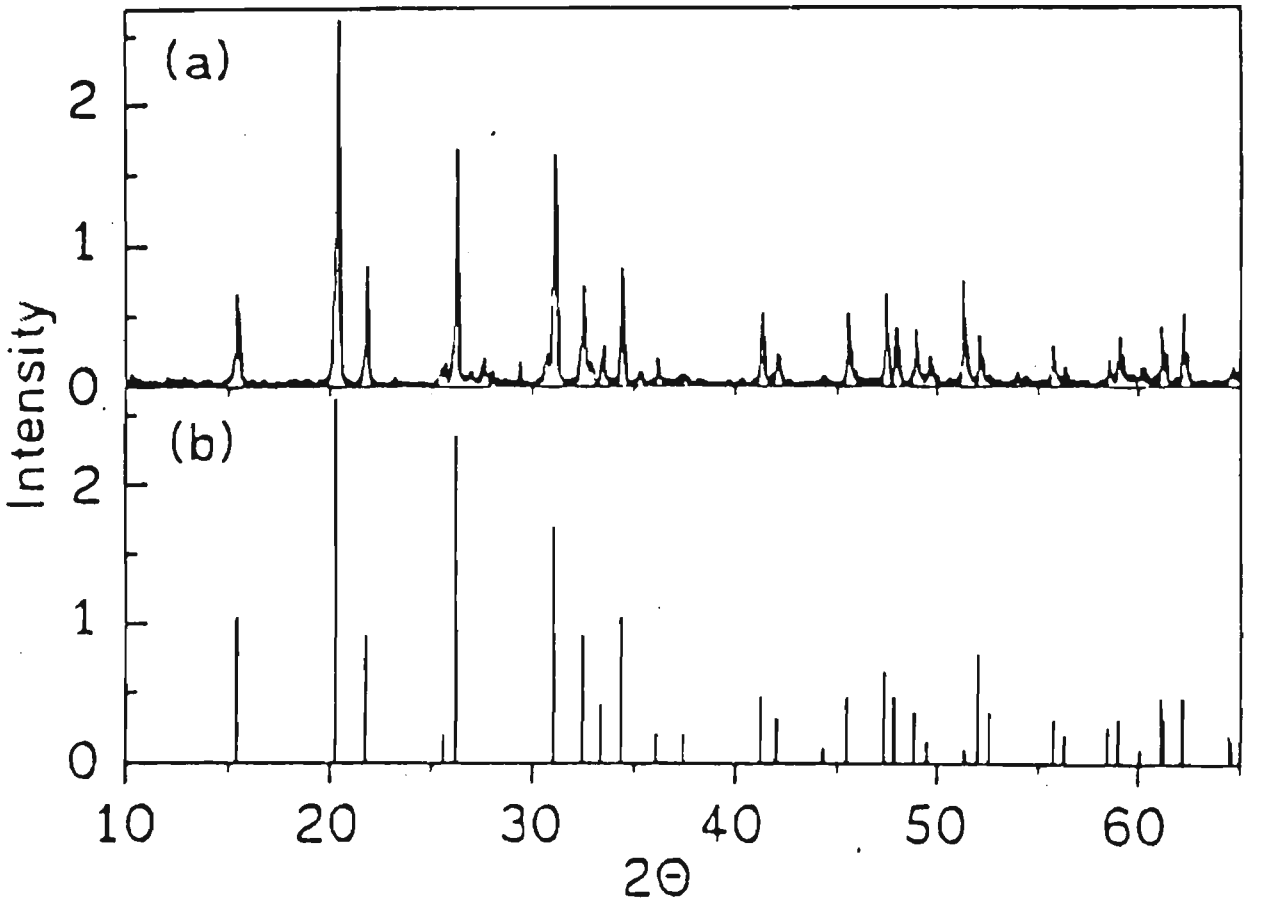

Fig. 4.6. X-ray spectrum of V_2O_5 after annealing at 870 K (a), in comparision with the results of of Bryström et al. [BYS50] (b)

4.2.2. VO_2

For the TDPAC measurements on VO_2, radioactive ^{111}In ions were implanted at 400 keV energy into two powder samples. The first sample was annealed at various temperatures in vacuum, and after each annealing, TDPAC spectra were acquired at room temperature. With the second sample, TDPAC measurements were performed on the sample directly after implantation as a function of the sample temperature, starting from room temperature up to 520 K.

The resulting *R(t)* spectra for both sets of measurements are shown in Fig. 4.7 and Fig. 4.8 and the hyperfine parameters obtained by fitting the spectra are listed in Table 4.2 (a) and (b).

In the annealed VO_2 sample, a component f_1 with a well defined quadrupole frequency ν_Q appears after annealing at 923 K. Besides the contribution of this distinct frequency, a second component f_2 with a broad frequency distribution is also required to fit the data. The percentage contribution of component f_1 increases with increasing T_A, while that of component f_2 shows a corresponding decrease. These results are shown in Fig. 4.9 (a).

For the isothermal TDPAC measurements, again two components f_3 and f_4 were observed, component f_3 with a well defined quadrupole frequency ν_Q, and component f_4 with a broad frequency distribution. However, the ν_Q values of the two components were quite different to those observed for the annealed samples. The percentage contribution of the frequency f_3 was also seen to increase with the measuring temperature as shown in Fig. 4.9 (b).

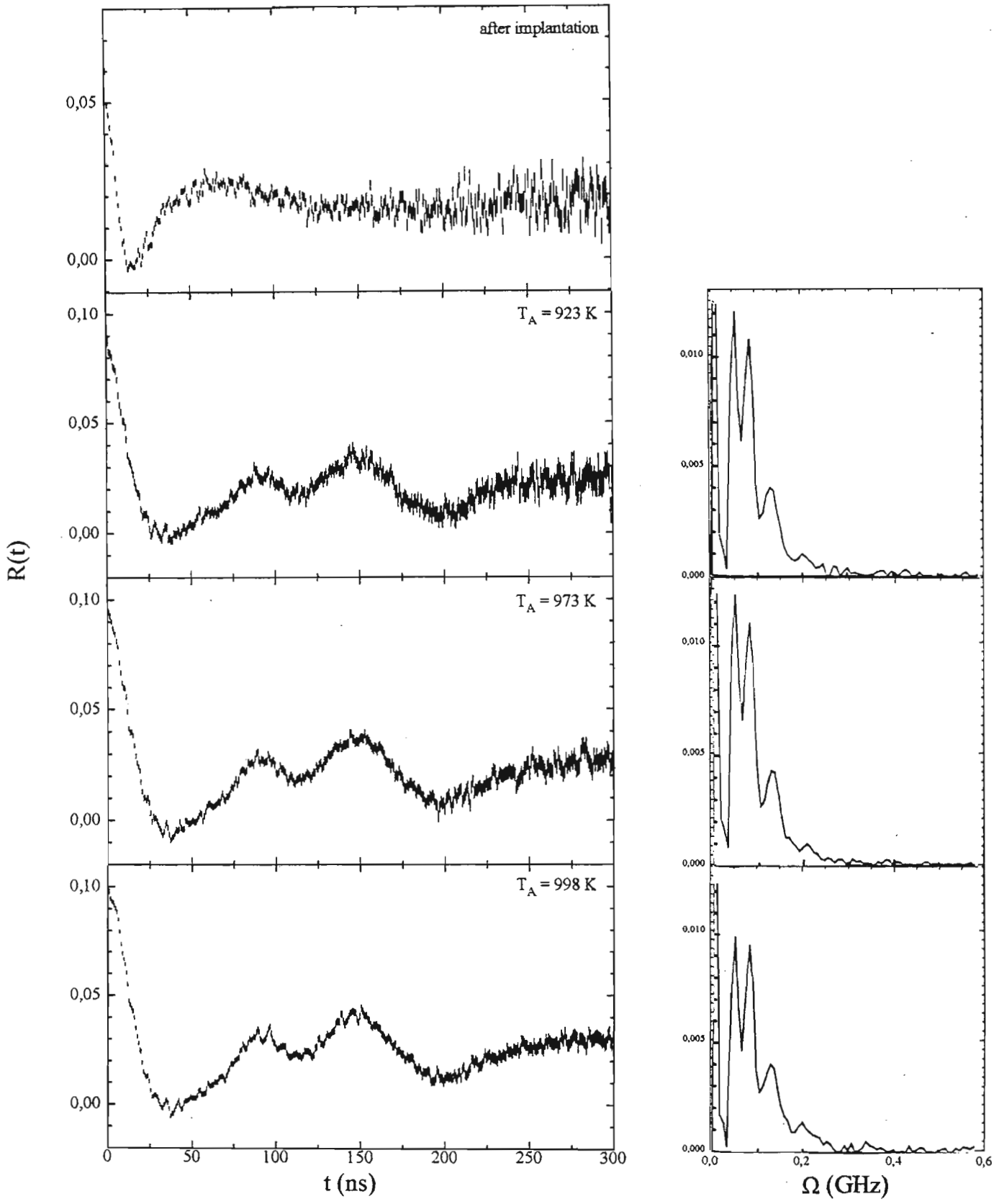

Fig. 4.7. ^{111}In-TDPAC measurements on VO_2 as-implanted, and after annealing in air at T_A = 923 K, 973K and 998 K.

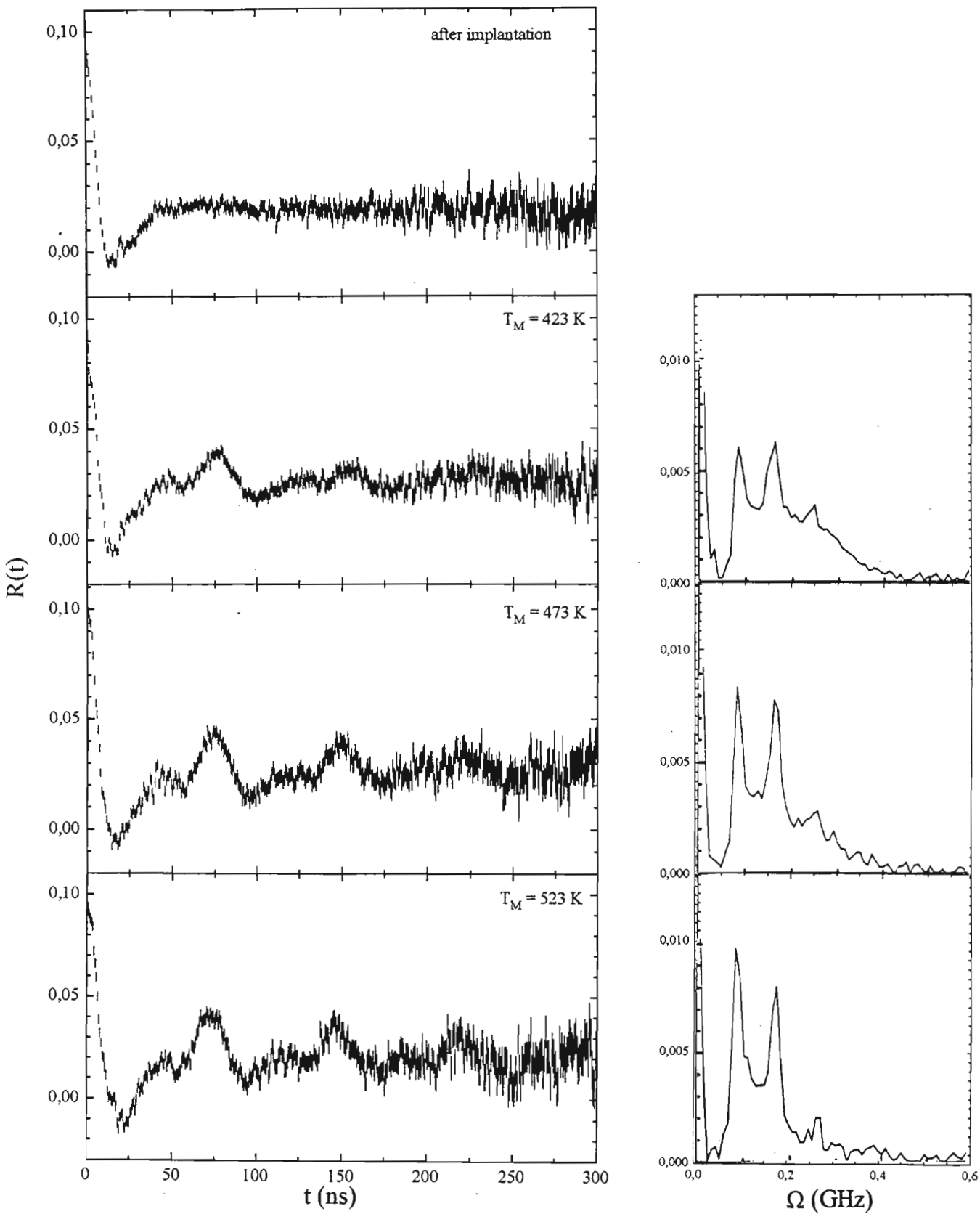

Fig. 4.8. R(t) spectra and the Fourier transforms of ^{111}In implanted VO_2 as a function of sample temperature.

Table 4.2(a) Hyperfine Parameters of VO_2 annealed in vacuum 1 x 10^{-5} mBar

	component f_1				component f_2			
T_A(K)	%	ν_Q(MHz)	η	δ(MHz)	%	ν_Q(MHz)	η	δ(MHz)
923	44	43,47	0,369	2,75	56	71,0	0,30	19,4
973	50	43,79	0,329	2,78	50	65,7	0,29	15,4
998	71	41,52	0,456	4,55	29	76,5	0,41	8,9
		43,0(7)	0,39(4)	3,4(6)				

Table 4.2(b) Hyperfine Parameters of VO_2 as a function of measuring temperature

	frequency f_3				frequency f_4			
T_M(K)	%	ν_Q(MHz)	η	δ(MHz)	%	ν_Q(MHz)	η	δ(MHz)
423	24	89,15	0,220	3,50	76	128,0	0,46	25,0
473	36	88,97	0,212	2,43	64	111,6	0,55	20,7
523	44	89,43	0,179	2,42	56	112,9	0,42	14,4
		89,1(1)	0,20(1)	2,8(4)				

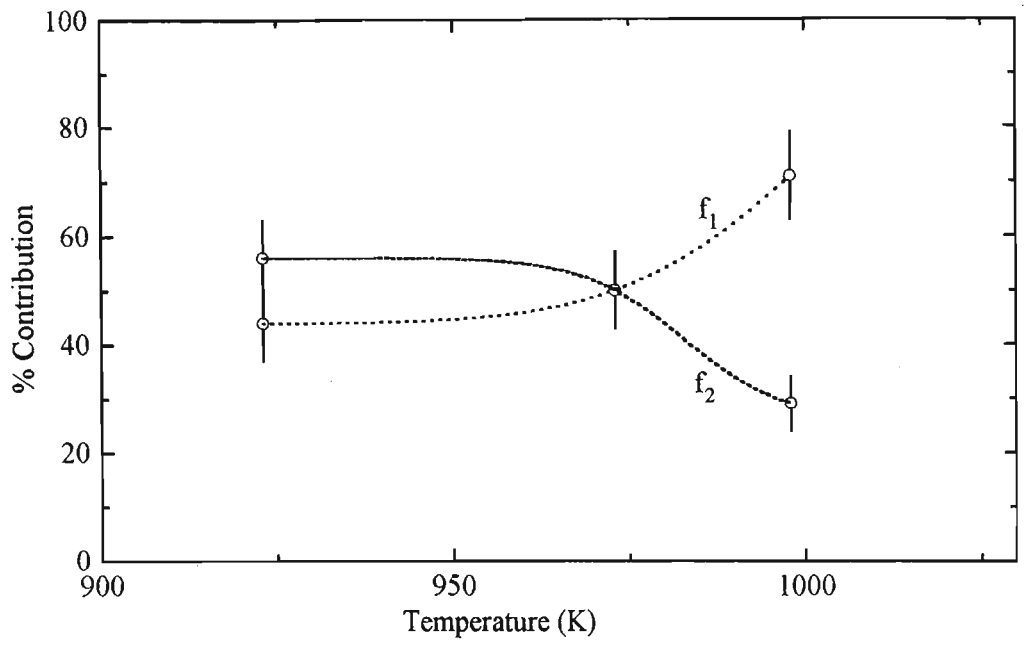

Fig. 4.9(a). Fractions observed in TDPAC spectra as a function of annealing temperature for VO_2

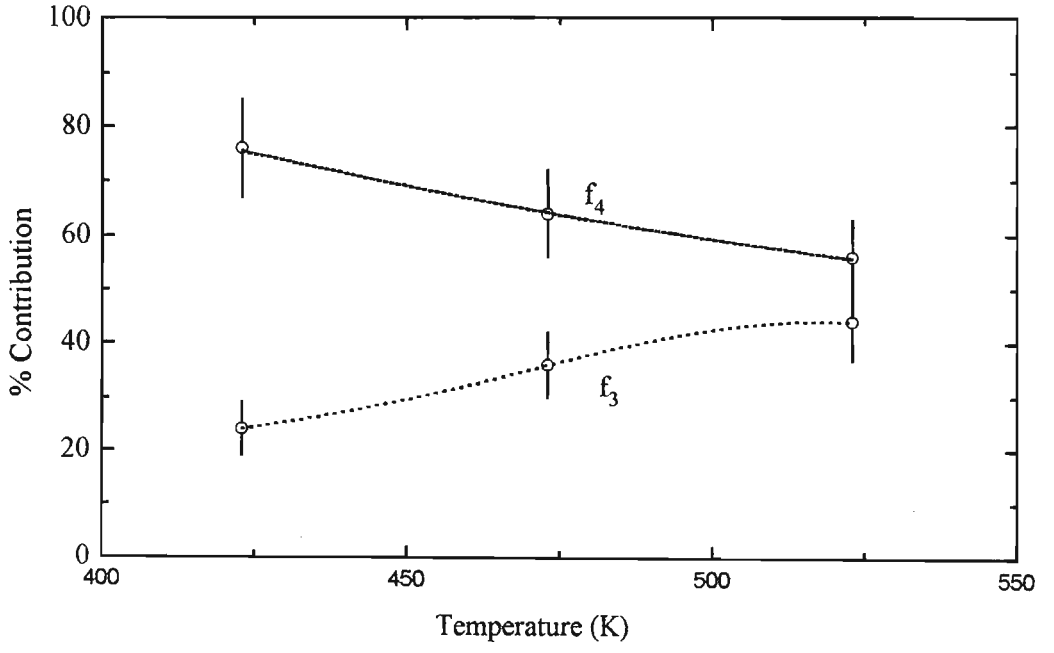

Fig. 4.9(b). Fractions observed in TDPAC spectra as a function of measuring temperature for VO_2

V: DISCUSSION

5.1 Fe SITES IN DOPED V_2O_5

V_2O_5 has an orthorhombic crystal structure with space group Pmmn, the lattice parameters of which are listed in Table 3.6 (a). In each unit cell, there are two pairs of heavily distorted VO_6 octahedra [JEN73, BUT89], and in each pair, the octahedra are mirror images of each other. An octahedron is illustrated in Fig. 5.1. Each unit cell has 4 vanadium ions and 24 oxygen ions.

The one possible site for Fe introduced into this lattice is the substitutional site of the V ion. However, the Fe ions are in 3+ oxidation states, whereas the V ions are in 5+ oxidation states. In order to maintain the electrical neutrality of the crystal, when the Fe^{3+} ions are introduced at the substitutional sites, then additional Fe^{3+} must also be introduced at interstitial sites, i.e. for every three Fe^{3+} ions at substitutional sites, there must be two Fe^{3+} ions at interstitial sites.

There are two possible interstitial sites for Fe^{3+} in the V_2O_5 lattice. One site is at the centre of a trigonal prism, where there are oxygen ions at each vertex of the prism [JEN73, ABD69]. This prism is located between layers perpendicular to the b axis of the lattice and is shown as (I) in Fig. 5.2. The distance from the centre of gravity of this prism to each of the oxygen atoms is approximately 2,51Å.

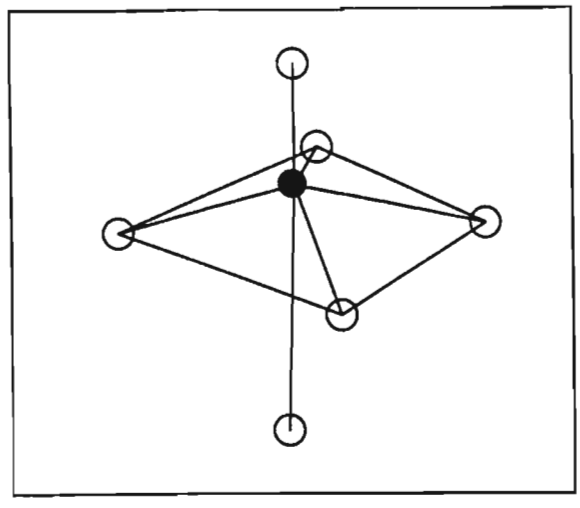

Fig. 5.1. Octahedron of V_2O_5.

The second site is inside that of an improper tetrahedron, with four oxygen ions at each vertex, shown as (II) in Fig. 5.2 [JEN73, ABD69]. The distance from the centre of the tetrahedron to each neighbouring O ion is approximately 1,95 Å. With the radius of the Fe ion being 0,64 Å and the radius of the O ion being 1,4 Å, using the Pauling rule, the improper tetrahedron is a more likely interstitial site than the trigonal prism [JEN73].

It is therefore expected that there will be two sites possible for Fe^{3+} in the V_2O_5 lattice, one at the substitutional sites, and the other at the interstitial site at the centre of the improper tetrahedron.

In Fig. 5.1, the shortest V-O bond has a covalent double bond character, the longest V-O bond has an ionic character, with the remaining four bonds of covalent single bond character. It is therefore expected that Fe at a substitutional site will have a greater covalent nature than Fe at an interstitial site. Since the probability of the *s* electrons being found at the nucleus is smaller for probe atoms with ionic bonds than for probe atoms with covalent

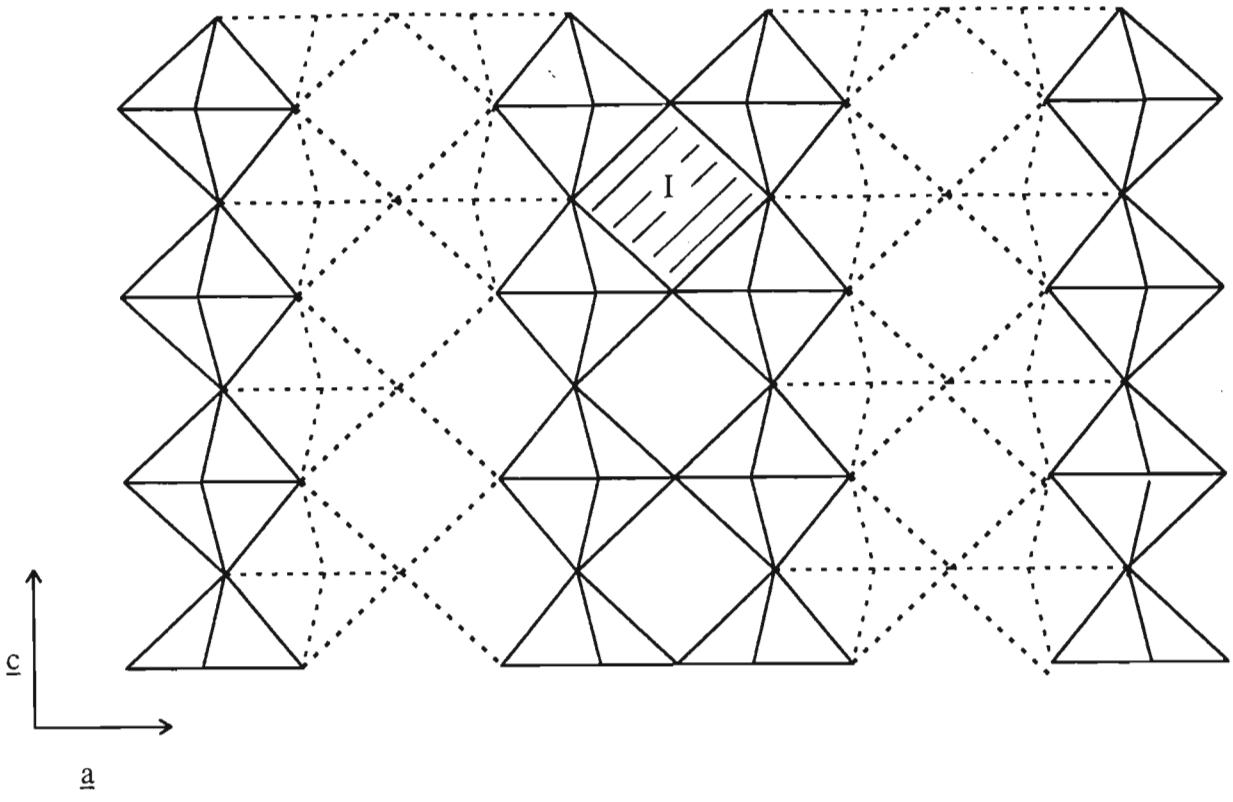

Fig 5.2(a). Lattice reprensation of V_2O_5 in the ac lattice plane. Only the oxygen positions are shown

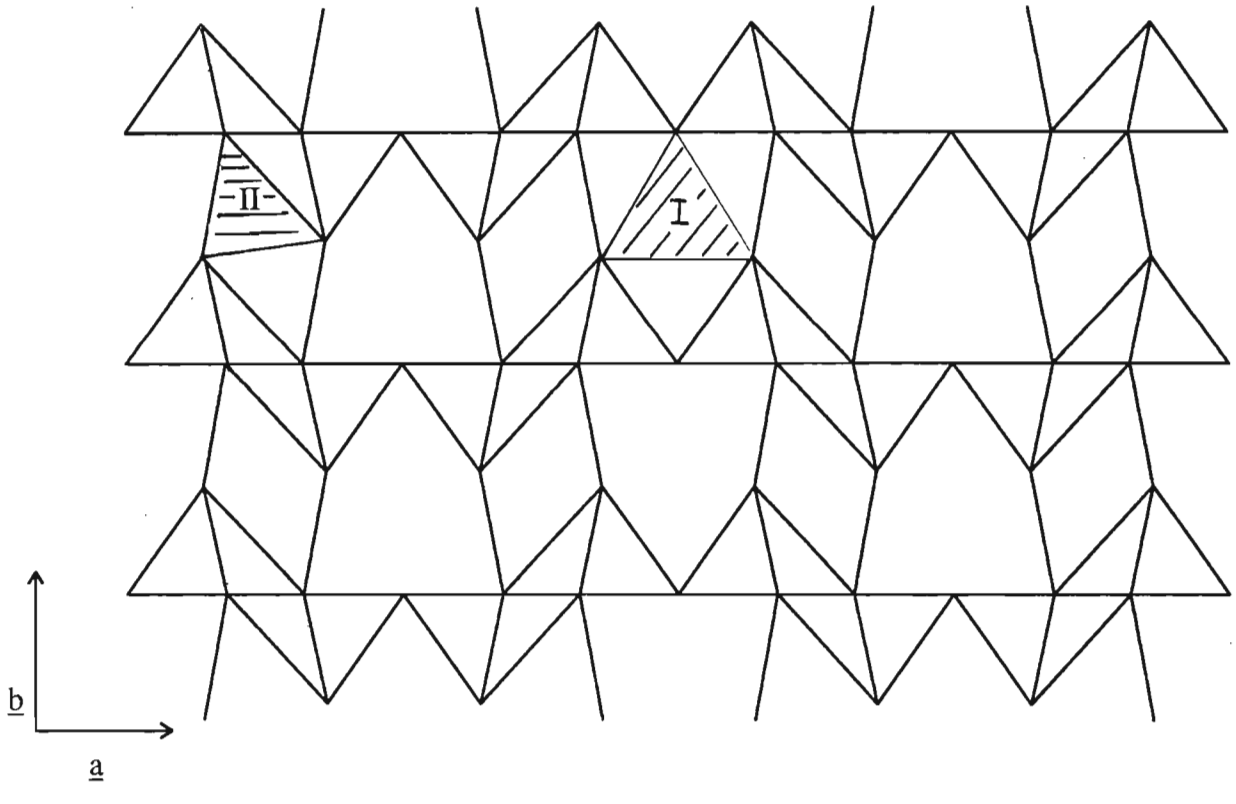

Fig 5.2(b). Lattice reprensation of V_2O_5 in the ab lattice plane. Only the oxygen positions are shown. I is the trigonal prism and II is the improper tetrahedron.

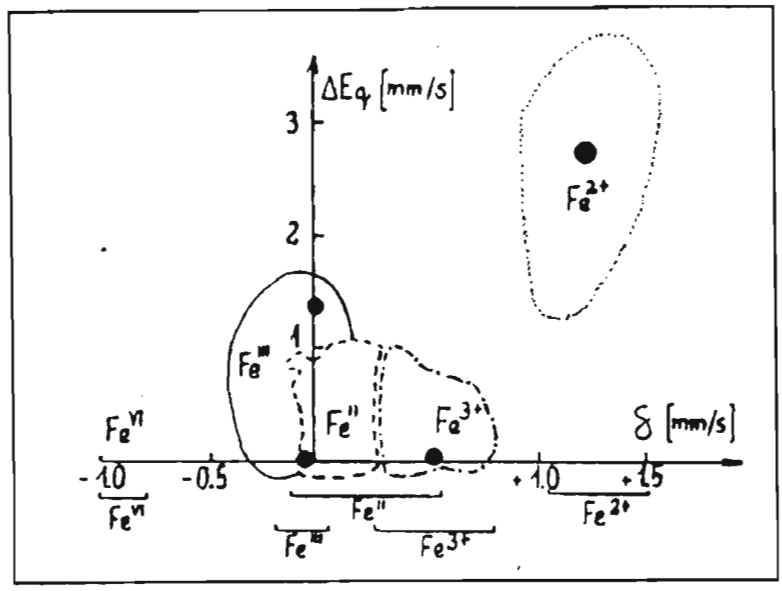

Fig. 5.3. The Duncan-Golding δ - ΔE_Q correlation diagram for Fe in various valency and spin states [DUN65]

bonds, then from Eqn. 2.8, this means that the isomer shifts of probes at ionic sites will be larger than the isomer shifts of probes at covalent sites. Based on this, we can therefore assign doublet c of the Mössbauer spectra to Fe at interstitial sites, and doublet d to Fe at substitutional sites.

In addition, the percentage contribution to the Mössbauer resonance of probes at substitutional sites should be greater than those of probes at the interstitial sites, because the ratio of the Fe^{3+} ions at substitutional sites to that at interstitial sites is 3/2. This is indeed what has been observed, as is shown in Fig. 3.7 (c) and (d).

In further support of this assignment, we can assess whether the oxidation state of Fe of 3+ is in agreement with the Duncan-Golding correlation diagram, shown in Fig. 5.3 [DUN65]. Using the parameters listed in Table 3.2(a) and (b) for the isomer shifts and quadrupole

splittings of the doublets c and d, we observe that they correspond to 3+ oxidation states on the Duncan-Golding correlation diagram.

5.2 Fe SITES IN Θ-VOB

At room temperature, the crystal structure of the Θ-VOB phase is monoclinic and is closely related to that of V_6O_{13}, [BAR85]. The unit cell contains 6 formula units $Fe_xV_2O_5$ where x lies between 0,33 and 0,66.

In order to understand how the introduction of Fe into this structure arises, it is advisable to look at a few unit cells in the a-c plane at positions 0 and 1/2 along the b direction, as shown in Fig. 5.4(a) and (b) [GAL67]. From this figure, it is clear that there are 12 V ions, 30 O ions, and 4 Fe ions possible in each unit cell. Written as $Fe_xV_2O_5$, we then observe that x can have a maximum value of 0,66.

In order for the Fe ions to enter into this lattice, the V^{5+} ions must change to the V^{4+} oxidation states in order to maintain charge neutrality:

$$\text{i.e. } Fe_{metal} + 3V^{5+} \rightarrow (Fe^{3+} + 3V^{4+})$$

If all the Fe sites shown in Fig. 5.4 were occupied, then all the V ions would have the 4+ oxidation state.

These sites for the Fe ions (holes) are more clearly displayed as "tunnels" by stacking the a-c planes on each other, as shown in Fig. 5.5 [BAR85]. Here, the Fe ions are found in the tunnels A and B. From this figure, we note that in considering the local charge

compensation, no two adjacent holes along the tunnel can remain unoccupied by the Fe ions [BAR85]. This means that x cannot be less than 0,33.

When x = 0,33, there are two possible distributions, the "zig-zag" type, where the sites 1, 4, 5, 8, 9, 12, . . . are filled, and the "ladder" type, where the sites 1,2, 5, 6, 9, 10, . . . are filled [BAR85]. As x increases, the other vacant sites can also be filled, until x = 0,66, when all the sites are filled. However, it has been reported [GAL67] that the upper limit for x is 0,38. Beyond this value, the structure does not remain homogeneous.

Thus, in considering the manner in which the Fe ions can fill the holes present in the tunnels, it is realised that the Fe ions can have different nearest neighbour surroundings, leading to different electric fields gradients. As x increases from 0,33 to 0,38, the environment of the Fe ions should become less symmetric. From the values of the quadrupole splittings listed in Table 3.2(b), where the quadrupole splitting of doublet a is less than the quadrupole splitting of doublet b, it is therefore concluded that doublet a represents the site with the higher symmetry, i.e. x close to 0,33, and doublet b the site with the lower symmetry, i.e. x approaching 0,38.

To further support this assignment, we note, from Fig. 3.7, that the intensity contribution of a decreases faster than does doublet b as a function of the increasing Fe concentration in the melt. The solubility of Fe in θ-VOB will increase as the Fe concentration in the melt increases, i.e. x will approach 0,38. Thus, doublet a, which corresponds to the site of greater symmetry, should have a larger contribution at lower Fe concentrations in the melt,

whereas doublet b should have a larger contribution at higher Fe iron concentrations in the melt.

The isomer shifts, should on the other hand, be fairly constant since it is assumed that the Fe ions have ionic bonds and are in the 3+ oxidation state.

Our spectra are similar to the spectra observed by Korecki et al. [KOR82] and Bara et al. [BAR85], once we have removed the components corresponding to the Fe doped V_2O_5 phase, the Fe_2O_3 superparamagnetic phase, and the unknown phase. However, they were not able to assign the two components *a* and *b* as corresponding to the θ-VOB phase when *x* was close to 0,33 and 0,38, respectively

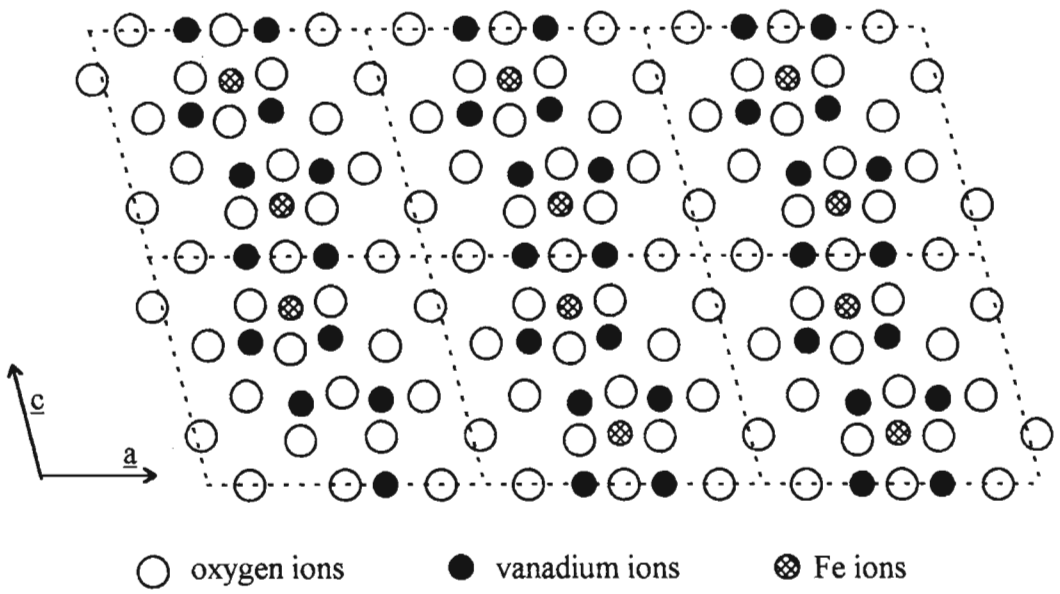

Fig. 5.4(a). Projection of the structure of $Fe_{0,33}V_2O_5$ onto the ac plane, at b = 0

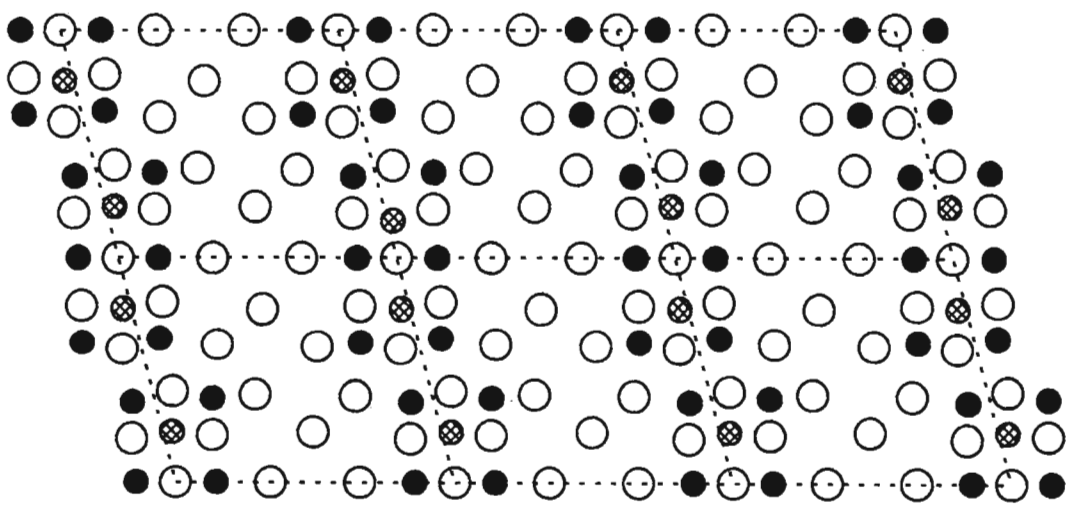

Fig 5.4(b). Projection of the structure of $Fe_{0,33}V_2O_5$ onto the ac plane, at b = ½

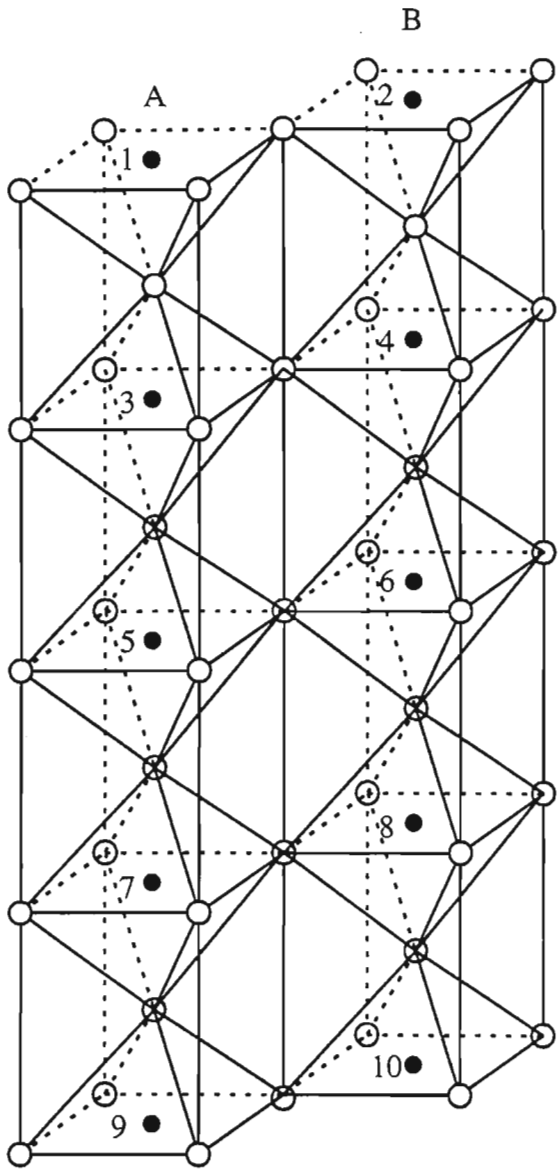

Fig 5.5. The tunnels A and B formed by the octahedrons in the crystal structure of θ-VOB

○ oxygen sites ● holes acceptable for Fe^{3+} sites

5.3. THE SEMICONDUCTING NATURE OF Fe DOPED V_2O_5 AND θ-VOB.

Semiconducting behaviour in both Fe-doped V_2O_5 and the θ-VOB phases have been reported previously [JAN73, BAR85]. Two possible mechanisms have been suggested for this behaviour, one using the mechanism of electron hopping between V^{4+} and V^{5+} oxidation states [KHA90], the other hopping of electrons between Fe^{3+} and Fe^{2+} ions [BAN87]. We examine our results in the light of these two models.

Just above the melting point of V_2O_5, the molecules of V_2O_5 dissociate according to the reaction [KHA90]

$$V_2O_5 \rightarrow V_2O_{5-x} + \tfrac{x}{2} O_2$$

where x increases with increasing temperature. This process in which the oxygen atoms are given off results in the lowering of the oxidation state of the vanadium ion from V^{5+} to V^{4+} or even to V^{3+}. Thus, if there were Fe ions present in the melt, when the melt cools, the θ-VOB phase could form easily since the creation of the θ-VOB phase necessarily requires the presence of V^{4+} ions. The Fe^{3+} ions, which enter in to the structure, occupies the holes in the tunnels shown in Fig. 5.5.

In the case of the Fe doped V_2O_5 phase, V^{4+} ions are not necessary for the introduction of the Fe^{3+} ions into the lattice, since the charge compensation is achieved when the Fe^{3+} ions occupy both substitutional and interstitial sites according to the ratio 3:2. However, since V^{4+} ions are created in the dissociation process, on cooling to create the Fe doped V_2O_5 phase, V^{4+} ions could also be present in the lattice. This would then imply that the ratio of Fe ions at lattice sites to Fe ions at interstitial sites will be larger than 3:2.

Thus both the Fe doped V_2O_5 phase and the θ-VOB phase can display semiconducting behaviour due to the presence of V^{4+} and V^{5+} ions in the lattices.

The electrical conductivity measurements (§3.2.7) have shown that the materials display a semiconducting nature. However, these results are the composite semiconducting behaviour of both the Fe doped V_2O_5 phase and the θ-VOB phase.

Both these phases are represented in the Mössbauer spectra as the doublets c and d, and a and b, respectively. Therefore, temperature dependent Mössbauer measurements would enable one to trace the behaviour of these components in terms of their semiconducting nature.

However, the temperature dependent Mössbauer measurements performed on the samples with 5%, 15% and 80% Fe concentration in the melt display only the usual second order Doppler shift of the isomer shift, with the quadrupole splittings remaining the same or decreasing slightly as shown in Fig. 3.9 (a) and (b).

There was no gradual or sudden appearance of any new components with increasing temperature, or changes in the intensities of any components with increasing temperature that would correlate with the mechanism for the semiconducting properties of V_2O_5 and the θ-VOB phase.

It has been suggested that hopping of electrons between Fe^{3+} and Fe^{2+} ions contributes to the observed semiconductivity [BAN87]. The Duncan-Golding curve (Fig. 5.3) gives us a good indication of the hyperfine parameters that a Fe^{2+} state in the vanadium oxides should have. Our spectra do not indicate any such states and hence rule out any subsequent transition between the Fe^{2+} to Fe^{3+} states with increasing temperature.

We are therefore led to the conclusion that the semiconducting properties are due solely to the hopping of electrons between the V^{5+} and V^{4+} ions and not to the Fe^{3+} and Fe^{2+} ions. No direct evidence of the presence of V^{4+} and V^{5+} ions is present in the Mössbauer spectra since the largest contribution to the hyperfine interaction arises from the immediate vicinity of the ^{57}Fe nucleus, which consists of the electrons of the Fe ion, and the nearest oxygen neighbours. The contribution of the V ions to this interaction are not as large, and this effect would not be observable due to the statistical nature of the spectra.

5.4 Cd SITES IN V_2O_5

In order to assign the components observed in the TDPAC measurements to the possible sites of ^{111}Cd in the V_2O_5 phase, it is first necessary to discuss the effect of implantation of ^{111}In into the sample and subsequent annealing of the sample.

Implantation of a foreign ion into a material will cause radiation damage. This will manifest itself as lattice distortions, creation of vacancies, etc. Thus, if the hyperfine probes are at lattice sites, the various probes will experience hyperfine fields which are not identical, with the result that the observed composite interaction of these probes would

having a wide distribution. As one anneals the sample, the radiation damage will be removed, and the lattice will regain its order. This means then that the various hyperfine fields experienced by the probes at one crystallographic site will then becomes more similar, until all the radiation damage is removed, at which point the hyperfine fields can be considered to be uniform within the limits of the experimental accuracy.

This is indeed the case for the sample annealed in vacuum. As the sample is annealed the width δ of the component f_1 is seen to decrease, and this is an indication that the cadmium ion is at a lattice site, as shown in Table 4.1(a).

We further note that component f_2, which has a much wider distribution, decreases in its percentage contribution as the annealing temperature increases, as shown in Fig 4.5 (a). It therefore seems reasonable to assume that component f_2 is associated with sites in the crystal where the radiation damage is great. As the sample is annealed, and the radiation damage is removed, causing a transition to the substitutional, high symmetry site, with the population of the f_2 site therefore decreasing. The Cd ions which were at these sites are then manifested as an increase in the intensity of the f_1 component.

The component f_1 is also observed for the sample in which the annealing was conducted in air, as listed in Table 4.1(b). Although its distribution is twice that observed for the sample annealed in vacuum, it is still much smaller than the distribution of component f_3 observed in this second sample. We can therefore assign component f_1 as the substitutional site in

the V_2O_5 lattice, and the component f_3 as the site due to the radiation damage, since the hyperfine parameters of f_3 are similar to those of f_2.

In addition to these components, the further component f_4 is also observed in the second sample. Its percentage contribution is much smaller than f_1 and f_3, as listed in Table. 4.1b, but its distribution is of the same order as component f_1. A possible explanation for the appearance of this component is that of an interstitial site in the V_2O_5 lattice.

Finally, we note that because the implantation dose of ^{111}In is much smaller than the concentration of the Fe in the Mössbauer effect measurements, the appearance of a phase similar to the θ-VOB seems unlikely.

5.5 Cd SITES IN VO_2

At the temperature T_t = 340 K, VO_2 shows a semiconductor-metal transition [MOR59].
In the high temperature region, the structure is rutile (tetragonal) but in the low temperature region, 3 phases can exist, two of which are monoclinic, M1 and M2, and one triclinic, T, [KOS67, PEB83, WIE78, ADL67 and PAU70].

Mössbauer studies have indicated two sites (doublets) in the low temperature phase and one site (a broad singlet) in the high temperature phase [KOS67].

Since the rutile phase is tetragonal, it is expected that the hyperfine field will show a greater symmetry in the tetragonal phase (high temperature phase) than in the monoclinic/triclinic phases (room temperature phases).

In the present study, for the first sample of VO_2, in which annealing was done in vacuum, and TDPAC measurements performed at room temperature, a distinct component f_1 appears, together with a broader component f_2. As the annealing temperature increases, the intensity contribution of component f_1 increases, with the corresponding decrease in the intensity of f_2. As in the case for ^{111}In implanted into V_2O_5, it is also expected that implantation of ^{111}In into VO_2 would also create radiation damage, and with annealing, this radiation damage will be removed.

We can therefore assign f_1 as substitutional Cd in the VO_2 lattice when the material is at room temperature and f_2 as the component associated with radiation damage.

For the second sample of VO_2 implanted with ^{111}In, the measurements were taken at temperatures of 423 K to 673 K in vacuum of 10^{-2} mBar. We can therefore treat these measurements as the simultaneous annealing and acquiring of TDPAC spectra at temperatures above the transition temperature.

By considering the widths of the components observed (Table 4.2 (b)) we can then assign the component f_3 to a substitutional lattice site in the tetragonal VO_2 structure, and the component f_4 as due to the effects of radiation damage.

Thus f_1 is a site in the low temperature phase and f_3 is a site in the rutile phase. We note that f_3 has a lower asymmetry parameter than f_1 which is in accordance with the symmetry comparisons of the crystallographic structure in these two phases.

These results compare well with other similar measurements. For the case of CuO [BAR88], where a cation site is in a monoclinic phase, the asymmetry parameter has a value of 0,41(1) and is in good agreement with f_1. The asymmetry parameter of f_3 is also similar to the other known cases of ^{111}Cd in rutile crystals [REN91, WEN92].

VI: CONCLUSION

The aim of this project was to use radioactive probes ^{111}In and ^{57}Fe to study the lattice location of the probes in V_2O_5, θ-VOB and VO_2, and to investigate the mechanism responsible for the observed semi-conducting phase in Fe-doped V_2O_5 and θ-VOB. Our complementary measurements using the hyperfine techniques of TDPAD (on In - doped samples) and Mössbauer Spectroscopy (on Fe - doped samples) and XRD lead to the following conclusions.

In the TDPAC measurements for V_2O_5, a component f_1 is observed with ν_Q = 89.8(5) MHz and η = 0,62(1), which may be assigned to susbstitutional Cd in the V_2O_5 lattice. Other frequencies are also observed, which are due to probe atoms at radiation damaged environments.

In VO_2, the TDPAC spectra are characterised by two components f_1 and f_3, with parameters ν_Q = 43.0(7) MHz and η = 0,39(4), and ν_Q = 89.1(1) MHz and η = 0,20(1), respectively. The f_1 component corresponds to a monoclinic or triclinic phase below the transition temperature of VO_2 and the f_3 component to the tetragonal phase above the transition temperature. The site in the tetragonal phase displays a higher symmetry than the site in the low temperature phase.

The Mössbauer spectra indicate that there are two sites present in the Fe doped V_2O_5 phase, one of which is a substitutional site, and the other an interstitial site. The interstitial site shows

a greater ionicity than the substitutional sites. However, both sites display similar symmetry in the crystallographic environment.

In the θ-VOB phase (Fe concentration in the range x = 0,33 to 0,38), two Mössbauer resonance components are observed, corresponding to Fe in the same crystallographic configuration but with different electronic environments. The more symmetric component corresponds to the case when *x* is close to 0,33, and the less symmetric component corresponds to the case when *x* is close to 0,38.

In the process of creating the Fe doped V_2O_5 and θ-VOB phases, the superparamagnetic and ferromagnetic phases of α-Fe_2O_3 also appear. In addition, a further unknown crystallographic phase is also present.

Electrical conductivity measurements performed on the samples containing the Fe doped V_2O_5 and θ-VOB phases clearly indicate the semiconducting nature of these phases, in confirmation with earlier measurements. In pure V_2O_5, two activation energies were observed, viz. 0,321(5) eV below 458 K and 0,238(5) eV above 458 K. For the samples containing 5%, 15% and 80% Fe concentrations, the activation energies were observed to be 0,299(5) eV, 0,314(5) eV and 0,758(5) eV respectively.

While two possible mechanisms for the semi-conducting behaviour have been proposed, viz, electron hopping between V^{4+} and V^{5+} sites or Fe^{2+} and Fe^{3+} sites, our results show no evidence of the Fe^{2+} phase, and hence lead to the conclusion that the semiconducting behaviour is due solely to the hopping of electrons between the V^{4+} and V^{5+} ions.

REFERENCES

[ABD69] A. A. Abdullaev, et.al, Soviet Phys. Solid State, 10 (1969) 2957

[ADL67] D. Adler, J. Feinlieb, H. Brooks and W. Paul, Phys. Rev., 155 (1967) 155

[BAN87] T. K. Bansal, S. Bansal and R. G. Mendiratta, Hyp. Int., 35 (1987) 863

[BAR74] M. Baran and A. Polaczek, Phys.Stat.Sol (A), 25 (1974) K13

[BAR85] J. J. Bara, et al., J. Sol. State Chem., 58 (1985) 143

[BAR88] A. Bartos, W. Bolse, K. P. Lieb and M. Uhrmacher, Phys. Lett. A, 130 (1998) 177

[BAR93] A. Bartos, K. Schemmerling, T. Wenzel and M. Uhrmacher, Nucl. Instr. Meth., A 330 (1993) 132.

[BOL87] W. Bolse, M. Uhrmacher and K. P. Lieb, Physical Review B, 36 (1987) 1818

[BOR70] Borisenko et al., Dokl. Akad. Nauk SSSR, 193 (1970) 135, listed in Mineral Powder Diffraction File Data Book, JCPDS (1986), 1070.

[BOS84] H. Bosch, et al., J. Chem. Soc., Faraday Trans. 1, 80 (1984) 2479

[BRO86] Brown, X-ray Indentification and Crystal Structures in Clay, listed in Mineral Powder Diffraction File Data Book, JCPDS (1986) 693

[BUR76] E. Burzo and L. Stansecu, Solid State Comm, 20 (1976) 653

[BUR78] E. Burzo and L. Stansecu L, Phys.Stat.Sol., (A) 46 (1978) K163

[BYS50] A. Bryström, K. A. Wilhelmi and O. Brotzen, Acta Chem. Scand., 4 (1950) 1119

[CAV88] F. Cavani, et al., J. Chem. Soc., Faraday Trans. 1, 84 (1988) 237

[CRC72] Handbook of Chemistry and Physics, CRC Press, Ohio, USA (1972) D60

[DER70] P. D. Dernier and M. Marezio, Phys. Rev. B, 2 (1970) 3771

[DUN65] F. J. Duncan and R. M. Golding, Quarterly Review, 19 (1965) 36

[FAB90] P. B. Fabritchnyi, et al., Sol.State Comm., 74 (1990) 337

[FEI67] J. Feinleib and W. Paul, Phys. Rev, 155 (1967) 155

[FER65] A. J. Ferguson, Angular Correlation Methods in Gamma Ray Spectroscopy, North-Holland, Amsterdam (1965)

[FRA65] H. Frauenfelder and R. M. Steffen (1965) in Alpha-, Beta-, and Gamma-Ray Spectroscopy, 2, (ed. K.Siegbahn), 997, North Holland, Amsterdam

[GAL67] J. Galy et al, Bulletin de la Societe Chimique, 1 (1967) 227

[GIL75] R. D. Gill, Gamma Ray Angular Correlations, Academic Press, London (1975)

[GON86] U. Gonser, Topics in Current Physics - Microscopic Methods in Metals, Springer, Berlin (1986)

[GRO60] G. Grossman, et al., Z. Anorg. Allgem. Chem., 305 (1960) 121

[JAN73] K. Jansen and G. Sperlich, Phys.Stat.Sol. (B), 55 (1973) 495

[JAN82] C. Janot, et al., J. Phys. F: Met. Phys., 12 (1982) 47

[JON65] E. D. Jones, Phys. Rev., 137 (1965) A978

[KAJ73] J. Kajfosz, Institute of Nuclear Physics (Cracow), Report No. 858/PM (1975)

[KAW64]T. Kawakubo and T. Nakagawa, J. Phys. Soc. Japan, 19 (1964) 517

[KHA90] G. A. Khan and C. A. Hogarth, J of Mat. Science, 25 (1990) 5014

[KKO67] K. Kosuge, J. Phys. Chem. Solids, 28 (1967) 1613

[KOR82] J. Korecki et al. Nuclear Instruments and Methods, 199 (1982) 209

[KOS67] K. Kosuge, J. Phys. Soc. of Japan, 22 (1967) 551

[KRU76] S. Krupicka, Fizika Ferritov, 2, Mir.Publ., Moscow (1976) 422

[LAS86] H. Lass, et al., Phys. Stat. Sol. (a), 93 (1986) 233

[MIN86] W. F. McClune, Ed. in Chief, Mineral Powder Diffraction File, JCPDS, Swartmore, USA (1986)

[MOO70]R. M. Moon, J. Appl. Phys., 41 (1970) 883

[MOO91]B. Moody, Comparative Inorganic Chemistry, 3rd Ed., Edward Arnold, London, (1991)

[MOR59] F. J. Morin, Phys.Rev.Lett., 3 (1959) 34

[MOR87] K. Mori, et al., J. Chem. Soc., Faraday Trans. 1, 83 (1987) 3303

[MOS58] R. L. Mössbauer, Z. Phys., 151 (1958) 124

[MUL80] W. Muller, MOSFUN, University of North Carolina, USA (1980)

[NII91] Y. Niida, et al., Hyperfine Interactions, 69 (1991) 631

[OKI69] H. Okinaka, et al., J. Phys. Soc. Japan, 27 (1969) 1366, 28 (1970) 798, 29 (1970) 245

[OKI70] H. Okinaka, et al., Phys. Lett, 33A (1970) 370

[OKI72] H. Okinaka, et al., J. Phys. Soc. Japan, 32 (1972) 1148

[PAU70] W. Paul, Mater. Res. Bull., 5 (1970) 691

[PEB83] J. Pebler, Phys. Stat. Sol. (a), 78 (1983) 589

[PEK80] M. Pekala and A. Polaczek, Phys.Stat.Sol. (A), 58 (1980) 533

[PRA67] S. Prakash, Advanced Chemistry of Rare Earth Elements, Chem.Publ.Co., New York (1967)

[REN91] M. Renteria, et al., J.Phys.: Condens. Matter, 3 (1991) 3625

[ROO80] F. Roozeboom, et al., J. Phys. Chem., 84 (1980) 2783

[RUD58] W. G. Rudorff, et al., Z. Anorg. Allgem. Chem., 297 (1958) 1

[SCH96] G. Schatz and A. Weidinger, Nuclear Condensed Matter Physics, John Wiley and Sons, New York (1996)

[SHI90] Y. Shimizu, et al, Japanese J. of Appl. Phys., 29 (1990) L1708

[UHR85] M. Uhrmacher, K. Pampus, F. J. Bergmeister, D. Purschke and K. P. Lieb, Nucl. Instr. Meth. B, 9 (1985) 234

[UME65] J. Umeda, et al., J. Chem. Phys., 42 (1965) 1458

[WAR60] E. P.Warekois, J. Appl. Phys., 31 (1960) 346S

[WEN92] T. Wenzel, et al., Ann. Physik, 1(1992) 155

[WIE78] E. Wieser, et al., Phys. Stat. Sol. (a), 45 (1978) 123

APPENDIX A

Hyperfine Interactions 80 (1993) 965–970

The electric field gradient at ^{111}Cd in vanadium oxides ☆

V. Naicker [1], A. Bartos, K.P. Lieb, M. Uhrmacher, T. Wenzel and D. Wiarda

II. Physikalisches Institut der Universität Göttingen, Bunsenstrasse 7–9, D-37073 Göttingen, Germany

The electric field gradient (efg) of ^{111}Cd in polycrystalline V_2O_5 was studied using perturbed angular correlation (PAC) spectroscopy, with the ^{111}In activity ion-implanted at 400 keV. Between the individual steps of an isochronal annealing program, a distinct efg ($\nu_{Q1} = 88.1(3)$ MHz, $\eta_1 = 0.62(2)$) was recorded the contribution of which increased with annealing temperature up to 74% at 870 K. Corresponding X-ray analysis of inactive V_2O_5 samples, which underwent the same annealing treatment, proved that the sample always stayed as V_2O_5. Since V_2O_5 has only one equivalent cation site, it is concluded that this efg belongs to ^{111}Cd at this site. Oxidation of a vanadium foil at $T = 675$ and 800 K at $p_{O_2} = 200$ mbar also yielded this efg. From PAC measurements in VO_2, two well-defined efg's were found above and below the metal–semiconductor transition at 340 K, which are tentatively attributed to the monoclinic and the tetragonal phase.

1. Introduction

The oxides of vanadium exhibit a wide variety of phases, ranging from metallic vanadium to the thermally most stable vanadium pentoxide V_2O_5. Earlier PAC studies with ^{111}In/^{111}Cd probes carried out on a vanadium foil undergoing oxidation yielded several electric field gradients (efg) [1]. However, these could not be assigned to any of the several oxide phases present in the sample as verified by X-ray diffraction. PAC measurements on metallic vanadium yielded pure electric quadrupole interaction, while antiferromagnetic, insulating V_2O_3 exhibited combined magnetic dipole and electric quadrupole interaction [2]. In this paper we report on PAC studies involving the non-magnetic oxides V_2O_5 and VO_2, with the focus placed on V_2O_5.

☆ Supported by Deutsche Forschungsgemeinschaft and DAAD.

[1] On leave from the University of Durban-Westville, South Africa.

2. Experimental

The ^{111}In PAC probe nuclei were ion-implanted at 400 keV using the Göttingen heavy ion implanter IONAS [3]. Before implantation, the oxide targets were prepared by pressing the commercially obtained oxide powders onto thin metallic backings. After implantation and during the annealing procedures and PAC measurements the oxides were enclosed in thin metal packets. For the V_2O_5 samples, Ag foils were used for backings and packets in all measurements; for VO_2 samples, Pt and Pd foils were used. To remove radiation damage caused during ^{111}In implantation, the samples were isochronally annealed at T_a, either at a total pressure of 10^{-5} mbar or in air. PAC measurements were carried out at room temperature (T_m = RT) and in air. One set of PAC measurements on a VO_2 sample was carried out at 420 K $\leqslant T_m \leqslant$ 520 K and at 10^{-2} mbar. The PAC spectra were recorded using a set-up of four NaI(Tl) detectors in 90° geometry, which allowed to record all possible twelve time spectra through an Atari PC data collection system [4]. The data were fitted using the standard formulae for static quadrupole hyperfine interaction (hfi) in which up to three efg fractions f_i were considered, each characterized by its quadrupole frequency ν_{Qi}, asymmetry parameter η_i and distribution width δ_i.

Inactive V_2O_5 and VO_2 powders were annealed under similar conditions as those in the PAC measurements. X-ray powder diffraction analyses with Cu K_α-radiation were subsequently conducted. The X-ray spectra were compared with the JCPDS data files [5].

3. Results and discussion

Between isochronal annealing steps of *V_2O_5 in vacuum* with t_a = 60 min and the annealing temperature T_a increasing up to 870 K, fraction f_1 (ν_{Q1} = 88.1(3) MHz, η_1 = 0.62(2) and δ_1 = 5.6(5) MHz) was observed to increase up to 74%. Correspondingly, a broadly distributed fraction f_2 (ν_{Q2} = 221(2) MHz, $\eta_2 \leqslant 0.1$ and δ_2 ranging from 25 to 45 MHz) was observed to decrease with increasing T_a. The evolution of both fractions as a function of T_a is shown in fig. 1. The $R(t)$ functions obtained after T_a = 670 and 870 K are shown in fig. 2, together with their Fourier spectra. Fig. 3 illustrates the X-ray spectrum taken after T_a = 870 K, together with the spectrum of the 9-387 JCPDS data file. All X-ray analyses proved that the samples stayed V_2O_5 during the full cycle.

During a similar annealing cycle of *V_2O_5 in air* and with t_a = 30 min, the hyperfine interaction f_1 was again observed, having a slightly larger ν_{Q1} of 91.4(6) MHz, but identical η_1 = 0.61(2). Its contribution f_1 decreased from 46 to 25% with increasing T_a. A small fraction of $\approx$ 10% with ν_Q = 224(3) MHz and $\eta \approx 0$ was identified, the efg parameters of which closely resemble those of fraction f_2 observed in the vacuum annealing, but have a smaller width of δ_2 = 10 MHz. A new broad efg fraction f_3 (ν_{Q3} = 265 MHz, η_3 = 0 and δ_3 ranging between 51 and

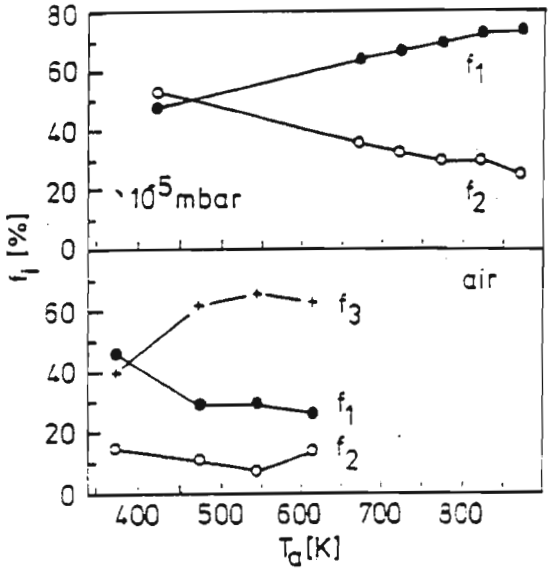

Fig. 1. Fractions f_1 (●), f_2 (○) and f_3 (+) plotted versus the annealing temperature T_a in air and in vacuum (10^{-5} mbar).

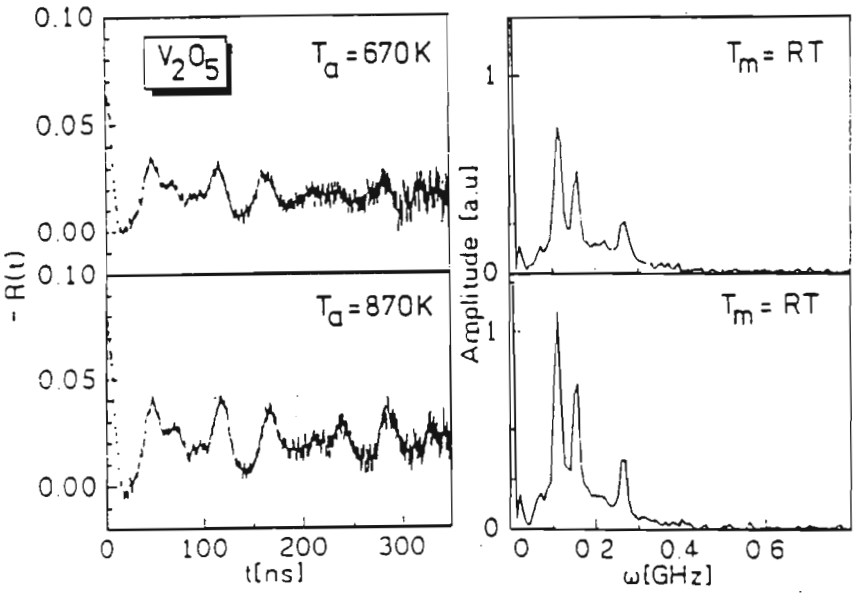

Fig. 2. Room temperature PAC spectra of ^{111}In in V_2O_5 after annealing at the temperature shown, together with their Fourier spectra.

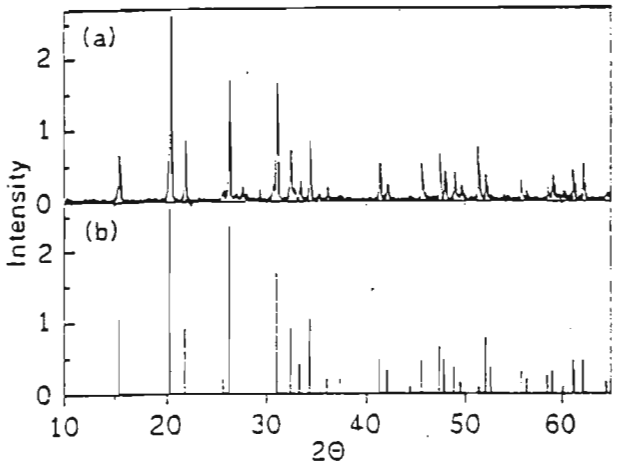

Fig. 3. X-ray spectrum of V_2O_5 after annealing at 870 K (a), in comparison with the JCPDS files (b).

97 MHz) was also observed ranging between 40 and 66%. The evolution of the three fractions f_1–f_3 as functions of T_a is shown in fig. 1.

The oxide V_2O_5 is orthorhombic with space group Pmnm [5]. There exists only one cation site with six nearest oxygen neighbours arranged as shown in fig. 4a; fig. 4b indicates how this unit develops into the crystal structure. The shortest V–O bond (1.543 Å) is reported to be of covalent double-bond character, the longest V–O bond (2.828 Å) of ionic bond character and the remaining four V–O bonds of covalent single-bond character [5]. Due to the high asymmetry of the oxygen environment, the efg at the vanadium site would be expected to have a large asymmetry parameter η, in the limit of the ionic point charge model (pcm). However,

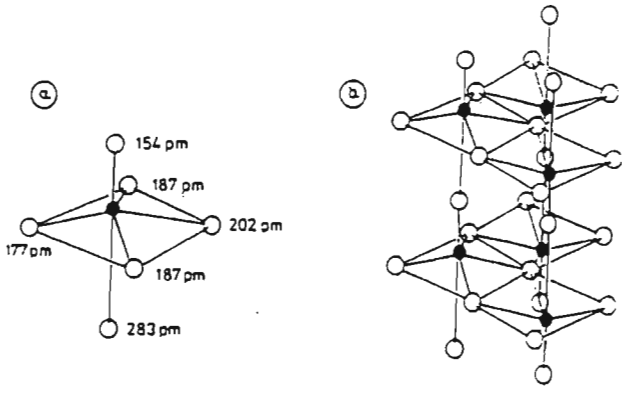

Fig. 4. (a) Structure model of the V_2O_5 molecule; (b) the development of (a) to form the crystal structure.

pcm calculations will not yield satisfactory efg values due to the different covalencies and lengths of the V–O bonds. A recent survey of experimental efg's for ^{111}Cd in many metal oxides, indeed indicated the pcm to be valid for bond lengths exceeding 2.1 Å [6]; shorter bond lengths lead to large variations of the efg.

Fraction f_1 which increases with the annealing temperature T_a and the decreasing width δ_1 shows the characteristics of a probe nucleus occupying a substitutional site in the lattice as verified in many metal oxides. Both findings are a consequence of annealing of radiation damage and point to a well-defined lattice location. A PAC measurement taken after a two-step 30 min oxidation treatment of a vanadium foil at 675 and 800 K and at $p_{O_2} = 200$ mbar yielded the same efg parameters. Comparing this with the results of the analyses of the V_2O_5 powder diffraction data, it is suggested that f_1 is related to ^{111}Cd at a substitutional defect-free cation site in V_2O_5. In the annealing treatment in air, this efg was again observed.

Finally we report on PAC measurements on *VO_2 in vacuum*. At the temperature $T_t = 340$ K, VO_2 shows a metal–semiconductor transition and its lattice structure changes from monoclinic to rutile [7]. In the latter structure only one cation site exists. Recent PAC experiments on SnO_2 [8] and TiO_2 [9] revealed only one efg for each compound: $\nu_Q(SnO_2) = 117(1)$ MHz/$\eta = 0.18(2)$ and $\nu_Q(TiO_2) = 105(1)$ MHz/$\eta = 0.18(1)$. Below T_t, different monoclinic phases exist with similar oxygen coordinations, mainly determined by the non-stoichiometry of the compound. In fact, X-ray analyses at RT showed that the VO_2 powder was composed of the following monoclinic phases listed in the JCPDS data files: 9-142, 33-1440, 33-1441 and 19-1398.

During an isochronal annealing cycle at 10^{-5} mbar, a distinct fraction $f_4 = 44\%$ was observed after $T_a = 920$ K which increased to 71% after $T_a = 995$ K. The efg parameters measured at RT and 10^{-5} mbar are $\nu_{Q4} = 42.9(7)$ MHz, $\eta_4 = 0.38(4)$, $\delta_4 = 3.4(6)$ MHz. A second sample was not annealed after the ^{111}In implantation, but measured at elevated temperatures and 10^{-2} mbar. At $T_m = 420$ K, a new well-defined fraction with $f_5 = 25\%$ was found which increased to 44% at $T_m = 520$ K. Its hfi parameters are $\nu_{Q5} = 89.2(2)$ MHz, $\eta_5 = 0.20(2)$ MHz and $\delta_5 = 2.8(4)$ MHz. Although we did not see the metal–semiconductor transition occurring at the same VO_2 sample, it seems plausible to correlate ν_{Q4} with monoclinic VO_2 and ν_{Q5} with the rutile structure. The efg-strength and the asymmetry parameter are similar to the other cases known of ^{111}In/^{111}Cd in a rutile crystal [8,9]. A higher asymmetry parameter can be expected at a cation site in a monoclinic oxide and, again a nice agreement is found with $\eta(CuO) = 0.42(1)$ [10]. In early PAC experiments with the ^{181}Hf/^{181}Ta probe, the metal–semiconductor transition in VO_2 was investigated [11]. Two different non-axial efg's were observed and characterized by their frequencies ω_1(monoclinic) = 480(30) MHz and ω_1(rutile) = 620(40) MHz. For comparison with the present results we calculated the ratio $R = \omega_1(^{181}\text{Ta})/\omega_1(^{111}\text{Cd})$. The values R(monoclinic) = 10.4(7) and R(rutile) = 7.1(4) are within the range of values found for these two PAC probes in different metals [12].

Acknowledgement

It is a pleasure to thank Dr. L. Ziegeler for preparing several vanadium oxide samples and D. Purschke for his help with the In implantations. The X-ray analyses were done by G. Brouwer and H. Engelmohr (Min. Petrol. Inst./Universität Göttingen). This work has been supported by Deutsche Forschungsgemeinschaft and Deutscher Akademischer Austauschdienst (VN).

References

[1] J. Kesten, private communication.
[2] M. Forker, H. Saitovitch and P.R. de Jesus Silva, J. Phys. C 17 (1984) 1055.
[3] M. Uhrmacher, K. Pampus, F.J. Bergmeister, D. Purschke and K.P. Lieb, Nucl. Instr. Meth. B 9 (1985) 234.
[4] A. Bartos, K. Schemmerling, T. Menzel and M. Uhrmacher, Nucl. Instr. Meth. A 330 (1993) 132.
[5] A. Byström, K.A. Wilhelmi and O. Brotzen, Acta Chem. Scand. 4 (1950) 1119.
[6] D. Wiarda, Doctoral Thesis, Göttingen, Germany (1992), unpublished;
D. Wiarda, M. Uhrmacher, A. Bartos and K.P. Lieb, J. Phys.: Condens. Matter 5 (1993) 4111.
[7] W. Paul, Mater. Res. Bull. 5 (1970) 691.
[8] M. Renteria, A.G. Bibiloni, M.S. Moreno, J. Desimoni, R.C. Mercader, A. Bartos, M. Uhrmacher and K.P. Lieb, J. Phys.: Condens. Matter 3 (1991) 3625.
[9] Th. Wenzel, A. Bartos, K.P. Lieb, M. Uhrmacher and D. Wiarda, Ann. Physik 1 (1992) 155.
[10] A. Bartos, W. Bolse, K.P. Lieb and M. Uhrmacher, Phys. Lett. A 130 (1988) 177.
[11] K. Lehnert, S. Unterricker and J. Hausbrand, Ann. Rep. ZfK Rossendorf (DDR), ZfK-295 (1975) 94.
[12] R. Vianden, Hyp. Int. 15/16 (1983) 1081.

APPENDIX B

A TEMPERATURE DEPENDENT MÖSSBAUER STUDY OF ^{57}Fe IN THE VANADIUM PENTOXIDE/ VANADIUM BRONZE OXIDE SYSTEMS.

V.V.Naicker and K.Bharuth-Ram
Department of Physics, University of Durban Westville, Durban 4000, South Africa

Our previous study involving V_2O_5 doped with various concentrations of Fe have shown that there are two sites present in the V_2O_5 lattice, and two sites present in the vanadium oxide bronze lattice. This study further investigates the behaviour of the hyperfine parameters of the ^{57}Fe ions at these sites as a function of temperature.

Temperature dependent Mössbauer spectra ranging from room temperature to 573 K were obtained on samples of V_2O_5 containing 5%, 15% and 80% Fe. The isomer shifts of the various components display the usual second order Doppler shift as a function of temperature, and no significant changes were observed in the magnitude of the quadrupole splittings. From the Duncan-Golding correlation diagram, the valence states of the Fe ions are found to be 3+.

No component was observed with increasing temperature which could be correlated with the population of Fe^{2+} states. It therefore seems probable that the semiconducting properties of vanadium pentoxide containing Fe are associated with electron hopping between V^{4+} - V^{5+} valence sites rather than Fe^{3+} - Fe^{2+} valence sites.

1. Introduction

The Fe-V_2O_5 system when created from a mixture of Fe powder and V_2O_5 powder is formed as a combination of two phases, the doped V_2O_5 phase in which the Fe impurity concentration is small and the vanadium oxide bronze (VOB) phase $Fe_xV_2O_5$ in which the Fe concentration x lies between 0,33 and 0,38. In a previous study [1], we have found that for the doped V_2O_5 phase the structure remains essentially the same as that of pure V_2O_5, and that there exists two Mössbauer sites, corresponding to a substitutional site and an interstitial site respectively. In the case of the VOB phase the structure is monoclinic and two further sites were observed in the Mössbauer spectra.

Both the phases have been reported to display a metal to insulator transition [2,3,4]. In particular for the VOB phase, the formation of V^{4+} ions are necessary in order to introduce the Fe into the V_2O_5 lattice. The V^{4+} ions together with the existing V^{5+} ions lead to the mechanism used to explain the electrical conductivity known as "electron hopping" [5] which can also be extended to the case of the doped vanadium pentoxide.

However it has also been suggested that the electrical conductivity could also arise from the hopping of electrons between Fe^{3+} and Fe^{2+} ions [5]. Since the Mössbauer parameters corresponding to Fe^{2+} states are normally quite different from those corresponding to Fe^{3+} states [6,7], if the conductivity is due to hopping between electrons of the Fe ions rather than the vanadium ions, then the appearance of Fe^{2+} states as a function of the temperature should be easily observed.

We have therefore conducted temperature dependent Mössbauer studies on three samples, each with different ratios of the doped V_2O_5 and VOB phases. These measurements were supplemented with electrical conductivity measurements in order to verify the semiconducting nature of the materials.

2. Experimental

Three samples, labelled as 1, 2 and 3, were produced by melting natural Fe powder and V_2O_5 powder in appropriate ratios using a solid state reaction [3,8]. After annealing at 473 K, Mössbauer spectra on each sample were collected, as a function of sample temperature, with a spectrometer operated in transmission mode with a ^{57}Co-Rh source. The sample was heated via a nichrome coil of 50Ω resistance attached to the sample base and the

temperature was monitored with chromel-alumel thermocouples. The data was analysed using a modification of the analysis code MOSFUN [9].

To conduct the electrical conductivity measurements, the powders were packed into a cylindrical vessel of diameter 2 mm and length 4 mm, the walls of which were made of electrically non conducting mica. Through the walls and into the chamber were passed two thin platinum wires. Electrical contact of the two wires was thus achieved only if conducting or semiconducting material was present in the vessel. The wires were externally connected to a digital multimeter and a stable power supply using copper leads. A 30V d.c. signal was supplied across the platinum wires for all the measurements.

3. Results and Discussion.

X-ray powder diffraction analysis indicated that in sample 1 the doped V_2O_5 phase was the dominant phase, in sample 2 the VOB phase was the dominant phase and in sample 3 both phases were of equal proportions.

Materials which display a semiconducting nature have the current I described by the equation $I \propto \exp\left(C/T\right)$ where C is a constant [2,7]. The results of the electrical conductivity measurements are shown in Fig. 1 from which the semiconducting nature of the materials is apparent. The measurements on pure V_2O_5 is also presented. These results are similar to the results of Bara et al.[8]. However, they had only measured the electrical conductivity of the single θ-VOB phase whereas the doped V_2O_5 phase is also present in our samples. Therefore, the semiconducting nature does not necessarily arise from a single θ-VOB phase in the samples but quite possibly from both the phases.

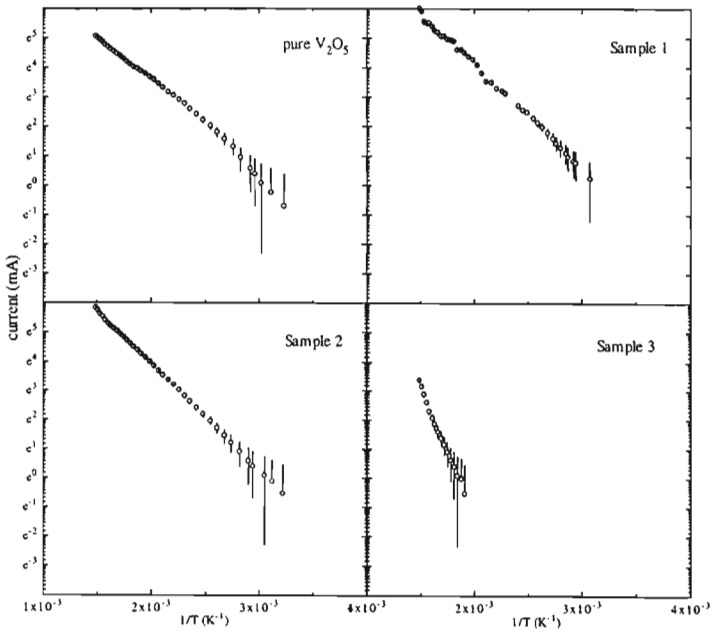

Fig 1. Electrical resistivity measurements for the various samples. In sample 1, the doped V_2O_5 phase is dominant, in sample 2, the VOB phase is dominant, and in sample 3 the doped V_2O_5 phase, the θ-VOB phase and the α-Fe_2O_3 phase have equal concentrations

The temperature dependent Mössbauer spectra of sample 2 is shown in Fig 2. Samples 1 and 3 displayed similar spectra. The isomer shifts of all the doublets for the three samples as a function of increasing temperature display the characteristic linear dependence due to the second order Doppler shift and the quadrupole splittings of all these doublets remain constant.

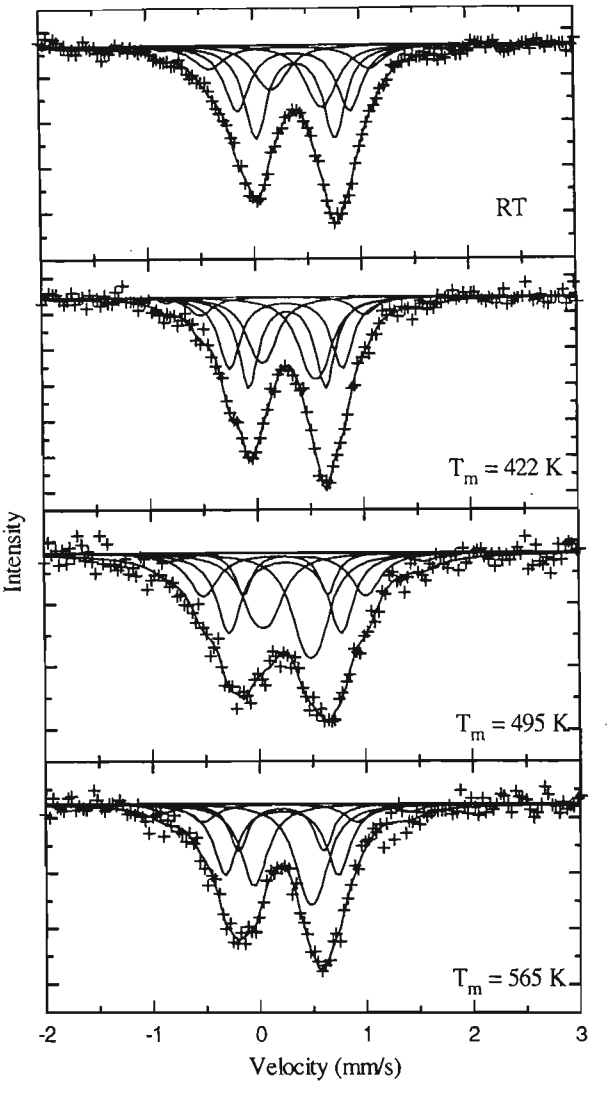

Fig 2. Temperature Dependent Mössbauer Spectra of Sample 2 in which the θ-VOB phase is dominant.

The Duncan-Golding correlation diagram [6] gives us a good indication of the Mössbauer parameters of a Fe^{2+} state and we have not observed any gradual or sudden appearance of such components with increasing temperature. Thus our spectra do not indicate any components which would imply the transition between the Fe^{2+} to Fe^{3+} states. We are therefore led to conclude that the semiconducting properties of the doped V_2O_5 and VOB phases are associated with electron hopping between V^{4+} and V^{5+} valence sites rather than Fe^{2+} and Fe^{3+} valence sites.

The existence of the V^{4+} ions in the VOB phase arises because of the dissociation of V_2O_5 just above the melting point of V_2O_5 according to the reaction

$V_2O_5 \rightarrow V_2O_{5-x} + x/2\, O_2$ where x increases with increasing temperature. [2]. This process results in the lowering of the oxidation state of the vanadium ion from V^{5+} to V^{4+} or even to V^{3+}. When the melt cools, the θ-VOB phase forms with V^{4+}, V^{5+} and Fe^{3+} ions occupying regular lattice sites in the monoclinic structure. This process can also be extended to the doped V_2O_5 phase where the Fe concentration is small. In this phase the Fe^{3+} ions substitute V^{5+} ions in the orthorhombic structure with additional Fe^{3+} ions located at interstitial sites in order to maintain charge neutrality. However, considering the dissociation of V_2O_5 above the melting point, it is possible that V^{4+} ions are also be present in the doped V_2O_5 phase. This will further have the implication that the ratio of Fe^{3+} ions at substitutional sites to those at interstitial sites will change. It is therefore possible that there will be V^{4+} and V^{5+} ions present in both phases and that the electrical conductivity occurs through electron hopping between these V^{4+} ions and V^{5+} ions. This conductivity would increase with temperature.

4. Conclusion

The semiconducting properties of the doped V_2O_5 and VOB phases are due to the hopping of electrons between the V^{5+} and V^{4+} ions and not to the Fe^{3+} and Fe^{2+} ions. Thus the reason for not observing any changes with temperature in the Mössbauer spectra is that the largest contribution to the hyperfine interaction arises from the immediate vicinity of the ^{57}Fe nucleus, which consists of the electrons of the Fe^{3+} ion and the nearest oxygen neighbours. The contribution of the V^{4+} and V^{5+} ions to this interaction are therefore not large when ^{57}Fe is used as the Mössbauer isotope.

5. References

[1] V.V.Naicker and K.Bharuth-Ram, to be published
[2] G.A.Khan and C.A.Hogarth, J.Mat.Sc., 25 (1990) 5014
[3] M.Pekala and A.Polaczek, Phys.Stat.Sol. (a), 58 (1980) 533
[4] K.Jansen and G.Sperlich, Phys.Stat.Sol. (b), 55 (1973) 495
[5] T.K.Bansal, et al., Hyp.Int., 35 (1987) 863
[6] F.J.Duncan and R.M.Golding, Quarterly Rev., 19 (1965) 36.
[7] Y.Niida, et al., Hyp.Int., 69 (1991) 631
[8] J.J.Bara, et al, J.Solid State Chem., 58 (1985) 143
[9] E.W.Muller, MOSFUN, (1980) Mössbauer Effect Data Center, Uni. of North Carolina, USA.

APPENDIX C

Program to determine lattice parameters for orthorhombic, tetragonal and monoclinic crystallographic systems.

```
$debug
      program main
      real x(100),a(3,4),xobs(300),yobs
      integer nobs, h(100),k(100),l(100)
      integer io(4),im(4),it(4)
      open(5,file='data.in1')
      do 10,i=1,3
      read(5,*) (a(i,j),j=1,4)
10    continue
      j = 0
      read(5,*) nobs
      do 20,i=1,nobs
      read(5,1080) xobs(i),yobs,dum,io(1),io(2),io(3),io(4),dum,
     & it(1),it(2),it(3),it(4),dum,im(1),im(2),im(3),im(4)
1080  format(f6.3,1x,f7.1,1x,3(f6.3,1x,4(i2),2x))
      if(io(4).eq.0) goto 15
          j = j + 1
          x(j) = xobs(i)
          h(j) = io(1)
          k(j) = io(2)
          l(j) = io(3)
15    continue
20    continue
      write(*,1000)
1000  format(' This is the othorhombic calculation')

1001  format(a6)
      call ort(j,a,x,h,k,l)
c     call tet(j,a,x,h,k,l)
c     call mon(j,a,x,h,k,l)
c use ort, tet or mon for orthorhombic, tetatragonal or monoclinic systems respectively
      close(5)
      call out(nobs,a)
      end

      subroutine out(nobs,const)
      real const(3,4),xobs,yobs,xcal(3)
      real lambda,pie,a(3),b(3),c(3)
      integer nobs,h,k,l,hkl(3,4)
      lambda = 1.7901970
      pie = 3.1415927

      do 5,i=1,3
          a(i) = const(i,1)
          b(i) = const(i,2)
          c(i) = const(i,3)
          gamma = const(3,4)
          g1 = cos(pie*gamma/180)
          g2 = sin(pie*gamma/180)**2
5     continue
      open(20,file='data.ot1')
```

```
      do 10,i=1,3
           write(20,1000) (const(i,j),j=1,4)
10    continue
1000  format(3(1x,f7.4),2x,f6.2)
      write(20,*) nobs
      open(5,file='data.in1')
      do 20,i=1,4
           read(5,*) dum1
20    continue
      do 30,i=1,nobs
c
           read(5,1080) xobs,yobs,xcal(1),
     &     hkl(1,1),hkl(1,2),hkl(1,3),hkl(1,4),xcal(2),hkl(2,1),
     &     hkl(2,2),hkl(2,3),hkl(2,4),xcal(3),
     &     hkl(3,1),hkl(3,2),hkl(3,3),hkl(3,4)
1080  format(f6.3,1x,f7.1,1x,3(f6.3,1x,4(i2),2x))

      do 65,j=1,3
           h = hkl(j,1)
           k = hkl(j,2)
           l = hkl(j,3)

           if((h.eq.0).and.(k.eq.0).and.(l.eq.0)) then
                xcal(j) = 0.0
           elseif((j.eq.1).or.(j.eq.2)) then
                d1 = h*h/(a(j)*a(j))
                d2 = k*k/(b(j)*b(j))
                d3 = l*l/(c(j)*c(j))
                d4 = 1./sqrt(d1+d2+d3)
                d5 = asin(lambda/(2*D4))
                xcal(j) = d5*2*180/pie
           else
                d1 = (h**2)/(a(j)**2) + (l**2)/(c(j)**2)
                d2 = 2*h*l*g1/(a(j)*c(j))
                d3 = (d1 - d2)/g2 + (k**2)/(b(j)**2)
                d4 = 1./sqrt(d3)
                d5 = asin(lambda/(2*D4))
                xcal(j) = d5*2*180/pie
           endif
65    continue
      write(20,1080) xobs,yobs,xcal(1),hkl(1,1),hkl(1,2),
     & hkl(1,3),hkl(1,4),xcal(2),hkl(2,1),hkl(2,2),hkl(2,3),
     & hkl(2,4),xcal(3),hkl(3,1),hkl(3,2),hkl(3,3),hkl(3,4)
30    continue
      close(5)
      close(20)

      return
      end

      subroutine ort(nlsq,a7,xlsq,h,k,l)
      real xlsq(100), a7(3,4)
      real x(100), y(100), z(100), the1(525),d(525)
      real lambda
      real pie,m11,m12,m21,m22
      integer h(100),k(100),l(100)
      integer nlsq
```

```
      lambda = 1.7901970
      pie = 3.1415927
      a = a7(1,1)
      b = a7(1,2)
      c = a7(1,3)
      do 10,i=1,nlsq
            the1(i) = xlsq(i)
            x(i) = h(i)*h(i)
            y(i) = k(i)*k(i)
            z(i) = l(i)*l(i)
            theta = the1(i)*pie/(180*2)
            dval = lambda/(2*sin(theta))
            d(i) = 1/(dval*dval)
10    continue
      do 20,i=1,nlsq
            t11 = t11 + x(i)*x(i)
            t12 = t12 + x(i)*y(i)
            t13 = t13 + x(i)*z(i)
            t22 = t22 + y(i)*y(i)
            t23 = t23 + y(i)*z(i)
            t33 = t33 + z(i)*z(i)
            e1 = e1 + d(i)*x(i)
            e2 = e2 + d(i)*y(i)
            e3 = e3 + d(i)*z(i)
20    continue
      m11 = t11/t13 - t12/t23
      m12 = t12/t13 - t22/t23
      m21 = t11/t13 - t13/t33
      m22 = t12/t13 - t23/t33
      f1 = e1/t13 - e2/t23
      f2 = e1/t13 - e3/t33
      a2 = (f1/m12 - f2/m22)/(m11/m12 - m21/m22)
      b2 = (f1 - m11*a2)/m12
      c2 = (e1 - t11*a2 - t12*b2)/t13
      a = 1/sqrt(a2)
      c = 1/sqrt(c2)
      b = 1/sqrt(b2)
      a7(1,1) = a
      a7(1,2) = b
      a7(1,3) = c
      write(*,*) a,b,c
      return
      end

      subroutine tet(nlsq,a7,xlsq,h,k,l)
      real xlsq(100), a7(3,4),a,b,c
      real x(100), y(500), z(525), the1(525),d(525)
      real lambda
      real pie,m11,m12,m22
      integer h(100),k(100),l(100)
      integer nlsq,nlsq
      lambda = 1.7901970
      pie = 3.1415927
      a = a7(2,1)
      b = a7(2,2)
      c = a7(2,3)
      do 10,i=1,nlsq
```

```
        the1(i) = xlsq(i)
        x(i) = h(i)*h(i)
        y(i) = k(i)*k(i)
        z(i) = l(i)*l(i)
        theta = the1(i)*pie/(180*2)
        dval = lambda/(2*sin(theta))
        d(i) = 1/(dval*dval)
10    continue
      do 20,i=1,nlsq
        m11 = (x(i) + y(i))*(x(i) + y(i)) + m11
        m12 = (x(i) + y(i))*z(i) + m12
        m22 = z(i)*z(i) + m22
        e1 = d(i) * (x(i)+y(i)) + e1
        e2 = d(i) * z(i) + e2
20    continue
      a2 = (e1/m12 - e2/m22)/(m11/m12 - m12/m22)
      c2 = (e2 - a2*m12)/m22
      a = 1/sqrt(a2)
      c = 1/sqrt(c2)
      b = a
      a7(2,1) = a
      a7(2,2) = b
      a7(2,3) = c
      write(*,*) a,b,c
      return

      end

      subroutine mon(nlsq,a7,xlsq,h,k,l)
      real xlsq(100), a7(3,4),a,b,c
      real x(100), y(500), z(525), the1(525),d(525)
      real lambda
      real a4,a5,b4,b5,c4,c5,d10
      real pie,gamma,fa1,fb1,fc1,fd1,rr1,fa,fb,fc,fd,rr
      real a0,b0,c0,d0,aold,bold,cold,dold,gamma0,gammao
      real m11,m12,m13,m14,m15,m21,m22,m23,m24,m25
      real m31,m32,m33,m34,m35,m41,m42,m43,m44,m45,ae,be,ce,de,ge
      real t11,t12,t13,t14,t21,t22,t23,t24,t31,t32,t33,t34
      real s11,s12,s13,s21,s22,s23,r11,r21
      integer nlsq,h(100),k(100),l(100)
      integer nlsq,ref(525),itype(525)
      integer nhkl

      lambda = 1.7901970
      pie = 3.1415927
      a = a7(3,1)
      b = a7(3,2)
      c = a7(3,3)
      gamma = a7(3,4)

      gamma0 = gamma
      a0 = a
      b0 = b
      c0 = c

      do 10,i=1,nlsq
        the1(i) = xlsq(i)
```

```
      x(i) = h(i)
      y(i) = k(i)
      z(i) = l(i)
      theta = the1(i)*pie/(180*2)
      dval = lambda/(2*sin(theta))
      d(i) = 1/(dval*dval)
10    continue

      do 107,k7 = 1,1000
      aold = a
      bold = b
      cold = c
      gammao = gamma

      gamma = gammao*pie/180
      a = 1/aold
      b = 1/bold
      c = 1/cold
      do 20,i=1,nlsq
      fa1 = fa(x(i),y(i),z(i),a,b,c,gamma)
      fb1 = fb(x(i),y(i),z(i),a,b,c,gamma)
      fc1 = fc(x(i),y(i),z(i),a,b,c,gamma)
      fd1 = fd(x(i),y(i),z(i),a,b,c,gamma)
      rr1 = rr(x(i),y(i),z(i),a,b,c,gamma,d(i))

      m11 = m11 + fa1 * fa1
      m12 = m12 + fa1 * fb1
      m13 = m13 + fa1 * fc1
      m14 = m14 + fa1 * fd1
      m15 = m15 + fa1 * rr1

      m21 = m12
      m22 = m22 + fb1 * fb1
      m23 = m23 + fb1 * fc1
      m24 = m24 + fb1 * fd1
      m25 = m25 + fb1 * rr1

      m31 = m13
      m32 = m23
      m33 = m33 + fc1 * fc1
      m34 = m34 + fc1 * fd1
      m35 = m35 + fc1 * rr1

      m41 = m14
      m42 = m24
      m43 = m34
      m44 = m44 + fd1 * fd1
      m45 = m45 + fd1 * rr1
20    continue

      t11 = m11/m14 - m41/m44
      t12 = m12/m14 - m42/m44
      t13 = m13/m14 - m43/m44
      t14 = m15/m14 - m45/m44

      t21 = m11/m14 - m31/m34
      t22 = m12/m14 - m32/m34
```

```
            t23 = m13/m14 - m33/m34
            t24 = m15/m14 - m35/m34

            t31 = m11/m14 - m21/m24
            t32 = m12/m14 - m22/m24
            t33 = m13/m14 - m23/m24
            t34 = m15/m14 - m25/m24

            s11 = t11/t13 - t21/t23
            s12 = t12/t13 - t22/t23
            s13 = t14/t13 - t24/t23

            s21 = t11/t13 - t31/t33
            s22 = t12/t13 - t32/t33
            s23 = t14/t13 - t34/t33

            r11 = s11/s12 - s21/s22
            r21 = s13/s12 - s23/s22

            ae = r21/r11
            be = (s23 - ae*s21)/s22
            ce = (t34 - ae*t31 - be*t32)/t33
            ge = (m45 - ae*m41 - be*m42 - ce*m43)/m44

            gamma = gamma + ge
            a = a + ae
            b = b + be
            c = c + ce

            a = 1/a
            b = 1/b
            c = 1/c
            gamma = gamma * 180/pie

            write(*,1005) a,b,c,gamma
1005        format(4(2x,f7.3))
1006        format(3(2x,f7.3))
107     continue
        a7(3,1) = a
        a7(3,2) = b
        a7(3,3) = c
        a7(3,4) = gamma
        return
        end

        real function fa(x,y,z,a,b,c,gamma)
        real x,y,z,a,b,c,gamma
        fa = 2*(a*x*x - c*x*z*cos(gamma))/(sin(gamma)*sin(gamma))
        return
        end

        real function fb(x,y,z,a,b,c,gamma)
        real x,y,z,a,b,c,gamma
        fb = 2*b*y*y
        return
        end
```

```
real function fc(x,y,z,a,b,c,gamma)
real x,y,z,a,b,c,gamma
fc = 2*(c*z*z - a*x*z*cos(gamma))/(sin(gamma)*sin(gamma))
return
end

real function fd(x,y,z,a,b,c,gamma)
real x,y,z,a,b,c,gamma,t1,t2,t3,t4
t1 = 2*a*c*x*z/sin(gamma)
t2 = 1 + 2/(tan(gamma)*tan(gamma))
t3 = 2*(a*a*x*x + c*c*z*z)*cos(gamma)
t4 = sin(gamma)*sin(gamma)*sin(gamma)
fd = t1*t2 - t3/t4
return
end

real function rr(x,y,z,a,b,c,gamma,d)
real x,y,z,a,b,c,d,gamma,t1,t2,t3
t1 = a*a*x*x + c*c*z*z - 2*a*c*x*z*cos(gamma)
t2 = sin(gamma)*sin(gamma)
t3 = y*y*b*b
rr = d - t1/t2 - t3
return
end
```